OFFICE OF NAVAL RESEARCH
DEPARTMENT OF THE NAVY
CONTRACT N00014-67-A-00094-0003

FINAL REPORT

EXPERIMENTAL INVESTIGATION OF NON-STEADY FORCES ON HYDROFOILS OSCILLATING IN HEAVE

BY
R. K. DeLONG and A. J. ACOSTA

DIVISION OF ENGINEERING AND APPLIED SCIENCE
CALIFORNIA INSTITUTE OF TECHNOLOGY
PASADENA, CALIFORNIA

MARCH 1969

EXPERIMENTAL INVESTIGATION OF NON-STEADY FORCES ON HYDROFOILS OSCILLATING IN HEAVE

This research was carried out under Naval Ships Command, General Hydromechanics Research Program, Subproject SR 009 01 01, administered by the Naval Ship Research and Development Center

Contract No. N00014-67-A-0094-0003

FINAL REPORT

by

R. K. DeLong and A. J. Acosta

Division of Engineering and Applied Science
California Institute of Technology
Pasadena, California

March 1969

TABLE OF CONTENTS

Abstract.

Measurements of the unsteady forces on heaving delta wing hydrofoils having apex angles of 15° and 30° were carried out in fully wetted flow, planing at a free surface, and with forced ventilation. The fully wetted dynamic measurements were in good agreement with the results of lifting surface theory at small angles of attack. A slender body theory of planing due originally to Tulin is extended to account for non-steady motions. This theory generally underestimates the in-phase lift force; the quadrature unsteady lift is well predicted by the theory. Additional measurements of steady planing delta wings were carried out; for small apex angles and small angles of attack the theory is found to be adequate though it does appear to underestimate the lift somewhat. Some additional experiments on non-steady forces on two-dimensional fully wetted and fully cavitating hydrofoils were also carried out.

I. Introduction.

The present report is concerned with the fluctuating forces that act on hydrofoils in non-steady motions. There are many practical reasons for interest in this subject; most of these stem from the problems of developing high speed surface ship components. A recent monograph (Ref. 1) summarizes much of the work in non-steady hydrodynamics; it includes a survey of current theoretical efforts in hydroelasticity, non-steady lifting surface theory and some supporting experimental work. The latter, though, like its aerodynamic counterpart is rather sparse. The present work is intended mainly to supplement this experimental work for configurations not previously investigated to any great degree, in order to provide this information for its own sake and to call attention to situations where presently available theoretical models are not adequate or have not been applied. In this respect, it is a continuation of the work in Refs. 2 and 3 wherein unsteady hydrodynamic data were obtained for two-dimensional and finite aspect ratio hydrofoils in heaving motion in fully wetted flow and forced-ventilation flow. Similar studies are reported herein on delta wings in fully wetted flow, in a planing configuration and also in forced-ventilation flows; in addition some work on fully wetted and naturally cavitating two-dimensional hydrofoils in heaving motion is presented and compared with existing calculations; it will be seen that at present, at least for the configurations studied, these theories do not entirely account for the observations.

In the following text some of the background work in delta wings is touched upon and more details of the experimental program are

outlined. These experimental results, together with descriptions of the test apparatus and experimental procedures are then described. The appendix contains a quasi-steady theory of non-steady planing of delta wings that was devised in an attempt to explain the observations.

Previous Investigations.

The interest in triangular lifting surfaces hardly needs justification. They are common in aeronautics. For background we will now review from the work of persons whose primary interest was motivated by aeronautical considerations some of these prior "fully wetted" flow studies. First, as was mentioned by Smith (4), the effect of Reynolds number on the general features of the flow about sharp edged delta wings is small, and for this reason we are not primarily concerned with viscous effects here provided the Reynolds number is moderately high. The salient feature of a slender delta wing is that the Kutta condition is satisfied along the lateral edges of the wing. The shed vorticity then gives rise to a longitudinal vortex springing from the apex of the wing and passing downstream near the leading edge. The flow at the leading edge itself streams smoothly off the surface and becomes entrained into the vortex. In a sense, the leading edge may be said to be separated. Prior to the interest in flows about delta wings with leading edge separation R. T. Jones (5) presented a method for calculating the force on such slender bodies at a small angle of attack. Jones' contribution was to show that for slender bodies the analysis could be carried out in a plane perpendicular to the main flow and thus to solve a two-dimensional problem. The cross-flow plane solution used by him

was that of a flat lamina moving normally to itself in potential flow. The infinite velocities at the lateral edges in this model clearly do not exist in the actual case. Jones' analysis is, however, satisfactory for slender delta wings at small angles of attack and his result is often called the linear contribution since it predicts the force to be linear with angle of attack.

Subsequent experimental investigations, particularly by Roy (6), caused interest in finding a model which represented the observed flow especially the smooth outflow condition at the leading edges. Legendre (7) proposed the addition of two vortices above and inboard of the two leading edges. The strength and position of the vortices would be determined by the smooth outflow condition at the leading edges with the condition that the vortices have no net force on them. The two vortices were implicitly assumed to be joined by a cut so that the lift on the foil or foil-vortex system would be uniquely determined.

Following a suggestion by Adams (8), Legendre modified the model with the vortices being joined to their respective leading edges by cuts rather than to each other. This had the advantage that the cut could be interpreted physically as a vortex sheet feeding the primary vortex. His force condition was still on the vortex which meant that the lift on the foil depended on whether the forces or the cuts were included or not. Brown and Michael (9) proposed a model, anticipated by Edwards (10), which placed the zero force condition at each vortex on the cut as well. That is, the net force on the vortex and cut taken together should be zero. The ambiguity in the lift calculation was then removed. The Brown and Michael model has served as a basis for a number of other investigations.

It has the advantage of basic simplicity and it reasonably represents the flow picture. It does not, however, predict the forces very well, being somewhat too high. The stability derivatives are likewise poorly predicted.

Trying to develop a model which was even closer to the physical flow and one which would better predict the forces, Mangler and Smith (11) proposed a model with the flow separated from the leading edge in the form of a spiral vortex sheet. Somewhat better agreement with experimental data was obtained than with the Brown and Michael model. It has the disadvantage that the added complexity requires that the problem be solved on a digital computer. Smith (4) has recently published some further calculations using this model. These are used in the discussion of the experimental results to follow.

Apart from the foregoing studies, Gersten (12) presented a method of calculating the stability derivatives for triangular wings. Gersten's method is basically one of lifting surface theory. It has the advantage that it predicts the forces fairly well but the trailing vortex field of his lifting surface theory does not physically resemble the actual flow.

These are the major efforts to predict the steady forces on fully wetted delta wings. There have been other studies of the vortex structure and some flow visualization studies, particularly Marsden, et al. (13), but these are the models from which most current work extends. The studies in this area are currently active as will be noted by Küchemann's (14) report on the 1964 I. U. T. A. M. symposium held at Ann Arbor, Michigan. Several of the papers, notably (15), (16) and

(17), presented at this symposium have since been published in volume seven of Progress in Aeronautical Science. Also the work of Garner and Lehrian (18) is notable but is really derived from Gersten's.

In the area of unsteady loads on non-stationary delta wings Jones' idea was discussed by Miles (19) and Garrick (20) for the linear problem. The unsteady problem with leading edge separation has been treated by Randall (21) who used the Brown and Michael model to calculate the force on a slender delta wing performing infinitesimal heaving oscillations. Lowson (22) and later Maltby (23) used the same model for a slender delta wing performing finite heaving oscillations. The advisability of using this model for unsteady forces seems questionable in view of the not too good agreement with steady experiments, but their interest in this problem seemed to be primarily in the vortex position rather than forces. Due to the computational difficulties no extension of the more realistic Mangler-Smith model has been made to unsteady flows but it would undoubtedly give superior force predictions.

Finally we mention the investigations of the forces on delta wings oscillating in heave by Lawrence and Gerber (24). They used lifting surface theory to calculate the effect of reduced frequency on the unsteady forces on some rectangular and delta wings. The theory is limited to vanishingly small angles of attack, not a very practical case, but gives surprisingly good correlation within the bounds of the theory.

The other two types of flow investigated herein are unique to hydrodynamics, therefore no aeronautically inspired results will be available. The second flow type (i. e., ventilated or cavitating) has received but slight treatment for delta wings. We know only of the

theoretical work of Tulin (25) and later Kaplan (26) who used a combination of slender body and linearized free streamline theory to treat the case of partial cavities on delta wings. Later, Cumberbatch and Wu (27) undertook a non-linear analysis of a fully cavitating delta wing – again, however, using a slender body approach. Supporting experimental work is very limited and for the cavitating case only Reichardt and Sattler's work (28) is known while Kiceniuk (29) undertook measurements of the fully ventilating (or cavitating) case. We are unaware of any theoretical or experimental work on non-steady cavity flows for these configurations.

The situation for planing flows is somewhat different. There exists a considerable literature for steady planing of prismatic hulls in steady flows and there is some work on the water impact problem of hydro-skis and the like. Most of the low aspect ratio planing surface theory is, however, semi-empirical. The one notable exception which deals with steady planing delta wings is a theory presented by Tulin (30) on the planing of slender bodies at small angles of attack. This theory is reconsidered in Appendix II and is extended to include quasi-steady heaving motions of the hydrofoil. As a general remark the problem of unsteady planing has received very little attention; the major effort in the past has gone toward predicting impact loads on hydro-skis attached to aircraft. The whole subject appears to need extensive study.

Present Investigations.

As indicated above the emphasis of the present report is on the forces experienced by delta wing hydrofoils oscillating in a heaving

motion; no investigations into the motions of the separated leading edge vortex core were undertaken. Though most of the present experimental work was carried out with this type of foil, additional work on two-dimensional foils was carried out but discussion of these tests will be deferred for the moment.

To investigate the dynamic properties of heaving delta wings, two apex angles, 15° and 30°, were chosen. It was also decided to carry out additional steady measurements and for this purpose an additional set of model wings having apex angles of 10°, 15°, 30°, 45° and 60° and a different chord length than the dynamic models was obtained. (The different chord length made it possible to check independently the effect of Froude number.) In the dynamic tests, the models were oscillated in heave at different angles of attack, free stream velocity, oscillation frequency, and oscillation amplitude. The depth of submergence was also varied for the fully wetted tests. Measurements were made of the unsteady lift and drag forces and pitching moment. With this many parameters to consider, the data gathering and processing was quite time-consuming, but the lack of availability of data on these effects made the work seem that much more worthwhile.

The data gathered for the ventilated delta wings were limited because of the additional parameter to be varied, cavity length, and because during the course of the experiments it was learned that the 15° delta wing would not ventilate properly. It was felt that the influence of the ventilation strut on the flow field over the 15° model was the cause of the problem. It was decided therefore that data would be taken only for the 30° model, and for economy only one angle of attack ($\alpha = 20^{\circ}$), one submergence depth ($D = 0.83$ chords) and one oscillation amplitude.

The added parameter of cavity length and the associated parameters of air supply rate and ventilation number cause the data gathering to still be a fairly large task especially since in all the investigations reported herein the experiment essentially had to be run twice, once with the lift and pitching moment balance and once with the drag balance. Pitching moment data are not reported for the ventilation tests because the data from both balances are required to calculate the pitching moment about a point on the model and the data were found to be so sensitive to cavity length that data at the exact conditions of the "lift" runs were not gathered for drag. Instead the drag data are for slightly different conditions.

Both the 15° and 30° models were used in the dynamic planing experiments. They were run at mean angles of attack of 6° and 12°. Since the forces are smaller for a planing body than for a fully wetted one the tunnel velocity was run as high as practical (i. e., $U = 22$ ft/sec) to provide larger signals. The desire to provide large force signals for measurement was thwarted somewhat because if the model was allowed to perform large displacements during an oscillation cycle it would be subject to a large wetted area change or it might become submerged during part of the cycle. This second effect, referred to here as part-cycle-planing, can cause as will be seen drastic changes in the unsteady forces. For these reasons, the oscillation displacement was usually kept as low as practical during the dynamic planing tests, although this does mitigate against accuracy.

In the following sections, the experimental apparatus and test procedure is covered at some length. Then follows a rather extensive

presentation of the results of the delta wing investigations in the various types of flow studied. We then give a brief report on the two-dimensional fully wetted and cavitating tests.

II. Experimental Apparatus.

Free Surface Water Tunnel.

The experimental work on the delta wings oscillating in heave was conducted in the Free Surface Water Tunnel at the California Institute of Technology. Reference (31) describes the tunnel in considerable detail so only its major features will be discussed here. It is a closed loop, recirculating tunnel with a useable working section approximately 20 inches by 20 inches in cross section and about eight feet long. The distinguishing feature of the working section is that the upper surface is open to the atmosphere which enables the tunnel to be used for planing and near-surface tests.

The maximum velocity attainable in the working section is about 25 feet per second. This velocity is indicated on a water manometer which gives the difference between the total head upstream from the nozzle and the static head in the static head in the working section. A feature of the tunnel which was added after it was built and consequently is not discussed in Ref. (31) is the skimmer. Its function is to remove the fluid decelerated in the boundary layer on the upper surface on the nozzle. This fluid is added back into the circuit downstream of the working section. The result is that the velocity profile of the flow in the working section is constant near the free surface, allowing meaningful planing tests to be performed. There are of course boundary layers

on the bottom and side walls of the working section but these do not ordinarily interfere with the experiment. Figure 1 presents an overall view of the working section and test equipment.

Hydraulic Pump and Oscillator.

The dynamic models were made to oscillate hydraulically. A Dennison variable displacement pump supplied oil at 1250 psi to a servo-controlled double-acting piston which in turn caused the excitation of the foil. These details are shown schematically in Fig. 2. The servo valve and piston were designed and built by Team Corporation of El Monte, California. Not pointed out in the figures are the position and velocity transducers which sense the motion of the piston and provide feedback information to the servo controller. The position transducer is a linear variable differential transformer (LVDT) and the velocity transducer is a conventional type linear voltage generator.

Servo Controller.

The motion of the piston is controlled by a servo-amplifier which minimizes the velocity error of the piston through conventional feedback principles. It was designed and built by the McFadden Electronics Company of South Gate, California, and is Model 150A.

Models and Attachment Fixtures.

The dynamic models, shown in Fig. 3, are two sharp-edged delta wings with apex angles of 15° and 30°. They were fabricated from one-quarter inch aluminum plate and are both approximately one foot in length. Their bottom sides are both flat and a two-stage bevel, rounded by hand,

was used on the top. This produced quite sharp edges. The effect of camber is negligible particularly in light of the leading edge separation which occurs in all three types of flow (i. e., planing, fully wetted and ventilated). Provision for running different angles of attack was accomplished through spacers placed between the model and the force balance. This assures a simple rigid system in which the angle can be reset at sill. It does not have the flexibility of a continuously variable device, but has proved very workable here.

Instrumentation.

1. Lift and Pitching Moment Balance.

The measurement of the unsteady lift and pitching moment forces was accomplished by a strain gage strut balance. That is, the balance is an extension of the support strut. The placement of the balance is shown in Fig. 2. The balance was constructed so that the lift and pitching moment force would be taken out through two longitudinally spaced vertical links. The drag force was taken out by one horizontal link. On each of these primary load-carrying links was attached a conventional wire strain gage bridge. By summing the forces in the two vertical links the lift is obtained; by differencing them the pitching moment is obtained. It was found in static tests after the balance was constructed that the drag element had an unacceptable amount of roll moment interaction and consequently this balance was not used for drag measurements but rather a new one was designed. It is described in some detail in the next section.

The lift and pitching moment balance is shown in Fig. 4 before the installation of the strain gages. The wires for the bridges pass through

a hole in the top of the balance, up through the center of the support strut and piston to a connector at the top of the oscillator. After the installation of the strain gages metal plates were soldered to the sides of the balance for mechanical protection and to provide support for the waterproofing which consisted of thin sheets of latex cemented around the outside of the balance. The balance was slightly pressurized via the hole carrying the wires to prevent water from entering the balance in the event of a leak.

The balance is fairly rigid having no natural frequencies below 200 cps, but a dynamic calibration of both lift and pitching moment was provided at each of the operating frequencies to obviate the effect of a dynamic magnification factor. The calibration is discussed in more detail later.

2. Drag Balance.

As was mentioned the existing balance was found to be unacceptable for drag measurements due to interactions. As dynamic drag measurements are quite scarce a new balance was designed to measure drag only with the hope of isolating all other forces and moments and eliminating all interactions. The final balance showed in extensive static tests that it did just that to the least count of our equipment.

The balance is shown in Fig. 5. It consists of two overlapping side plates which are about 0.2 inch thick and very rigid, one of which is attached to the support strut and the other to the model. The side plates are connected to each other in turn by a system of flexures and an instrumented link to measure the drag force. (This drag link is not visible in Fig. 5.)

The flexure system consists of four thin metal sheets lying in two vertical transverse planes. Each flexure is 0.8 inch high, 0.005 inch thick and 0.2 inch in the lateral direction. They were cut from sheet stock and furnace brazed in position. They carry all loads except drag for which they are comparatively flexible. The instrumented link carries most of the drag force; it is a flat bar approximately 0.3 inch high, 3 inches overall length and 0.050 inch thick except in the central instrumented portion where it is 0.030 inch thick. It is attached at the front to the grounded side and at the back to the model side. Thus, a drag force puts the link in tension. Small "cut-outs" in two perpendicular planes were machined into the link at each end just inboard of the attachment position to prevent any displacements due to lift force, pitching or rolling moments from causing any unwanted interaction.

The strain gages are of the solid state type; two are the P type and two the N type, which not only give high gage factors but also four active gages in a pure tension or compression member. Their placement on the gaged section was further planned to cancel any moments which might creep in. Temperature compensation is also provided by gage matching but that is of little importance in this application.

Because the gages could not be in place during the brazing operation the balance was designed so that the drag link could be inserted through an opening in the trailing edge after brazing and fastened in place by dowel pins and cap screws through access holes in the side pieces. The opening in the trailing edge was filled with a brass plug to provide support for the waterproofing. This has the added advantage of easing maintenance should the gage fail. Waterproofing is provided as on the lift balance by thin latex sheets cemented to the outside of the balance.

The balance was designed so that it is very rigid in all directions; in the drag direction its natural frequency is above 600 cps with a model attached. The balance therefore could be calibrated statically and the same factor used at all frequencies.

3. Voltage Supplies and Amplifiers.

Figure 6 will be helpful in showing how the electronic equipment is patched together. The excitation voltages for the strain gage bridges were provided by a Microdot Power and Balance Unit PB-200A for each. They have provision for patching resistors on a conditioning board to approximately balance the bridge. A potentiometer was also provided for balance which was useful for nulling the steady load. Each unit contained a potentiometer for setting the excitation voltage. A Microdot Voltage and Balance Monitor VB-300 was used to monitor the excitation voltages and to null the bridge output during steady operation.

The output of the strain gage bridges was fed through a series of Burr-Brown Model 1685 amplifiers. In the lift-pitching moment balance the outputs were summed and differenced in the first two amplifiers to produce lift and pitching moment. These outputs went to a selector switch so that only the signal being analyzed would be fed to two other amplifiers connected in series. The total gain was then 1000.

4. Return Signal Analyzer.

The force signals and heaving velocity signals were analyzed in Boonshaft and Fuchs Model 711A Return Signal Analyzer (RSA). The signal being analyzed is compared internally to a signal of the same frequency as the command signal. A Fourier analysis is performed

electronically and the components having the same frequency as the exciting frequency can be read out on panel meters or on an auxiliary voltmeter.

5. Variable Phase Low Frequency Oscillator.

The command signal which was fed to the servo controller was generated by a Boonshaft and Fuchs Model 711AP Variable Phase Low Frequency Oscillator (VPLFO). This has two outputs; one was fed into the servo controller, the other is also tied internally to the RSA. By varying the phase of the command signal while analyzing the output of the velocity transducer a velocity reference for the force signals can be obtained.

6. Digital Voltmeter.

The output of the RSA was connected to a Non-Linear Systems Series 2900 Digital Voltmeter. This is an integrating meter and the integrating times most frequently used were one and ten seconds, the latter used if the data were unsteady.

7. Position and Velocity Transducers.

The position and velocity transducers were mentioned earlier. The primary functions of the position transducer were to aid in the calibration of the velocity transducer and to provide static height stability in the servo controller. The velocity transducer provided the phase reference for the force data and was also used in the normalization of the forces.

Support and Ventilation Struts.

The support strut tying the model and force balance to the piston of the oscillator is a NACA 0010 section of 10 percent thickness and

4 inch chord. It was designed to minimize ventilation from the free surface. The force balances had similar contours to continue the strut profile to the model. The angle changing spacers were also contoured similarly.

For the ventilation tests a means was needed to provide a known quantity of air at the suction side of the foil without otherwise interfering with the flow. The method finally chosen was a hollow bi-convex strut fabricated from two sheets of aluminum 0.040 inch thick rolled into cylindrical sections which were subsequently heli-arc welded at the leading and trailing edges. This was slipped over the support strut and attached to it above the balance. A means was provided to seal the upper end and air supply and pressure fittings were provided.

Ventilation Measuring Apparatus.

1. Air Supply Measurement.

The air supplied to the cavity during the ventilating runs was measured by a Fischer-Porter Flowmeter and the supply pressure was measured on a Heise Bordon tube pressure gage. The reduction of the data is discussed later.

2. Cavity Length Measurement.

The cavity length was measured with a tape rule held against the working section side. This method probably is not accurate to less than an inch but considering the difficulty in defining the termination point for the cavity this accuracy was quite acceptable.

3. Cavity Pressure Measurement.

The cavity pressure was measured by a water-filled U-tube manometer open to the atmosphere on one end and connected to the top

of the ventilation strut on the other. There was a pressure drop from the point of measurement to the cavity which was accounted for by running tests with the tunnel dry. This allowed the pressure drop which is a function of the air supply rate to be subtracted out.

III. Experimental Procedure.

Calibrations.

1. Position Transducer.

The position transducer was calibrated using a microscope attached to a lead screw and counter. The lead screw and counter were geared together so that the counter read directly in thousandths of an inch. The microscope could be set with the cross hairs aligned to a mark on the oscillator shaft; a number of position and voltage readings would then be made and the data least squares fit with a cubic polynomial. The linear term is the only one which is used since over the range covered in the velocity transducer calibration only the linear term is important.

2. Velocity Transducer.

The velocity transducer was calibrated using the position transducer since the motion was simple harmonic. At each of the frequencies used in the experiment the velocity and position signals were analyzed using the Return Signal Analyzer. Since for simple harmonic motion the velocity amplitude is just the angular frequency times the position amplitude, and since we know the position calibration factor, we can then infer the velocity calibration factor.

3. Lift and Pitching Moment Balance.

The lift and pitching moment balance was calibrated both statically and dynamically. Static tests were run to determine the electrical position of each of the force links and the excitation voltages were chosen so that both of the lift gages (N_1 and N_2) had the same output/unit force. This must be done, otherwise the balance will have a lift-pitching moment interaction.

The dynamic calibrations were done at each frequency because even though the balance's natural frequency was well above those used in the experiment this afforded an easy way to obviate errors due to dynamic response. A two piece calibration mass was fabricated specifically for this task. The upper part, made of aluminum, was bolted to the strut at the model attachment holes. The bottom part, much heavier and fabricated of brass, was made so that it could be attached to the aluminum bar at any of six different positions to vary the longitudinal center of gravity of the total live mass. Using Newton's second law and the characteristics of simple harmonic motion the forces were inferred from knowing the mass and the velocity transducer output. By oscillating the mass at two different longitudinal positions (generally the end ones) the pitching moment calibration coefficients and the longitudinal electrical center were determined. This also allowed a check on the sensitivity of lift to pitching moment changes.

4. Drag Balance.

The drag balance presented a much easier calibration problem. Because of its designed-in constant response over the test frequency range the calibration could be and was done statically. This consisted

of bolting a fixture to the bottom of the balance and running a line from this fixture over a pulley to a hook on which shot-bags could be hung. The problem of assuring that the line was pulling in the drag direction was handled by levels on both the fixture and the line. Having only one load-carrying element in the drag direction no matching of outputs was required as in the "lift" balance, therefore the excitation voltage was changed to maintain a fixed calibration coefficient over the period of drag testing.

As a check for whipping of the strut the balance was oscillated with the tunnel dry and no sensible drag output was noted.

5. Return Signal Analyzer.

The manner in which the force coefficients were normalized meant that the Return Signal Analyzer processed a signal in the denominator as well as the numerator. This means that an absolute calibration was not required (in fact, it was checked against an rms voltmeter and appeared to be within two percent of scale) but only variations from scale to scale. These relative coefficients were obtained using a signal from the Velocity Phase Low Frequency Oscillator and leap-frogging from scale to scale. Except for the two lowest scales they were within one percent of the ratio of scales so even that had they not been accounted for, and they were, the effect would hardly have been noticed.

6. Air Supply Apparatus.

The ventilation tests required that three additional pieces of apparatus be calibrated. They are a flow meter, a supply pressure gage and in this case we also had to account for the pressure drop in the ventilation strut.

The flow meter was a Fischer-Porter product with tube No. FP-3/4-27-G-10/80 for which a calibration curve was provided by the manufacturer. It was double-checked against another flow meter which had been previously calibrated and was within the five percent tolerance, over the working range, that these instruments are good for.

The supply pressure, which exceeded 70 psi at the flow meter, was measured by a Heise gage No. H1665. This gage was checked with a dead weight tester and found to be within 0.1 psi from zero to ninety-five psi. This was the accuracy to which the gage could be read.

The cavity pressure was given by a water manometer less the pressure drop in the ventilation strut. This pressure drop was accounted for by running various air supply rates through the strut with the tunnel dry and calculating the relationship between pressure drop and mass flow rate. This drop was then subtracted from the apparent cavity pressure in the final data reduction.

Parameters Investigated.

There are basically six parameters whose influence on the force coefficients was investigated. They are angle of attack, aspect ratio, reduced frequency, submergence, oscillation amplitude and air supply rate. Not all combinations of the parameters were run due to the time involved, however representative checks were made where it was felt appropriate.

The basic angles of attack which were investigated varied depending on the type of flow. For instance, in the fully wetted runs angles of zero, six and twelve degrees were run for each of the submergences. The planing runs, however, were done only at six and

twelve degrees since proper planing cannot be established at zero degrees. The ventilated runs were performed at twenty degrees angle of attack because this is near the lowest angle that the model could be fully ventilated under the test conditions.

In addition to the basic data runs, tests were done at minus six and minus twelve degrees with the model fully wetted and at the deepest submergence. This was done to give some justification to the assumptions that the camber and strut effects were small.

Two different models were used. They were both fabricated from 0.250 inch aluminum plate and have sharp edges all around to insure flow separation. Both models were approximately one foot in length and had apex angles of 15 and 30 degrees. The aspect ratio of these two models is 0.526 and 1.071 respectively.

One of the most varied parameters in the tests was the reduced frequency. In all of the runs except the ventilation tests the reduced frequency was the one varied, by means of the frequency, having fixed the other variables. In addition to the fundamental influence of the reduced frequency on the force coefficients, various tunnel velocities were run to determine the effect of obtaining the reduced frequency by different frequency-velocity combinations. This was done only at an angle of attack of twelve degrees, 30^{o} model and at maximum submergence since this was thought to provide the severest test.

The effect of the free surface was investigated in the fully wetted tests by running the models at approximately two, six and ten inches submergence. These large submergence changes were accomplished by inserting spacers between the box holding the hydraulic oscillator and the tunnel.

For the data reduction it was desirable to normalize the force coefficients with the heaving velocity but to do this it was necessary to establish that the effect on these coefficients of changing the amplitude was negligible. Since it was impractical to do this at every combination of parameters the case of the 30^{o} delta wing, 12^{o} angle of attack, 0.83 chord submergence and 16.5 ft/sec tunnel velocity was chosen as at least representative if not a worst case. In the planing runs the oscillation amplitude was more constrained by other things to small values, consequently the effect was that it was not practical to measure but was thought to be very slight.

In the ventilation runs a whole new group of parameters was introduced. They are the air supply rate, the cavity length and the cavity pressure. These parameters are all directly related to each other so the situation is not quite as complicated as it sounds. The basic variable chosen was the air supply rate but the other data were also computed.

Data Runs.

In this section we will be concerned with the actual steps of data gathering. For the most part the steps are the same for both fully wetted and planing tests. The basic parameter varied for these two in any particular run was the frequency whereas in the ventilation runs the air supply rate was varied.

Before the start of a run we must select and fix the following "variables":

1. Model
2. Angle of attack

3. Submergence
4. Oscillation amplitude (fully wetted)
5. Tunnel velocity

At some time during the testing each combination of model and attachment fixtures must have its mass determined because the force due to the "live" mass and the acceleration must be accounted for to determine the fluid mechanical forces. This was accomplished by assembling the model and fixtures as for a test and then with the tunnel dry the model would be oscillated and the live mass tare determined.

Having fixed the above parameters and with the tunnel full and operating at the chosen velocity but with the model stationary, the bridge excitation voltages are checked and the bridges balanced to limit the DC input to the RSA. With the static bridge outputs zeroed the amplifiers are balanced. Now the model can be oscillated.

The frequency is chosen on the VPLFO and the voltage for the desired oscillation amplitude is dialed in. With the input shorted each output channel of the RSA is zeroed to limit the tare. Now the signal from the velocity transducer on the oscillator is applied at the input of the RSA and the phase of the command signal varied so that the RSA output appears only on one channel. By varying the phase in this way a velocity reference is obtained. The force is applied to the RSA. That part of the force signal observed on the channel previously containing the velocity has the same phase as the velocity. The second output channel gives the quadrature component of force.

In a typical data block zeros are taken for each channel with the input shorted. The heaving velocity is applied to the RSA and read. The

force signal is applied and each channel read. The input is again shorted and zeros again taken. When using the "lift" balance, the first force taken is the lift. After the second set of zeros another velocity is taken and then the pitching moment. This routine is repeated again at constant frequency so that redundant lift and pitching moment readings are obtained with sets of zeros before and after each force reading. The data taking is similar for the drag balance except that only one force is being read. This process is repeated at each of the frequencies investigated.

The ventilation runs are similar in that the bridges and amplifiers are balanced with the model stationary and the RSA outputs are zeroed with shorted input. The primary difference lies in that the frequency is fixed not just for a "block" of data but for an entire "run". The parameter varied within the run is the air supply rate.

Data Reduction.

The data reduction was accomplished for the most part with the aid of an electronic digital computer. The calibrations and data reduction are intimately tied together, consequently some overlap with the previous section on calibrations must be expected. The equations defining the calibration coefficients and their use in the data reduction are presented here.

1. Force Coefficients.

We will assume that the hydrofoil is performing a simple harmonic heaving motion. The vertical displacement transducer output is then given by a relation of the form

$$y = F_1 A' \sin \omega t \tag{1}$$

where y is the vertical displacement transducer output, F_1 the displacement calibration coefficient obtained as described previously and A' is the amplitude. Feeding this displacement signal into the RSA we get (all RSA output signals will be denoted by tildes)

$$\tilde{y} = C A' F_1 \tag{2}$$

where C is some constant associated with the Fourier analysis performed by the RSA.

Because the motion is simple harmonic the velocity transducer output can be written in the form

$$\dot{y} = F_2 A' \omega \cos \omega t . \tag{3}$$

This can also be thought of as the defining relation for the velocity calibration factor, F_2. The signal becomes, after processing by the RSA,

$$\tilde{\dot{y}} = F_2 C A' \omega \tag{4}$$

or substituting equation (2) into equation (4) we get

$$\tilde{\dot{y}} = F_2 \frac{\tilde{y}}{F_1} \omega . \tag{5}$$

Solving equation (5) for F_2 shows us explicitly how we may obtain this calibration factor

$$F_2 = \frac{F_1}{\omega} \frac{\tilde{\dot{y}}}{\tilde{y}} \tag{6}$$

The acceleration is also directly related to the velocity and since we know the value of the calibration mass we can use Newton's Second Law to infer the force output.

$$F = -mF_3 A' \omega^2 \sin \omega t \tag{7}$$

This equation defines the lift force calibration factor F_3 and m is the calibration mass (total). The signal as processed by the RSA is

$$\tilde{F} = -mF_3 CA' \omega^2. \tag{8}$$

Substituting equation (4) into equation (8) the RSA output becomes

$$\tilde{F} = -mF_3 \omega \frac{\tilde{\dot{y}}}{F_2} \tag{9}$$

and solving this expression for F_3 we get equation (10).

$$F_3 = -\frac{F_2}{m\omega} \frac{\tilde{F}}{\tilde{\dot{y}}} \tag{10}$$

The rms dynamic lift is then related to the RSA output signal through the factor F_3.

$$\tilde{L}_{r,i} = L_{r,i} \cdot F_5 \tag{11}$$

The subscripts r and i have been used to denote the force components in-phase with the apparent change of angle of attack and 90^o out of phase.

The apparent change of angle of attack is given by

$$\bar{\alpha} = \frac{-\tilde{\dot{y}}}{UF_2} . \tag{12}$$

The in-phase lift coefficient is then defined by and calculated using equation (13).

$$C_{L_{\bar{\alpha}_r}} = \frac{L_r}{\frac{1}{2}\rho U^2 A\bar{\alpha}} = \frac{2F_2}{\rho UAF_3} \frac{\tilde{L}_r}{\tilde{\dot{y}}} \tag{13}$$

The quadrature lift coefficient is then defined by and calculated using equation (14).

$$C_{L_{\bar{\alpha}_i}} = \frac{L_i}{\frac{1}{2}\rho U A \bar{\alpha}} = \frac{2F_2}{\rho U A F_3}\left(\frac{\tilde{L}_i}{\tilde{y}} - \frac{m' F_3 \omega}{F_2}\right) \tag{14}$$

The second term in parentheses in equation (14) represents the force due to the acceleration of the model's and the live mass of the balance. The total live mass is m'.

The pitching moment calibration is similar. The calibration mass m has its center of gravity at a distance ℓ from the electrical center of the balance. This offset causes a moment as the mass is accelerated vertically. The moment signal can be expressed in the form

$$M = m \ell F_4 A' \omega \sin \omega t. \tag{15}$$

This equation defines the pitching moment calibration factor F_4 and the processed signal can be expressed as

$$\tilde{M} = m \ell F_4 C A' \omega^2. \tag{16}$$

Substituting equation (4) into equation (16) and solving for the calibration factor F_4 we get

$$F_4 = \frac{F_2}{m \ell \omega} \frac{\tilde{M}}{\tilde{y}}. \tag{17}$$

The rms dynamic pitching moment is related to the RSA output signal through the factor F_4.

$$\tilde{M}_{r,i} = M_{r,i} \cdot F_4 \tag{18}$$

The in-phase pitching moment coefficient is then defined by and calculated using equation (19).

$$C_{M_{\bar{\alpha}_r}} = \frac{M_r}{\frac{1}{2}\rho U^2 A c \bar{\alpha}} = \frac{2F_2}{\rho U A F_4 c} \frac{\tilde{M}_r}{\tilde{y}} \tag{19}$$

The quadrature pitching moment coefficient is defined by and calculated using equation (20).

$$C_{M_{\bar{\alpha}_i}} = \frac{M_i}{\frac{1}{2}\rho U^2 Ac\bar{\alpha}} = \frac{2F_2}{\rho UAF_4 c}\left(\frac{\tilde{M}_i}{\tilde{\gamma}_y} - \frac{m' \ell' F_4 w}{F_2}\right) \tag{20}$$

The distance of the total live mass from the electrical center of the balance is ℓ' and m' is as for the lift. The pitching moments as given above are for moments about the electrical center of the balance. To obtain moments about a parallel axis through the model planform's centroid we must have drag data.

The drag is reduced in much the same way. The drag calibration factor is obtained statically and is the same for all frequencies. Also, because the motion is perpendicular to the direction that the force is being measured there is no live mass tare. The drag force is related to the RSA output by

$$\tilde{D}_{r,i} = D_{r,i} \cdot F_5 \tag{21}$$

and the drag coefficients are given by

$$C_{D_{\bar{\alpha}_{r,i}}} = \frac{D_{r,i}}{\frac{1}{2}\rho U^2 A\bar{\alpha}} = \frac{2F_2}{\rho UAF_5}\frac{\tilde{D}_{r,i}}{\tilde{\gamma}_y}. \tag{22}$$

2. Ventilation Parameters.

The additional data taken during the ventilation runs were reduced to dimensionless parameters as follows.

The cavity length was measured with an ordinary rule and the number divided by the model chord length to produce a dimensionless cavity length.

The air supply rate was measured with a Fischer-Porter flow meter and the supplyrate reduced to standard cubic feet per second using calibration information provided by the manufacturer. An air supply coefficient was defined as

$$C_Q = \frac{Q}{UA \sin\alpha}.$$

This has the meaning of a column of air of cross-sectional area equal to the projected frontal area of the foil and moving at free stream velocity.

The ventilation number is analogous to the cavitation number and is defined by

$$\sigma_v = \frac{P_\infty - P_c}{\frac{1}{2}\rho U^2}.$$

The cavity pressure was measured by a manometer connected to the ventilation strut. The pressure drop in the strut was calibrated as a function of the air flow rate so that the cavity pressure reading could be adjusted accordingly.

IV. Discussion of the Experimental Data and Theoretical Calculations.

The first portions (A, B) of the discussion are concerned with the dynamic measurements of the delta wing hydrofoils in fully wetted and forced-ventilated flow. Then in (C) the experiments concerned with steady planing flow and the relevant theory are described. The results of the dynamic planing tests and comparison with the theory outlined in Appendix II are then described in (D, E). Section (F) describes the work carried out in the High Speed Water Tunnel on two-dimensional non-steady hydrofoils.

A. Fully Wetted Flow.

The fully wetted results are separated into that for the 15° delta wing and that for the 30° delta wing. Figures 9, 10 and 11 present the unsteady lift, drag and pitching moment about the planform centroid for the 15° delta wing at 0.83 chords submergence. Figures 12, 13 and 14 present the same data at 0.50 chords submergence and Figs. 15, 16 and 17 are for a submergence of 0.17 chords.

Also shown on Fig. 9 is the effect of reduced frequency on the unsteady lift as calculated by Lawrence and Gerber (24). Because they did not present data for the aspect ratios tested, the results used here are interpolated from their tabular values. Their results agree quite well with the present experiments, as can be seen from the figure, for zero angle of attack.

There is a sizable non-linear angle of attack effect on the in-phase lift but almost no effect on the quadrature lift. The non-linear effect is presumably due to leading edge separation since the foils have sharp edges. The quadrature lift seems to be an apparent mass effect since it is linear in reduced frequency but the slope is somewhat smaller than that calculated using the "linear" model.

The in-phase drag data also exhibit a non-linear effect greater than the projection of a linear value of normal force. One expects the lift and drag forces to be related by the angle of attack since due to the separated edges the loading should be mostly normal to the foil. The in-phase drag exhibits a fairly large reduced frequency effect at non-zero angles of attack. This is believed to be a real effect, not an experimental problem. The quadrature drag is about as expected except

for reduced frequencies less than one where the data are independent of angle of attack.

The in-phase pitching moment is very small for the 15^{o} delta wing. A slight pitch-up moment is noted which is no doubt due to the flow not being conical near the trailing edge. The reason for the unsual behavior of the quadrature pitching moment with angle of attack is not known.

Figures 12, 13 and 14 illustrate that the free surface effect is negligible at 0.50 chords submergence. At 0.17 chords submergence, illustrated in Figs. 15, 16 and 17, there is a noticeable free surface effect. All of the values are reduced slightly. What is particularly noticeable, however, is that the quadrature lift and drag are negative at low reduced frequency, particularly at the largest angle of attack. It might be expected that since this is a surface effect it might be Froude number dependent but no investigations of this point were undertaken.

Recent theoretical treatments of delta wings have been primarily concerned with the description of the flow resulting from the leading edge separation. This separation produces a sizable non-linear effect as was noted in the data. Figure 18 presents a summary of the major steady theories calculated for the 15^{o} delta wing at each of the angles of attack tested. Also presented on this graph for comparison only is the mean of the present experimental dynamic data for the various reduced frequencies tested at each of the angles of attack. Of course we do not expect the dynamic results to be applicable for the steady state case except in the limit of zero reduced frequency. But the variation in the in-phase lift coefficients with reduced frequency over the range tested

is not large as, for example, is shown in Fig. 9, so we may reasonably expect some degree of correlation between the two. We see that the zero angle of attack value is fairly well predicted by Jones' steady state method. The agreement with the Brown-Michael theory is not good and appears to get worse with increasing angle of attack. The Mangler-Smith theory also does not show good agreement but it may be better at even higher angles of attack. The theory which is by far the best is that of Gersten. The experimental data and theory actually overlap at six degrees but underestimates the lift at twelve degrees. This might indicate that Gersten's theory is better for small angles of attack, say $\alpha < \beta$. It would be interesting to compare the Mangler-Smith theory for $\alpha > \beta$; unfortunately no data were taken for that range of angles of attack.

Figures 19, 20 and 21 present the unsteady lift, drag and pitching moment coefficients for the 30° delta wing at 0.83 chords submergence. Figures 22, 23 and 24 present the same data at 0.50 chords submergence and Figs. 25, 26 and 27 at 0.17 chords submergence.

Figure 19 also shows the effect of reduced frequency as calculated by Lawrence and Gerber. As for the 15° foil the agreement with the zero angle of attack data is quite good for both in-phase and quadrature lift.

There is a significant non-linear angle of attack effect on the in-phase experimental data. As for the more slender model the quadrature lift is almost independent of angle of attack.

The in-phase drag exhibits marked angle of attack and reduced frequency effects. The reason for the negative in-phase drag at zero angle of attack is not known. The nearness of the quadrature drag to zero at zero angle of attack seems to indicate that the foil is perpendicular

to the oscillation. The effect, or lack thereof, of angle of attack on the quadrature drag for reduced frequencies less than one is much the same as for the 15° foil.

The pitching moment exhibits a larger value for the 30° foil presumably because the model is not really a slender body and the reduced loading on the aft of the foil increases the moment.

Figures 22, 23 and 24 present the data for 0.50 chords submergence. The submergence effect is very small but the data serve as a useful check on the data at 0.83 chords submergence.

The effect of the free surface is quite noticeable in Figs. 25, 26 and 27, which are for a submergence of 0.17 chords. The effect is most noticeable at the largest angle of attack for which the free surface is quite distorted. These three figures illustrate the facts that the effect of the free surface is small unless the foil is quite close and also that if the foil is close the effect can be large.

Figure 28 presents the effect of oscillation amplitude on the unsteady lift coefficient. The oscillation amplitude is labeled with a voltage since it is that which is fed into the force servo controller. The nominal voltage was 4 v. and this series of runs was accomplished at 2 v. and 3 v. to establish the linearity of the effect so that the coefficients could be justifiably normalized by the apparent angle of attack change. The validity of this assumption is well substantiated by the data with only a few spurious points not collapsing together.

Figure 29 presents the effect of using different frequency-velocity combinations to obtain various reduced frequencies. As can be seen from the agreement of the data at the same reduced frequencies and the

smooth behavior with reduced frequency, this is the proper reduction parameter.

Data were also taken at negative six and twelve degrees angle of attack. These data are typified in Fig. 30. Little effect of reversing the sign of the angle on the quadrature lift is noted.

Figure 31 presents a summary of the major steady theories calculated for the 30° delta wing at each of the angles of attack tested. Also presented for comparison in the same manner as that in Fig. 18 is the mean of the experimental data at different reduced frequencies for each of the angles of attack. The zero angle of attack value is now not as accurately predicted by Jones' theory as it was for the 15° wing, presumably because the 30° wing is not really "slender". Both the Brown-Michael and Mangler-Smith theories give poor agreement with the experimental data. As for the 15° model Gersten's theory is by far the best. It should be emphasized that we are comparing here results of dynamic tests averaged over a range of frequencies with calculations from steady state theories. While the experimental results of in-phase lift coefficient for the 15° wing do not show much change with reduced frequency, those for the 30° wing do particularly at the lower reduced frequencies and highest angle of attack (see again Fig. 19). For this reason the average of the present dynamic data at the higher angles of attack is an incorrect basis of comparison; uncertainties in extrapolating the experimental data to zero reduced frequency led us instead to make the present comparison. Even on the basis of these comparisons shown in Fig. 31 and the other examples it is clear that much more remains to be done in order to predict non-steady forces of fully wetted delta wings at moderate angles of attack.

B. Ventilated Flow.

It was originally intended to test both models with ventilated cavities but only the 30^{o} apex angle delta wing was tested for reasons previously described. Also due to the additional parameter cavity length, and associated parameters cavity pressure and air supply rate, the tests were limited to one submergence and one angle of attack. These investigations were not intended to be as extensive as the other measurements but were intended as a first look into a previously uninvestigated area.

Figures 32 and 33 present the unsteady lift and drag coefficients at various cavity lengths and reduced frequencies. The behavior of the coefficients with cavity length is odd but not entirely unexpected in view of the findings of Klose (2). Projections of the steady values of C_{N_α} calculated by Kaplan, et al (26) using the Cumberbatch-Wu theory at a cavitation number of zero are also presented on the figures. It can be seen from the figures that this underpredicts the experimental data at the lowest reduced frequency and largest cavity length (i. e., lowest ventilation number).

Although it was not possible in this series of investigations it would be very interesting to have measurements of the unsteady cavity pressure during the oscillation cycle. Before a valid model can be established to attempt the calculation of the unsteady forces, more investigation needs to be done to find the proper boundary conditions.

The measured average ventilation number and average air supply coefficient were also determined as a function of cavity length and are shown in Figs. 34 and 35. There is a direct correlation of ventilation

number with cavity length independent of reduced frequency. The same situation seems to exist for air supply coefficient at least at the lower cavity lengths, although for longer cavity lengths a great deal of scatter becomes apparent. This may be due in part to the difficulty in determining the cavity termination point especially when the cavity is long, but may also be associated with the change in the entrainment mechanism at the terminus of the cavity which is well known to occur with steady cavity flow in the presence of gravity.

High speed flash photographs of four ventilated flows are presented in Fig. 36. Photograph (a) shows a low reduced frequency and fairly short cavity. The bursts of bubbles entrained in the wake are due to the basic flow, not the forced oscillation. The frequency of the heaving oscillation is much lower than the shedding frequency. Photograph (b) presents a higher reduced frequency and slightly shorter cavity length. The oscillation may be seen in the sinusoidal mean position of the wake. As can be seen in all the photographs the entrainment in the region of cavity closure makes determination of the cavity length difficult. Photograph (c) shows a higher reduced frequency still and a cavity length about the same as in the first case. The bubbles entrained into the shed vorticity are clearly seen. Photograph (d) shows the same reduced frequency as (c) but with a longer cavity length. The waves on the cavity wall are easily seen. The large quantity of air in the wake illustrates why this case has the largest air supply coefficient.

It might be noted that all the cavities are smooth along the first half chord and not over the aft part. The reason for this is that the supporting strut causes spray which disturbs the cavity wall.

C. Steady Planing of Delta Wings.

Although a rather large literature on the planing phenomenon has developed over the years, the flat triangular surface or delta wing has received very little attention. Most experimental work has been concerned with planing of prismatic bodies having a definit "Vee" in the cross-flow plane or simpler profiles such as a flat rectangular planing surface. In fact we have been unable to find any experimental work on planing of flat delta plan forms; the only theoretical treatments are those of Tulin (Ref. 30) already mentioned and Maruo (Ref. 34). As the Tulin theory forms the basis of the non-steady planing measurements reported in the next section it seemed to be advisable to undertake a brief investigation of the steady planing of delta wings and to compare the results of this theory with experimental observations.

The slender body planing theory of delta wings is laid out in Appendix II. The final results for steady planing are contained in Eq. A-65 and an additive term accounting for the effect of gravity, Eq. A-72. First we present the results of the measurements themselves. These are summarized in Fig. 37 where the lift coefficient versus angle of attack is given for delta wings having apex angles of 10°, 15°, 30°, 45° and 60°. The chord of these foils ranged from about 5 inches to about a foot and this together with the variable flow velocity in the tunnel is responsible for the different Froude numbers shown in the legend of the figure. It will be noticed that there is a distinct Froude number effect though it is not very large. These same results are replotted and compared with the theory of Appendix II for the 10°, 15° and 30° apex angles in Figs. 38, 39 and 40 respectively. On the whole the theoretical

predictions are in reasonable agreement with the observations. As is discussed at some length in the appendix, this theory is limited to small apex angles and to angles of attack much smaller than the apex angle. Thus the domain of validity is, strictly speaking, rather small for the 10° apex angle case and we see in Fig. 38 that for angles of attack of 14° or less, the theory rather underpredicts the observed lift. Presumably at the lowest angle, $\alpha = 4^{\circ}$, the theory should become applicable; and it appears to do so. These same trends are also in evidence for the other two angles shown except that the theory becomes relatively more successful although it appears in Fig. 40 that for an apex angle of 30°, the theory now actually overpredicts the lift force. No doubt this is due to the breakdown of the "slenderness" assumption of the theory. At the higher apex angles, the present theory seriously overpredicts the observed lift and for that reason, these comparisons are not shown.

Also shown in Figs. 38 and 39 are the results of the calculations of Cumberbatch and Wu (Ref. 27) for the lift coefficient of a slender delta wing in fully cavitated flow with zero cavitation (or ventilation) number. This calculation is in many respects similar in spirit to that in Appendix II. However, because the flow is unbounded and there is no free surface they were able to carry out a much more exact calculation. Of course their results should not really be applicable for small angles of attack (where the present theory holds) but instead should become applicable when $\alpha > \beta^{*}$. In fact, we see that the experimental results closely approach this theory for large angles of attack.

---

*This follows on the intuitive ground that in the cross flow plane the foil is then submerged one span beneath the free surface – which effect should then be small.

All slender body theories predict that the center of pressure (for flat uncambered profiles) is at the planform centroid. Measurements of the center of pressure for the family of delta wings are reported in Fig. 41. There we see that this slender body prediction is clearly not followed. These results can be explained by a decrease in lift near the trailing edge (in fact it must vanish there) to cause the forward movement of the center of pressure. This is, then, an inherent defect of slender body theory. Nevertheless, it appears that this theory is able to provide reasonable estimates of the steady lift coefficient for planing delta wings. We next turn to the dynamic planing experiments.

D. Dynamic Planing Measurement of Delta Wing Hydrofoils Oscillating in Heave.

Both the 15° and 30° delta wing models were tested dynamically in planing. Angles of attack of six and twelve degrees were run for each of the models. Only one free stream velocity was run ($U = 22$ ft/sec) since this was as high as practical and the heaving amplitude was kept as small as practical to lessen the wetted area change.

Figures 42, 43, and 44 present the unsteady lift, drag and pitching moment coefficients for the 15° delta wing. Also shown on the figures are the theoretical calculations of Appendix II. The agreement of the theory and the in-phase lift is poor which is not too surprising for this foil since the theory was developed for small ratios of angle of attack to apex angle. The logarithmic behavior of the theory appears to be too strong compared to the other non-linear term and thus like the steady case the in-phase lift coefficient is underpredicted. The quadrature lift, on the other hand, is quite accurately predicted with the

experimental points lying along the predicted line. The drag force is slightly better predicted by the theory although the smallness of the values makes the agreement seem better than it really is. The quadrature drag is negative below a reduced frequency of one-half for the experimental data. It is unknown if this is a real planing effect. The pitching moment data exhibit much the same behavior as for the fully wetted flow. It is interesting that the dynamic tests show that the center of pressure is forward of the planform centroid just as for steady planing.

Figures 45, 46 and 47 present the unsteady lift, drag and pitching moment data for the planing 30° delta wing. Also given on the same graphs are the results from the theory of the appendix calculated for these cases. It would be expected that since the angle of attack to apex angle ratio is substantially less than for the 15° apex angle case, the theory would predict more accurately the experimental values for the in-phase lift. This does not appear to be the case and the relative difference is about the same for the two apex angles, but the quadrature lift is again predicted quite accurately.

The in-phase drag seems again to be predicted more accurately than the lift but the difference is more apparent than real. The quadrature drag is somewhat overpredicted by the theory, perhaps because the 30° foil is not really a very slender body. The pitching moment data again show that the center of pressure is forward of the foil planform centroid.

Figure 48 presents high speed flash photographs of the 30° delta wing planing at three reduced frequencies. The angle of attack is only

six degrees in this case, consequently the cavity is shallower than for the other case where the angle of attack was 12^{o}. The distortions in the cavity due to the oscillation are evident in the bottom picture, especially the one of higher reduced frequency.

E. Part-Cycle-Planing.

In the course of the planing experiments it was discovered that if the foil was oscillated such that it was planing during the upper part of the cycle and fully wetted during the lower part of the cycle, the phase of the lift force would change drastically. This striking effect has been named "part-cycle-planing". During this part-cycle-planing phenomenon the in-phase lift coefficient could actually become negative which would mean that an elastically mounted foil could be dynamically unstable. It was also readily apparent that the amplitude of the foil displacement governed the magnitude of the in-phase lift coefficient (unlike the usual case) and that if the amplitude were sufficiently large this component of the lift force would pass through zero and become positive again. The amplitude for which the in-phase lift is zero (integrated over a cycle) determines the condition of neutral stability. This was determined empirically for the 30^{o} delta for several tunnel velocities as a function of reduced frequency and is shown in Fig. 49. Rather surprisingly different boundaries are found for each speed; this would indicate that either gravity or perhaps surface tension might play an important role.

It should be mentioned that for the usual planing experiments the tip of the foil was always positioned so that it just emerged above the undisturbed water surface. The part-cycle phenomenon would occur

when the mean position of the foil was lowered slightly so that the tip became submerged during part or most of the cycle. With further immersion the upper surface of the foil would become fully wetted at all times and the anomolous results of part-cycle-planing would give way to the well-behaved conditions of fully wetted flow.

Two high speed flash photographs of the 30° delta wing operating in the part-cycle-planing mode are presented in Fig. 50. In the upper photograph the foil has just ceased to plane. The cavity is almost unchanged except at the front of the foil. In the lower picture the cavity has collapsed and only the ventilated leading edge vortices remain.

F. Some Two-Dimensional Experiments on Hydrofoils Oscillating in Heave.

The availability of the dynamic measuring system was an inducement to consider making additional experiments in the two-dimensional test section of the high speed water tunnel at Caltech. We had been somewhat reluctant to do this in the past because of the experimental problems associated with mounting of the hydrofoil-strut assembly in the test section, and because of the problem of maintaining a water-tight seal on the dynamic balance over the range of static pressures and tunnel velocities to be experienced. After some consideration the hydrofoil driver unit was attached to a special mounting plate which was bolted to the frame of the tunnel. The piston of the driver communicated to the working section through a hole drilled through the upper window of the tunnel; the mounting plate contained an additional O-ring seal which

prevented tunnel water when pressurized from entering the hydraulic piston. The strut assembly was then attached to the piston. A thin plate was fastened over the opening between the tunnel and the small plenum formed by the hole in the upper window; it had a contoured opening in it which permitted the strut to pass through.

The supporting strut was about 12 inches long and the tunnel height is 30 inches, so that the dynamic model was not mounted on the center line. Strut inserts to locate the model on the tunnel center line were made but it was found that with the longer length of strut the natural frequency of resulting structure in fore-and-aft bending was too low, so the off-center mounting had to be accepted. The model was then attached to the strut with about 0.010 inches tip clearance on either side and the tunnel section closed up. We were concerned that the strut might wobble from side to side in its heaving motion and thereby impart erroneous forces, not to mention the possibility of damaging the balance. We were agreeably surprised to find that at tunnel speeds of about 30 feet per second, the strut-foil system tracked up-and-down in a true vertical line and that running gap clearances as low as 0.005 inches could be easily maintained.

Providing a continuous and reliable waterproof seal on the balance was another matter, however. The range of tunnel static pressure was from nearly the vapor pressure of water to about one atmosphere gage. The waterproofing consisted only of two layers of a thin latex sheet cemented to the balance and because of this, only a small pressure difference between the internal cavity of the balance and the exterior flow can be supported. The initial tests were made with this internal pressure

approximately 1/4 psi above the tunnel ambient pressure to prevent leaks into the cavity. This approach had to be abandoned, however, because under the action of flow (about 30 feet per second) this slight positive pressure together with the surrounding pressure field would peel off the waterproofing layers and short out the electrical connections of the strain gages. It was then found that the waterproofing layer could be made to withstand a good vacuum without pinhole leaks developing. Consequently the experiments were then made with the pressure inside the balance maintained at about 2 mm Hg absolute.

A photograph of the foil-strut assembly in the water tunnel is shown in Fig. 51. The off-center position of the foil is clearly seen as is the rather extensive development of cavitation on the supporting strut as well as the force balance itself. In the case of Fig. 51, the cavitation bubble is considerably longer than the chord; in achieving this condition the tunnel ambient pressure is lowered gradually and it is thereby necessary to pass through a condition of extremely unsteady partial cavitation. We were apprehensive that these unsteady loads – especially in roll moment – might destroy the forces balance. The partially cavitating region was therefore passed through as quickly as possible and for this reason no dynamic measurements were made in this important regime.

Instead, the dynamic experiments were limited to two brief sets of measurements, one fully wetted and the other fully cavitated. The fully wetted experiments were carried out on a flat plate hydrofoil having a sharpened leading edge and a sharpened trailing edge. The chord was 6 inches and the thickness was 1/4 inch; the span was a nominal

6 inches and as the strut length was nominally 12 inches, the hydrofoil was mounted 2 chords from the upper window and 3 chords from the lower. Tunnel speed was nominally 30 feet per second and the oscillation frequency from about 2 - 25 Hz.

Results of the dynamic measurements in heave for mean angles of attack of zero and 6° in fully wetted flow are shown in Fig. 52. The ordinate and abscissa have been divided by 2π. Also shown for reference are the predictions of linearized unsteady two-dimensional lifting surface theory without wall corrections. Whatever the influence of the latter it can be seen that the linear theory (see for example Ref. 1) gives a reasonable estimate of the unsteady forces except that the magnitude of the experimental lift force vector is low; the phases are in reasonable agreement. Although the experimental results for $\alpha = 0^{\circ}$ hold no real surprises, we were quite surprised at the outcome of the $\alpha = 6^{\circ}$ tests. There, as Fig. 52 clearly shows, the theory does not account for the observations except in a qualitative way. Not only is the lift magnitude larger (than estimated) but the phase is quite different, first leading then lagging the theoretical estimate as the frequency increases. These results, we feel, are clearly due to the existence of the sharp leading edge; similar experiments by other workers on rounded hydrofoils do not show such a pronounced angle of attack effect. While the cause of this effect was not investigated through more detailed studies, it seems plausible that a separation bubble or vortex must be formed dynamically at the sharp leading edge. The possibilities here for both experimental work and analysis are quite challenging.

As indicated above, dynamic measurements in fully cavitating flow presented certain instrumentation problems. There are also

additional questions of perhaps a facility nature that also arise, but before discussing these let us turn to Fig. 53 which gives in graphical form the principal experimental results. In this figure are presented both components of the dynamic lift in heaving motion of a flat hydrofoil in fully cavitating flow. The mean angle of attack is 8^{o} (unlike the photo of Fig. 1). Again these experimental findings are compared with existing unbounded flow theory for cavitating hydrofoils having infinitely long cavities. As in the fully wetted case there is qualitative agreement between the two. However, in the present case we are not really certain just how to interpret the experimental results.

For one thing, it is almost certain that wall effects will certainly be much more important in non-steady cavity flow than corresponding fully wetted flow; perhaps another more serious question is the effect of the fluctuating cavity volume upon possible pressure fluctuations in the tunnel circuit. Also, from Fig. 51 it can be seen that the flow is not strictly two-dimensional because of the cavity attached to the supporting strut. At the moment it is difficult to say just which of these effects is the more important or even if the results observed are typical of unbounded cavity flow. It was in fact because of these reservations that a more extensive experimental program of non-steady cavity flows in the high speed water tunnel was not undertaken.

The results of Fig. 53 as they stand, however, are not without interest. The data for the choked tunnel (i. e., the cavity disappearing into the tunnel diffusor) are very similar to the unbounded flow case except that the real part of the lift coefficient is about 70-80 percent of the theoretical unbounded value and for practical values, the same can

be ascribed to the imaginary part too. The behavior with reduced frequency is also rather similar and is quite unlike the usual fully wetted flow. It is possible that these differences are purely wall effect problems and this possibility is now being examined theoretically on another contract.* In addition, it would be expected by analogy with steady cavity flows past lifting surfaces that shorter cavities would exhibit higher in-phase lift coefficients than with infinitely long cavities. Such an effect is observed in Fig. 53, but we have no such guide for the imaginary part which appears to decrease when the cavity becomes shorter. Clearly, this whole area, especially with partially cavitating hydrofoils, is in need of further research.

V. Summary and Concluding Remarks.

The present report includes a fairly extensive series of experiments on the unsteady forces of delta wings oscillating in heave in three different modes: fully wetted, planing and forced ventilated. In addition further experiments were carried out on steady planing delta wing hydrofoils. A quasi-steady extension of Tulin's theory was made to interpret the dynamic force measurements; this same theory was also used to estimate the forces in steady planing.

Generally speaking, the theory gave a reasonable estimate. The steady forces and the quadrature lift forces in dynamic planing were also well estimated. However, the in-phase dynamic lift force was not well predicted by the theory, generally it was about 25 percent low and did not indicate the observed changes with reduced frequency. Also, a new unstable planing phenomenon associated with slightly submerged delta wings was found.

---

*Contract Nonr 220(59).

The dynamic measurements on forced-ventilated delta wings are new and they reveal that the presence of the ventilated cavity materially changes the dynamic forces just as similar experiments on two-dimensional hydrofoils have.

The fully wetted dynamic measurements were found to be well correlated with existing lifting surface theory for zero mean angle of attack. However these dynamic coefficients are not well correlated by existing theories at angles of attack of 6° and 12°.

Some additional experiments on two-dimensional foils in a closed water tunnel were also carried out. Dynamic measurements on a heaving flat plate foil with sharp leading edge showed quite good agreement with existing non-steady theoretical predictions; there was a pronounced effect of angle of attack, and it was suggested that a transient leading edge separation bubble could be responsible for this effect. Dynamic measurements on fully cavitated hydrofoils were also carried out in the closed tunnel; this raised certain problems of interpretation of the results, specifically the question of wall effect, tunnel dynamics and lack of flow two-dimensionality due to the cavitating supporting strut. While the observed forces are in qualitative agreement with unbounded flow theoretical predictions, many experimental and theoretical problems remain to be solved.

As a general remark it was found that at reasonable angles of attack, say 12°, none of the existing dynamic theories would adequately predict the observed forces in any of the above modes for slender delta wings, and that as a rule the in phase lift force was greater than estimated.

VI. References.

1. H. N. Abramson, W.-H. Chu and J. T. Irick, "Hydroelasticity with Special Reference to Hydrofoil Craft", Naval Ship Research and Development Center, Report 2557, September 1967.

2. G. J. Klose, "Unsteady Forces on Oscillating Hydrofoils", Ph. D. Thesis, California Institute of Technology, 1966.

3. G. J. Klose and A. J. Acosta, "Unsteady Force Measurements on Fully Wetted Hydrofoils in Heaving Motion", J. Ship Res. 12, pp. 69-80, March 1968.

4. J. H. B. Smith, "Improved Calculations of Leading-Edge Separation from Slender Delta Wings", R. A. E. Tech. Rept. No. 66070, March 1966.

5. R. T. Jones, "Properties of Low-Aspect-Ratio Pointed Wings at Speeds Below and Above the Speed of Sound", NACA Report 835, 1946.

6. M. Roy, "Caracteres de l'Ecoulement autour d'une Aile en Fleche Accentuee", C. R. Acad. Sci., Paris, 234, 2501, 1952.

7. R. Legendre, "Ecoulement au Voisinage de le Point Avant d'une Aile a Forte Fleche aux Incidences Moyennes", 8th Int. Cong. Th. Appl. Mech., Istanbul, 1952, Rech. Aero., No. 30, 1952 and Rech. Aero., No. 31, 1953.

8. M. C. Adams, "Leading-Edge Separation from Delta Wings at Supersonic Speeds", J. Aero. Sci., 20, p. 430, 1953.

9. C. E. Brown and W. H. Michael, "On Slender Delta Wings with Leading-Edge Separation", NACA TN 3430, April 1955. Also J. Aero. Sci., 21, pp. 690-694 and 706, 1954.

10. R. H. Edwards, "Leading-Edge Separation from Delta Wings", J. Aero. Sci., 21, pp. 134-135, 1954.

11. K. W. Mangler and J. H. B. Smith, "A Theory of the Flow Past a Slender Delta Wing with Leading Edge Separation", Proc. Roy. Soc. A, 251, pp. 200-217, 1959 (R. A. E. Rept. Aero 2593, 1957).

12. K. Gersten, "Calculation of Non-Linear Aerodynamic Stability Derivatives of Aeroplanes", AGARD Rept. No. 342, April 1961.

13. D. J. Marsden, R. W. Simpson and W. J. Rainbird, "The Flow Over Delta Wings at Low Speeds with Leading-Edge Separation", College of Aeronautics Rept. No. 114, ARC 20409, 1957.

14. D. Küchemann, "Report on the I. U. T. A. M. Symposium on Concentrated Vortex Motions in Fluids", J. Fluid Mech. 21, pp. 1-20, January 1965.

15. M. Roy, "On the Rolling-Up of the Conical Vortex Sheet above a Delta Wing", Prog. in Aero. Sci., 7, pp. 1-5, 1966.

16. R. Legendre, "Vortex Sheets Rolling-Up along Leading-Edges of Delta Wings", Prog. in Aero. Sci., 7, pp. 7-33, 1966.

17. J. H. B. Smith, "Theoretical Work on the Formation of Vorted Sheets", Prog. in Aero. Sci., 7, pp. 35-51, 1966.

18. H. C. Garner and D. E. Lehrian, "Non-Linear Theory of Steady Forces on Wings with Leading-Edge Flow Separation", A. R. C. R & M No. 3375, 1964.

19. J. W. Miles, "On Non-Steady Motion of Slender Bodies", Aero. Quart. 2, pp. 183-194, 1950.

20. I. E. Garrick, "Some Research on High-Speed Flutter", Proc. Third Anglo-American Aero. Conf., 1951, pp. 419-446.

21. D. G. Randall, "Oscillating Slender Wings with Leading-Edge Separation", Aero. Quart., Vol. 17, pp. 311-331, 1966.

22. M. V. Lowson, "The Separated Flow on Slender Wings in Unsteady Motion", A. R. C. R & M No. 3448, 1967.

23. R. R. Maltby, P. B. Engler and R. F. A. Keating with an Addendum by G. F. Moss, "Some Exploratory Measurements of Leading-Edge Vortex Positions on a Delta Wing Oscillating in Heave", A. R. C. R & M No. 3410, 1965.

24. H. R. Lawrence and E. H. Gerber, "The Aerodynamic Forces on Low Aspect Ratio Wings Oscillating in an Incompressible Flow", J. Aero. Sci. 19, pp. 769-781, 1952; See also: Errata, J. Aero. Sci. 20, p. 296, 1953.

25. M. P. Tulin, "Supercavitating Flow Past Slender Delta Wings", J. Ship Res. 3, No. 3, 1959.

26. P. Kaplan, T. R. Goodman and C. C. Chen, "A Hydrodynamic Theory for Cavitating Delta Wing Hydrofoils", Oceanics Inc. Tech. Rept. No. 67-33, December 1966.

27. E. Cumberbatch and T. Y.-T. Wu, "Cavity Flow Past a Slender Pointed Hydrofoil", J. Fluid Mech. 11, Part 2, pp. 187-208, 1961.

28. H. Reichardt and W. Sattler, "Three-Component Measurements on Delta Wings with Cavitation", Max-Planck-Institut für Stromungsforschung, Göttingen, July 1962.

29. T. Kiceniuk, "Superventilated Flow Past Delta Wings", California Institute of Technology Engineering Division Rept. No. E-101.5, July, 1964.

30. M. P. Tulin, "The Theory of Slender Surfaces Planing at High Speeds", Forschungshefte fur Schiffstechnik, 4, 1956/57.

31. R. T. Knapp, J. Levy, J. P. O'Neill and F. B. Brown, "The Hydrodynamics Laboratory of the California Institute of Technology", Trans. ASME 70, July 1948, pp. 437-457.

32. G. Tricomi, "Integral Equations", Interscience Pub., Inc., New York, 1957, p. 173.

33. Bateman Manuscript Project, "Tables of Integral Transforms", Vol. II, McGraw-Hill Book Co., Inc., New York, 1954.

34. H. Maruo, "High- and Low-Aspect Ratio Approximation of Planing Surfaces", Schiffstechnik 72, May 1967, pp. 57-64.

VII. Acknowledgments.

The undertaking of any experimental investigation of the scope herein discussed must always require the participation of others. In particular we would like to thank Mr. R. Lyon of the Institute's Central Engineering Services and Messrs. C. Eastvedt, H. Hamaguchi, J. Kingan and C. Lundgren of the Hydrodynamics Laboratory. The assistance of Miss Cecilia Lin, Mr. H. Petrie, and Mr. M. Wilson in the preparation and proofreading of this manuscript is gratefully acknowledged. And finally, to Mrs. Phyllis Henderson and Mrs. Yvonne Vedder we express our most sincere appreciation, as well as to Miss Julie Wright who typed the final manuscript.

VIII. Figures and Captions.

Fig. 1 View of tunnel working section, electronic apparatus and hydraulic oscillator mounted in the working section. There is no water in the working section.

Fig. 2 Cross-section drawing of the hydraulic oscillator showing the tunnel mounting, balance (dynamometer) location and hydrofoil location.

Fig. 3 Photograph of the 15 and 30 degree apex angle delta wing hydrofoil models.

Fig. 4 The lift and pitching moment balance, seen from both sides, before affixing the strain gages.

Fig. 5 The drag balance, seen from both sides, without waterproofing.

Fig. 6 Diagram of the electronic equipment for the hydraulic oscillator and data acquisition.

Fig. 7 Photograph of the 30^{o} delta wing hydrofoil planing at a small angle of attack.

Fig. 8 Sketch of the actual cross flow of a planing delta wing at a small angle of attack.

Fig. 9 Unsteady lift coefficients for a fully wetted delta wing with 0.83 chords submergence at various angles of attack.

Fig. 10 Unsteady drag coefficients for a fully wetted delta wing with 0.83 chords submergence at various angles of attack.

Fig. 11 Unsteady pitching moment coefficients for a fully wetted delta wing at 0.33 chords submergence at various angles of attack.

Fig. 12 Unsteady lift coefficients for a fully wetted delta wing with 0.50 chords submergence at various angles of attack.

Fig. 13 Unsteady drag coefficients for a fully wetted delta wing with 0.50 chords submergence at various angles of attack.

Fig. 14 Unsteady pitching moment coefficients for a fully wetted delta wing at 0.50 chords submergence at various angles of attack.

Fig. 15 Unsteady lift coefficients for a fully wetted delta wing with 0.17 chords submergence at various angles of attack.

Fig. 16 Unsteady drag coefficients for a fully wetted delta wing with 0.17 chords submergence at various angles of attack.

Fig. 17 Unsteady pitching moment coefficients for a fully wetted delta wing at 0.17 chords submergence at various angles of attack.

Fig. 18 Summary of various steady theories of lift slope for a fully wetted 15° apex angle delta wing vs angle of attack together with the present experimental in-phase dynamic lift slope coefficient averaged over the reduced frequencies tested.

Fig. 19 Unsteady lift coefficients for a fully wetted delta wing of 30° apex angle with 0.83 chords submergence.

Fig. 20 Unsteady drag coefficients for a fully wetted delta wing of 30° apex angle with 0.83 chords submergence.

Fig. 21 Unsteady pitching moment coefficients for a fully wetted delta wing of 30° apex angle with 0.83 chords submergence.

Fig. 22 Unsteady lift coefficients for a fully wetted delta wing of 30° apex angle with 0.5 chords submergence.

Fig. 23 Unsteady drag coefficients for a fully wetted delta wing of 30° apex angle with 0.5 chords submergence.

Fig. 24 Unsteady pitching moment coefficients for a fully wetted delta wing of 30° apex angle with 0.5 chords submergence.

Fig. 25 Unsteady lift coefficients for a fully wetted delta wing of 30° apex angle with 0.17 chords submergence.

Fig. 26 Unsteady drag coefficients for a fully wetted delta wing of 30° apex angle with 0.17 chords submergence.

Fig. 27 Unsteady pitching moment coefficients for a fully wetted delta wing of 30° apex angle with 0.17 chords submergence.

Fig. 28 Unsteady lift coefficients on a fully wetted delta wing of 30° apex angle for various heaving amplitudes.

Fig. 29 Unsteady lift coefficients on a fully wetted delta wing of 30° apex angle showing the effect of various free-stream velocities.

Fig. 30 Unsteady lift coefficients for negative angles of attack on a fully wetted 30° apex angle delta wing hydrofoil.

Fig. 31 Summary of various steady theories of lift slope for a fully wetted 30° apex angle delta wing vs angle of attack together with the present experimental in-phase dynamic lift slope coefficient averaged over the reduced frequencies tested.

Fig. 32 Unsteady lift coefficients in forced ventilation flow past a 30° delta wing hydrofoil oscillating in heave for various frequencies. The number on each of the curves is the mean length of the ventilation cavity expressed in chords.

Fig. 33 Unsteady drag coefficients for the configuration of Fig. 32.

Fig. 34 Air supply coefficient as a function of cavity length showing the effect of reduced frequency.

Fig. 35 Ventilation number as a function of cavity length showing the effect of reduced frequency.

Fig. 36 Flash photographs of the ventilated cavity on the 30° delta wing at various reduced frequencies k and ventilation coefficients c_Q.

Fig. 37 Summary of experimental data for the steady planing lift coefficient of a family of delta wing hydrofoils vs angle of attack.

Fig. 38 Lift coefficient vs angle of attack for steady planing of a 10° delta wing.

Fig. 39 Lift coefficient vs angle of attack for steady planing of a 15° delta wing.

Fig. 40 Lift coefficient vs angle of attack for steady planing of a 30° delta wing.

Fig. 41 Location of experimentally measured centers of pressure (from the trailing edge) in steady planing vs angle of attack for the series of delta wings.

Fig. 42 Unsteady lift coefficients for the planing 15° delta wing.

Fig. 43 Unsteady drag coefficients for the planing 15° delta wing.

Fig. 44 Unsteady pitching moment coefficients for the planing 15° delta wing.

Fig. 45 Unsteady lift coefficients for the planing 30° delta wing.

Fig. 46 Unsteady drag coefficients for the planing 30° delta wing.

Fig. 47 Unsteady pitching moment coefficients for the planing 30° delta wing.

Fig. 48 High speed flash photographs of the 30° delta wing planing at three different reduced frequencies.

Fig. 49 Frequency-amplitude boundaries for neutral stability of the 30° planing delta wing during 'part cycle' planing.

Fig. 50 Flash photographs of 'part cycle' planing; the upper picture shows that part where normal planing occurs. The lower photograph shows that during a position of the cycle, the planing spray sheet collapses on the top of the foil so that it becomes partially wetted and only ventilated tip cavities remain.

Fig. 51 Photograph of the cavitating hydrofoil and support apparatus. The black covering over the supporting strut adjacent to the foil is the waterproofing for the balance shown in Fig. 4. The mean angle of attack shown is 16°.

Fig. 52 Unsteady lift coefficients in fully wetted heaving motion of a two-dimensional flat plate hydrofoil for various reduced frequencies and mean angles of attack. Reynolds number based on chord = 1.2×10^6. The diagram of the graph shows the relation of the hydrofoil to the tunnel working section.

Fig. 53 Unsteady lift coefficients in heaving motion of a naturally cavitating two-dimensional hydrofoil having a mean angle of attack of 8 degrees. These coefficients have been divided by $\pi/2$.

Fig. A-1 The coordinate system used to calculate planing loads.

Fig. A-2 The boundary value problem in the reduced cross flow plane.

Fig. A-3 Theoretical quasi-steady normal force slope.

APPENDIX I

Notation

$a(x)$	local semi-span
A	foil planform area
A'	heaving amplitude
b	spray position in reduced coordinates
b_1	$a(x)b$
$B(t)$	Bernoulli "constant"
c	model chord length
C	RSA factor
$C_{D_{\bar{\alpha}}}$	unsteady drag slope coefficient
$C_{L_{\bar{\alpha}}}$	unsteady lift slope coefficient
$C_{M_{\bar{\alpha}}}$	unsteady pitching moment slope coefficient about foil planform centroid
C_N	normal force coefficient
C_Q	air supply coefficient, $Q/UA \sin\alpha$
$\tilde{D}$	processed drag signal
f	reduced perturbation velocity potential
F	Froude number, $U/\sqrt{gc}$
F_1	displacement calibration factor
F_2	velocity calibration factor
F_3	lift calibration factor
F_4	pitching moment calibration factor
F_5	drag calibration factor

g	acceleration of gravity
k	reduced frequency, $\frac{\omega c}{2U}$; also dummy variable
ℓ	calibration mass offset
ℓ'	tare mass offset
$\tilde{L}$	processed lift signal
m	total calibration mass; also summing index
m'	tare mass
$\tilde{M}$	processed moment signal
n	summing index
N	normal force
p	pressure; also dummy variable
$\vec{q}$	velocity vector in foil coordinates
Q	air supply rate corrected to atmospheric pressure
t	time
U	free stream velocity
$\vec{v}_b$	velocity of foil coordinate system with respect to an inertial system
$\tilde{v}$	heaving velocity amplitude
x, y, z	coordinates attached to foil (See Fig. A-1.)
$y_0(x)$	foil camber function
α	angle of attack
$\bar{\alpha}$	apparent change of angle of attack
β	delta wing apex angle
$\gamma(\xi)$	local vortex strength
δ	ordering parameter
ϵ	$b(\xi)-1$
ϵ_1	$a(x)\epsilon$

ζ	dummy variable
η, ξ	reduced cross-flow plane coordinates (See Fig. A-2.)
θ	dummy variable
ν	defined to be $v_b + Uy_0' - U\alpha$
ρ	density of water
σ_v	ventilation number = $(p_\infty - p_c)/\frac{1}{2}\rho U^2$
τ	dummy variable
φ	perturbation velocity potential
Φ	total velocity potential
ω	oscillation angular frequency

Subscripts:

x, y, z η, ξ, t	differentiation by the subscripted variable (Note: dot above a symbol sometimes used for time differentiation and prime sometimes denotes differentiation by argument.)
c	cavity conditions
i	component leading apparent change of angle of attack by 90°
r	component in-phase with apparent change of angle of attack
∞	free stream conditions

APPENDIX II

A Theory of Unsteady Planing of Slender Bodies at Small Angles of Attack

Preliminary Remarks.

As mentioned in the text, Tulin (30) has previously presented a theory for steady planing of slender bodies at small angles of attack. It is unfortunate that this paper appears to have several errors. Nevertheless, it contains an interesting approach to the problem of steady planing and is adopted herein. The purpose of this section is twofold. It is intended that Tulin's original problem be formulate anew and extended to unsteady planing. The specific cases of uncambered delta wings at test and oscillating in heave are treated in detail.

The Coordinate System and Bernoulli Equation.

The coordinate system used for the solution of this problem is shown in Fig. A-1. It is fixed to the foil with its origin at the foil's apex. The x-axis passes through the mid-point of the trailing edge. The y-axis is normal to the plane containing the apex and the trailing edge and the z-axis completes the right handed set. The foil may have a small amount of camber but is assumed to be unyawed.

Neglecting the effect of gravity the equation of motion of the fluid in this frame of reference is given by:

$$\frac{D\vec{q}}{Dt} + \dot{\vec{v}}_b = -\frac{1}{\rho}\nabla p \qquad (A-1)$$

The term $\dot{\vec{v}}_b$, not usually encountered in steady problems, in required because Newton's Second Law must be applied in an inertial reference frame. This term represents the acceleration of the previously defined coordinate system with respect to an inertial one.

The velocity of any fluid particle with respect to the coordinate system of Fig. A-1 is $\vec{q}$. This velocity is expressed in terms of a potential such that the gradient of the potential yields the velocity.

$$\nabla \Phi = \vec{q} \tag{A-2}$$

Using this definition of Φ we can re-write equation A-1.

$$\nabla\left[\Phi_t + \frac{1}{2}(\nabla\Phi)^2 + \frac{p}{\rho} + \dot{v}_b(y\cos\alpha - x\sin\alpha)\right] = 0 \tag{A-3}$$

It should be noted that in the above equation motions normal to the free stream have been assumed. We can integrate equation A-3 to get

$$\Phi_t + \frac{1}{2}(\nabla\Phi)^2 + \frac{p}{\rho} + \dot{v}_b(y\cos\alpha - x\sin\alpha) = B(t). \tag{A-4}$$

The function B(t) is often called the Bernoulli constant since in steady problems it is a constant. Here it may be a function of time.

At infinity the velocity potential Φ is given by

$$\Phi_\infty = (U\cos\alpha + v_b\sin\alpha)x + (U\sin\alpha - v_b\cos\alpha)y \tag{A-5}$$

From this condition on the potential at infinity we get upon substitution into equation A-4 the value of B(t).

$$B(t) = \frac{p_\infty}{\rho} + \frac{1}{2}(U\cos\alpha + v_b\sin\alpha)^2 + \frac{1}{2}(U\sin\alpha - v_b\cos\alpha)^2 \tag{A-6}$$

By subtracting the potential at infinity we can define a new "perturbation" potential as in equation A-7.

$$\varphi = \Phi - \Phi_\infty \tag{A-7}$$

Re-writing equation A-4 in terms of the new potential φ we get the exact unsteady Bernoulli equation for this problem.

$$\varphi_t + \frac{1}{2}(\varphi_x + U\cos\alpha + v_b \sin\alpha)^2 + \frac{1}{2}(\varphi_y + U\sin\alpha - v_b\cos\alpha)^2$$

$$+ \frac{1}{2}(\varphi_z)^2 + \frac{p}{\rho} = \frac{1}{2}(U\cos\alpha + v_b\sin\alpha)^2 + \frac{1}{2}(U\sin\alpha - v_b\cos\alpha)^2 + \frac{p_\infty}{\rho} \qquad (A\text{-}8)$$

Laplace's Equation and the Boundary Conditions.

Although it has not been stated we are taking the fluid to be incompressible and inviscid. The condition of incompressibility simplifies the continuity equation and the irrotationality following from the inviscid assumption allows us to write the velocity as the gradient of a scalar potential. The equation then that the velocity potential must satisfy is the well known Laplace's equation A-9.

$$\nabla\Phi(x, y, z; t) = 0 \qquad (A\text{-}9)$$

It is easily shown that the perturbation potential also satisfies the same equation.

The boundary conditions on the perturbation potential will now be constructed. From its definition the perturbation potential is seen to vanish at infinity. On the foil we have the condition that the flow must be tangent to the boundary, which gives:

$$\Phi_y/\Phi_x = y_0' \qquad (A\text{-}10)$$

where $y_0(x)$ is the camber function and the prime denotes differentiation with respect to its spatial argument. Equation A-10 can be re-written as shown below

$$\Phi_y = \Phi_x y_0'$$

$$= (\varphi_x + U\cos\alpha + v_b\sin\alpha)y_0' \qquad (A\text{-}11)$$

This boundary condition on the foil is exact. The boundary condtions on the free surface require some approximations. They will be discussed in the next section.

Approximations.

From this point on we will assume that we are treating a "slender" body. What we mean by slender will become clear as the approximations are made. If we can assume as a result of this slenderness that $\varphi_{xx} << \varphi_{yy}, \varphi_{zz}$, it can then be neglected in Laplace's equation and x becomes a parameter entering the problem only through the boundary conditions and the potential is not affected by conditions upstream. Laplace's equation can now be written as

$$\nabla^2 \varphi(y, z; x, t) = 0. \qquad \text{(A-12)}$$

The problem has been reduced to a two dimensional boundary value problem in the so-called "cross-flow" plane.

We can also simplify the boundary condtion on the foil under the assumptions:

1) $\alpha << 1$ so that $\sin\alpha \doteq \alpha$ and $\cos\alpha \doteq 1$

2) $\varphi_x << U$ and

3) $\alpha v_b << U$.

Equation A-11 then becomes

$$\Phi_y \doteq \varphi_y + U\alpha - v_b \doteq U y_0'$$

or we can re-write this as

$$\varphi_y \doteq v_b + U y_0' - U\alpha. \qquad \text{(A-13)}$$

We have still to satisfy boundary conditions on the free surface. The nature of the problem dictates that we should have free stream

pressure everywhere on the free surface. The position of the free surface, not known a priori, will be taken to lie along the z-axis. In the actual case, sketched in Fig. 8, the free surface boundary is at $y = \alpha x$ at infinite distances from the foil and acquires a complicated shape near the foil. The approximation that the boundary conditions can be applied to the z-axis is necessary to keep the problem tractable. Figure 7 presents a photograph of a 30° apex angle delta wing planing at a small angle of attack. The spray can be seen. Because of the difficulty of determining the shape of the spray and the flow in the spray region, the spray will be represented as a singularity. The separation of the tips of the spray depends on the static height of the apex above the free surface, a slight amount of which will exist in any real situation.

As is shown in Fig. A-2, spray singularity is taken at $z = b_1$ (i.e., $\zeta = b$). Outside of this point the flow is assumed to be undisturbed or rather that $\varphi_z = 0$ for $|z| > b_1$ and since $\varphi = 0$ at infinity, $\varphi = 0$ for $|z| > b_i$ also.

In the region between the leading edge, $z = a(x)$ and $z = b_1$ we must determine a velocity boundary condition which at least approximates the pressure condition. This will be our next concern.

Let us define a new velocity potential in terms of coordinates normalized on the local semi-span, $a(x)$, since the flow will be approximately conical.

$$\varphi(y, z; x, t) = a(x) f(\eta, \zeta; t) \tag{A-14}$$

The coordinates are given by:

$$\eta = \frac{y}{a} \quad \text{and} \quad \zeta = \frac{z}{a}. \tag{A-15}$$

The derivatives of φ expressed in terms of f and appropriate coordinates are given below.

$$\begin{aligned} \varphi_x &= a_x(f-\eta f_\eta - \xi f_\xi) \\ \varphi_y &= f_\eta \\ \varphi_z &= f_\xi \\ \varphi_t &= a(x) f_t \end{aligned} \tag{A-16}$$

On the foil and in the region near the leading edge the pressure equation becomes

$$\frac{p-p_\infty}{\rho} \doteq -U\varphi_x - \frac{1}{2}\left(Uy_0'\right)^2 - \frac{1}{2}\left(\varphi_z\right)^2 + \frac{1}{2}\left(U\alpha - v_b\right)^2 - \varphi_t \tag{A-17}$$

where the $(\varphi_x)^2$ term has been neglected along with the assumptions following from the smallness of α. Replacing derivatives of φ by the appropriate functions of f and setting $p = p_\infty$ we get that at the free surface near the leading edge the following relation holds.

$$-2Ua_x(f-\xi f_\xi) - \left(Uy_0'\right)^2 - \left(f_\xi\right)^2 + \left(U\alpha - v_b\right)^2 - 2a(x)f_t = 0 \tag{A-18}$$

We will now estimate the value of each term in this equation so that some of them can be dispensed with. Near the leading edge $\xi \doteq 1$. Taking the distance from the leading edge to b to be ϵ and assuming f_ξ is approximately constant in that region we get that $f(1) \doteq -\epsilon f_\xi(1)$ near the leading edge. Taking $Ua_x \sim o(1)$, $Uy_0' \sim o(\delta)$, $U\alpha \sim o(\delta)$ and $v_b \sim o(\delta)$ where $\delta << 1$ we re-write equation (40) where the order of each term is noted.

$$\begin{matrix} 1+\delta^2 & \delta^2 & 1 & \delta^2 & k\delta^2 \end{matrix}$$

$$0 = 2Ua_x(1+\epsilon)f_\xi - \left(Uy_0'\right)^2 - \left(f_\xi\right)^2 + \left(U\alpha - v_b\right)^2 + 2a(x)f_t \tag{A-19}$$

The reduced frequency has been denoted by k. The order of the last term

in the above equation has not been shown yet. It will be shown later when ϵ is calculated. Since we will seek a quasi-steady solution of this problem we can reasonably neglect this term until a time when the proper restrictions on its importance can be shown. Keeping only terms of o(1) equation A-19 yields the following condition.

$$f_\xi = 2Ua_x \mathrm{Sgn}(\xi) \qquad \text{for} \quad 1 \le |\xi| < b \tag{A-20}$$

Conditions on f have now been specified along the entire ξ-axis. They are shown on Fig. A-2.

The Solution of the Boundary Value Problem.

The boundary value problem is, except for the unsteady parts, identical with Tulin's. The method of solution proposed by him and indeed part of his solution are used more-or-less directly.

The specified boundary conditions may be satisfied by a distribution of vorticity of strength $\gamma(\xi, t)$ along the ξ-axis between $-b(x,t)$ and $+b(x,t)$.

$$f_\eta(\xi) = \frac{1}{2\pi} \int_{-b}^{+b} \frac{\gamma(\zeta, t)}{(\xi - \zeta)} d\zeta \tag{A-21}$$

We can also re-write equation A-21 below since $\gamma(\xi, t) = 2f_\xi(-0, \xi; t)$.

$$\pi f_\eta(\xi) = \int_{-b}^{-1} \frac{f_\xi(\zeta)}{(\xi - \zeta)} d\zeta + \int_{-1}^{1} \frac{f_\xi(\zeta)}{(\xi - \zeta)} d\zeta + \int_{1}^{b} \frac{f_\xi(\zeta)}{(\xi - \zeta)} d\zeta \tag{A-22}$$

We can apply the known conditions on f_η and f_ξ, namely

$$f_\eta(\xi) = v_b + Uy_0' - U\alpha = v \qquad \text{for} \quad |\xi| \le 1$$

$$f_\xi(\xi) = 2Ua_x \mathrm{Sgn}(\xi) \qquad \text{for } 1 < |\xi| < b.$$

Equation A-22 then becomes the following where the only unknown is f_ξ for $|\xi| < 1$.

$$\pi v = -2Ua_x \int_{-b}^{-1} \frac{d\zeta}{(\xi-\zeta)} + 2Ua_x \int_{1}^{b} \frac{d\zeta}{(\xi-\zeta)} + \int_{-1}^{1} \frac{f_\xi(\zeta)}{(\xi-\zeta)} d\zeta \qquad \text{(A-23)}$$

Re-writing this in the form of the conventional airfoil equation we have the following:

$$\int_{-1}^{1} \frac{f_\xi(\zeta)}{(\xi-\zeta)} d\zeta = \left[\pi v - 2Ua_x \int_{1}^{b} \frac{d\zeta}{(\xi-\zeta)} + 2Ua_x \int_{-b}^{-1} \frac{d\zeta}{(\xi-\zeta)} \right] \quad \text{for } |\xi|<1$$

The formal solution of this equation can be found in Tricomi (32) and is taken from Tulin's work in the form given below.

$$\frac{f_\xi(\xi)}{U} = -\frac{1}{\pi^2\sqrt{1-\xi^2}} \left\{ \int_{-1}^{1} \frac{\sqrt{1-\zeta^2}}{(\xi-\zeta)} \left[\pi \frac{v}{U} - 2a_x \int_{1}^{b} \frac{d\tau}{(\zeta-\tau)} + 2a_x \int_{-1}^{1} \frac{d\tau}{(\zeta-\tau)} \right] d\xi \right\} \qquad \text{(A-24)}$$

The vortex sheet limit b is determined later to make $f_\xi(1)$ bounded.

If we combine integrations equation A-24 becomes

$$\frac{f_\xi(\xi)}{U} = -\frac{1}{\pi^2\sqrt{1-\xi^2}} \left\{ \pi^2 \frac{v}{U} \xi - 2a_x \int_{1}^{b} d\tau \int_{-1}^{1} \frac{\sqrt{1-\zeta^2}}{(\xi-\zeta)(\zeta-\tau)} d\zeta \right.$$
$$\left. + 2a_x \int_{-b}^{-1} d\tau \int_{-1}^{1} \frac{\sqrt{1-\zeta^2}}{(\xi-\zeta)(\zeta-\tau)} d\zeta \right\} . \qquad \text{(A-25)}$$

Using the following identities:

$$\frac{1}{(\xi-\zeta)(\zeta-\tau)} = \frac{1}{(\xi-\tau)} \left[\frac{1}{(\xi-\zeta)} + \frac{1}{(\zeta-\tau)} \right]$$

$$\int_{-1}^{1} \frac{\sqrt{1-\zeta^2}}{(\xi-\zeta)} d\zeta = \pi\xi \qquad \text{for } |\xi|<1$$

$$\int_{-1}^{1} \frac{\sqrt{1-\zeta^2}}{(\xi-\tau)} d\zeta = \begin{cases} \pi\left(-\tau - \sqrt{\tau^2-1}\right) & \tau < -1 \\ \pi\left(-\tau + \sqrt{\tau^2-1}\right) & \tau > 1 \end{cases}$$

the following equations can be shown to be true:

$$\frac{f_\xi(\xi)}{U} = -\frac{1}{\pi^2\sqrt{1-\xi^2}}\left\{\pi^2\frac{\nu}{U}\xi - \pi 2a_x\int_1^b \frac{\left[\xi-\tau+\sqrt{\tau^2-1}\right]}{(\xi-\tau)}d\tau \right.$$

$$\left. + \pi 2a_x\int_{-b}^{-1}\frac{\left[\xi-\tau-\sqrt{\tau^2-1}\right]}{(\xi-\tau)}d\tau\right\} \qquad \text{(A-26)}$$

$$\frac{f_\xi(\xi)}{U} = -\frac{1}{\sqrt{1-\xi^2}}\left\{\frac{\nu}{U}\xi + \frac{4}{\pi}a_x\xi\int_1^b\frac{\sqrt{\tau^2-1}}{(\tau^2-\xi^2)}\,d\tau\right\} \qquad \text{(A-27)}$$

With the substitution $\sqrt{1-\xi^2}\tan\theta = \sqrt{\tau^2-1}$ it can be shown for $b^2 \doteq 1$ (i.e., $\epsilon << 1$) that the integral in equation A-27 can be evaluated approximately.

$$\frac{f_\xi(\xi)}{U} \doteq -\frac{1}{\sqrt{1-\xi^2}}\left\{\frac{\nu}{U}\xi + \frac{4}{\pi}a_x\xi\left(\sqrt{b^2-1} - \sqrt{1-\xi^2}\tan^{-1}\sqrt{\frac{b^2-1}{1-\xi^2}}\right)\right\} \quad |\xi|<1 \qquad \text{(A-28)}$$

To keep $f_\xi(1)$ bounded b must have a particular value; namely,

$$\frac{\nu}{U} + \frac{4}{\pi}a_x\sqrt{b^2-1} = 0 \qquad \text{(A-29)}$$

If we write b as $1+\epsilon$ and take $\epsilon << 1$ we get the following relation for ϵ.

$$\epsilon = \frac{\pi^2}{32}\left(\frac{\nu}{Ua_x}\right)^2 \qquad \text{(A-30)}$$

$$= \frac{\pi^2}{32}\left(\frac{v_b + Uy_0' - U\alpha}{Ua_x}\right)^2 \qquad \text{(A-31)}$$

Previously we have assumed that $Ua_x \sim o(1)$, $v_b \sim o(\delta)$, $Uy_0' \sim o(\delta)$ where $\delta << 1$. From equation A-31 then we get directly that $\epsilon \sim o(\delta^2)$ which certainly justifies taking $b \doteq 1$ for the solution of equation A-27 and it also justifies neglecting ϵ compared to 1 in the first term of equation A-19.

It was stated without proof in equation A-19 that the last term of the equation was $o(k\delta^2)$. This will now be shown. The term is given below. It has been assumed f_ξ is constant in the region $1<|\xi|<b$ thereby neglecting any waves, therefore:

$$-2a(x)f_t = 2a(x)f_\xi \dot{\epsilon} \tag{A-32}$$

We can evaluate $\dot{\epsilon}$ from equation A-31.

$$\dot{\epsilon} = \frac{\pi^2}{16} \frac{\left(v_b + Uy_0' - U\alpha\right)}{\left(Ua_x\right)^2} \dot{v}_b$$

Assuming simple harmonic motion for v_b we get $|\dot{v}_b| = \omega|v_b|$ and $a(x)$ is limited to ca_x where c is the root chord of the foil. Substituting this into equation A-32 we get the following estimate for the order of that term.

$$-2a(x)f_t \sim 2(ca_x)(2Ua_x)\frac{\pi^2}{16}\frac{\left(v_b + Uy_0' - U\alpha\right)}{(Ua_x)^2}\omega v_b \sim o(k\delta^2) \tag{A-33}$$

We may conclude then that for $k \sim o(1)$ we are certainly justified in neglecting the contribution of this term to the boundary condition.

Substituting in the required value of b we get the final solution for f_ξ.

$$\frac{f_\xi(\xi)}{U} = \frac{4}{\pi} a_x \xi \tan^{-1} \frac{\left[-\frac{\pi}{4}\frac{\nu}{Ua_x}\right]}{\sqrt{1-\xi^2}} \qquad \text{for } |\xi|<1 \tag{A-34}$$

We can also express this in unreduced coordinates.

$$\frac{\varphi_z}{U} = \frac{4}{\pi} a_x \frac{z}{a} \tan^{-1} \frac{\left[-\frac{\pi}{4}\frac{\nu}{Ua_x}\right]}{\sqrt{1-(z/a)^2}} \qquad \text{for } |z|<a \tag{A-35}$$

This is the solution for φ_z as given by Tulin.

The Calculation of Forces.

The normal force on each incremental section will be found by integrating the pressure across the span.

$$\frac{dN}{dx} = \int_{-a}^{a} \left[p(0, z; x, t) - p_{\infty}\right] dz \qquad \text{(A-36)}$$

Using equation A-17 this can be re-written as shown below.

$$\frac{dN}{dx} = -\rho \int_{-a}^{a} \left[U\varphi_x + \frac{1}{2}(\varphi_z)^2 + \varphi_t + \frac{1}{2}\left(Uy_0'\right)^2 - \frac{1}{2}(U\alpha - v_b)^2\right] dz \qquad \text{(A-37)}$$

The first term of the above integral is evaluated using the relation:

$$\varphi(0, z; x, t) = \int_{a(1+\epsilon)}^{z} \frac{\partial}{\partial \zeta} \varphi(0, \zeta; x, t) d\zeta$$

$$= -2a\epsilon U a_x + \int_{a}^{z} \varphi_{\zeta}(0, \zeta; x, t) d\zeta. \qquad \text{(A-38)}$$

And by an application of Leibnitz' rule we get

$$\int_{-a}^{a} \varphi_x(0, z; x, t) dz = \frac{\partial}{\partial x} \int_{-a}^{a} \varphi(0, z; x, t) dz + 4a\epsilon U a_x^2. \qquad \text{(A-39)}$$

To use this we will need to integrate φ over the span.

$$\int_{-a}^{a} \varphi(0, z; x, t) dz = -4a^2 \epsilon U a_x - 2\int_{0}^{a} dz \int_{z}^{a} \varphi_{\zeta}(0, \zeta; x, t) d\zeta$$

$$= -4a^2 \epsilon U a_x - 2\int_{0}^{a} \varphi_z(0, z; x, t) dz \int_{0}^{z} d\zeta$$

$$= -4a^2 \epsilon U a_x - 2\int_{0}^{a} z\varphi_z(0, z; x, t) dz \qquad \text{(A-40)}$$

Now substituting equation A-40 into equation A-41 we get

$$-\rho\int_{-a}^{a} U\varphi_x dz = -\rho U\left\{\frac{\partial}{\partial x}\left[-4a^2\epsilon U a_x - 2\int_0^a z\varphi_z(0,z;x,t)dz\right] + 4a\epsilon U a_x^2\right\}$$

$$= \rho U^2 4a\frac{\partial}{\partial x}(a\epsilon a_x) + 2\rho U\frac{\partial}{\partial x}\int_0^a z\varphi_z(0,z;x,t)dz \qquad \text{(A-41)}$$

The remaining integral can be evaluated by reduction to known form. The solution given in reference (30) is repeated here.

$$\int_0^a z\varphi_z(0,z;x,t)dz = \frac{4U}{\pi}\frac{a_x}{a}\int_0^a z^2\tan^{-1}\frac{\left[-\frac{\pi}{4}\frac{\nu}{Ua_x}\right]}{\sqrt{1-(z/a)^2}}dz \qquad \text{(A-42)}$$

Let us substitute $k = k(x,t) = -\frac{\pi}{4}\frac{\nu}{Ua_x}$ and $\tau = \frac{z}{a}$. Equation A-42 is then equal to

$$= \frac{4U}{\pi}a^2 a_x\int_0^1 \tau^2\tan^{-1}\frac{k}{\sqrt{1-\tau^2}}d\tau. \qquad \text{(A-43)}$$

The integral from zero to one is then solved where the last step is from reference (33), p. 246.

$$\int_0^1 \tau^2\tan^{-1}\frac{k}{\sqrt{1-\tau^2}}d\tau = \int_0^k dk\int_0^1 \frac{\tau^2\sqrt{1-\tau^2}}{[(1+k^2)-\tau^2]}d\tau$$

$$= \frac{1}{2}\int_0^k dk\int_{-1/2}^{1/2}\frac{\sqrt{(\tau+1/2)(\tau-1/2)}}{[(1/2+k^2)-\tau]} \qquad \text{(A-44)}$$

$$= \frac{\pi}{2}\int_0^k\left[\frac{1}{2}+\frac{k^2}{2}-k\sqrt{1+k^2}\right] \qquad \text{(A-45)}$$

This can easily be integrated to give the following approximation.

$$\int_0^1 \tau^2 \tan^{-1}\frac{k}{\sqrt{1-\tau^2}}\,d\tau = \frac{\pi}{4}(k-k^2)+o(k^3) \qquad \text{(A-46)}$$

Then to $o(k^2)$ we have

$$\int_0^a z\varphi_z(0,z;x,t)\,dz = -\left(\frac{\pi}{4}\nu a^2 + \frac{\pi^2}{16}\frac{\nu^2 a^2}{Ua_x}\right) \qquad \text{(A-47)}$$

Gathering terms equation A-41 becomes finally

$$-\rho\int_{-a}^{a} U\varphi_x\,dz = \rho U^2 4a\frac{\partial}{\partial x}(a\epsilon a_x) - 2\rho U^2\frac{\partial}{\partial x}\left(\frac{\pi}{4}\frac{a^2\nu}{U}+\frac{\pi^2}{16}\frac{\nu^2 a^2}{U^2 a_x}\right)$$

$$= -\frac{\pi}{2}\rho U\frac{\partial}{\partial x}(a^2\nu) - \frac{\pi^2}{8}\rho a\nu^2 \qquad \text{(A-48)}$$

The next term in equation A-37 is evaluated approximately. Now,

$$\int_0^a \varphi_z^2\,dz = \left(\frac{4Ua_x}{\pi}\right)^2\int_0^a\left(\frac{z}{a}\right)^2\left[\tan^{-1}\frac{\left(-\frac{\pi}{4}Ua_x\right)}{\sqrt{1-\left(\frac{z}{a}\right)^2}}\right]^2 dz \qquad \text{(A-49)}$$

If we again let $k = -\frac{\pi}{4}\frac{\nu}{Ua_x}$ and let $p = \sqrt{1-(z/a)^2}$, equation A-49 becomes

$$= \left(\frac{4Ua_x}{\pi}\right)^2 a\int_0^1 p\sqrt{1-p^2}\left[\tan^{-1}\frac{k}{p}\right]^2 dp \qquad \text{(A-50)}$$

The inverse tangent can be expanded in the two regions as shown below.

$$\tan^{-1}\frac{k}{p} = \frac{\pi}{2} - \sum_{n=0}^{\infty}\frac{(-1)^n}{(2n+1)}\left(\frac{p}{k}\right)^{2n+1} \qquad \text{for } p<k$$

$$= \sum_{n=0}^{\infty}\frac{(-1)^n}{(2n+1)}\left(\frac{k}{p}\right)^{2n+1} \qquad \text{for } p>k$$

The integral can then be split into two parts.

$$\int_0^1 p\sqrt{1-p^2}\left[\tan^{-1}\frac{k}{p}\right]^2 dp = \int_0^k p\sqrt{1-p^2}\left[\frac{\pi}{2} - \sum_{n=0}^{\infty}\frac{(-1)^n}{2n+1}\left(\frac{p}{k}\right)^{2n+1}\right]^2 dp$$

$$+ \int_k^1 p\sqrt{1-p^2}\left[\sum_{n=0}^{\infty}\frac{(-1)^n}{2n+1}\left(\frac{k}{p}\right)^{2n+1}\right]^2 dp \qquad (A\text{-}51)$$

We will first treat the integral from zero to k. In this region $\sqrt{1-p^2}$ will be replaced by 1 since the next contribution is $o(k^2)$ compared to the part retained. Expanding this integral we get the following expression.

$$\int_0^k p\left[\frac{\pi}{2} - \sum_{n=0}^{\infty}\frac{(-1)^n}{2n+1}\left(\frac{p}{k}\right)^{2n+1}\right]^2 dp = \int_0^k \left[\frac{\pi^2}{4}p\right.$$

$$\left. - \pi\sum_{n=0}^{\infty}\frac{(-1)^n}{2n+1}\frac{p^{2n+2}}{k^{2n+1}} + \sum_{n=0}^{\infty}A_n\frac{p^{2n+3}}{k^{2n+2}}\right] dp \qquad (A\text{-}52)$$

The value of A_n is given by

$$A_n = (-1)^n \sum_{m=0}^{n}\frac{1}{(2m+1)(2n-2m+1)} \qquad (A\text{-}53)$$

Equation A-52 can now be easily integrated term by term.

$$= \left[\frac{\pi^2}{8} - \pi\sum_{n=0}^{\infty}\frac{(-1)^n}{(2n+1)(2n+3)} + \sum_{n=0}^{\infty}\frac{A_n}{2n+4}\right]k^2 \qquad (A\text{-}54)$$

The region from k to 1 is treated in a similar manner.

$$\int_k^1 p\sqrt{1-p^2}\left[\sum_{n=0}^{\infty}\frac{(-1)^n}{2n+1}\left(\frac{k}{p}\right)^{2n+1}\right]^2 dp = \int_k^1 p\sqrt{1-p^2}\sum_{n=0}^{\infty}A_n\left(\frac{k}{p}\right)^{2n+2} dp \qquad (A\text{-}55)$$

Interchanging integration and summation we get

$$= \sum_{n=0}^{\infty} A_n k^{2n+2} \int_k^1 \frac{\sqrt{1-p^2}}{p^{2n+1}}\, dp \tag{A-56}$$

For the case $n = 0$ we have

$$k^2 \int_k^1 \frac{\sqrt{1-p^2}}{p}\, dp = -k^2\sqrt{1-k^2} + k^2 \log \frac{1+\sqrt{1-k^2}}{k}$$

and for general $n > 0$ the leading term of the solution is

$$k^{2n+2} \int_k^1 \frac{\sqrt{1-p^2}}{p^{2n+2}}\, dp = \frac{k^2}{2n} + o(k^4)$$

Then to $o(k^2)$ we have

$$\int_k^1 p\sqrt{1-p^2}\left[\tan^{-1}\frac{k}{p}\right]^2 dp = -A_0 k^2 - A_0 k^2 \log k + k^2 \sum_{n=1}^{\infty} \frac{A_n}{2n} \tag{A-57}$$

The integral over the whole region from zero to one is then finally

$$\int_0^1 p\sqrt{1-p^2}\left[\tan^{-1}\frac{k}{p}\right]^2 dp = \left[\frac{\pi^2}{8} - 1 + \log 2 - \pi \sum_{n=0}^{\infty} \frac{(-1)^n}{(2n+1)(2n+3)}\right.$$

$$- \pi \sum_{n=0}^{\infty} \frac{(-1)^n}{(2n+1)(2n+3)} + \sum_{n=0}^{\infty} \sum_{m=0}^{n} \frac{(-1)^n}{(2n+4)(2m+1)(2n-2m+1)}$$

$$\left. + \frac{1}{2} \sum_{n=1}^{\infty} \sum_{m=0}^{n} \frac{(-1)^n}{n(2m+1)(2n-2m+1)} - \log k \right] k^2 + o(k^4) \tag{A-58}$$

The two double sums do not converge particularly rapidly so we set them up on a computer (an application it is eminently suited for). With an execution time of less than one second we are given the following result.

$$\int_0^1 p\sqrt{1-p^2}\left[\tan^{-1}\left(\frac{k}{p}\right)\right]^2 dp \doteq -\left[0.04+\log k\right]k^2 \qquad \text{(A-59)}$$

After substituting for k we have the solution for equation (49).

$$-\rho\int_0^a \varphi_z^2\, dz = \rho a\nu^2\left[0.04+\log\left(-\frac{\pi}{4}\,\frac{\nu}{Ua_x}\right)\right] \qquad \text{(A-60)}$$

The third term in equation (37) is evaluated as follows.

$$-\rho\int_{-a}^{a} \varphi_t dz = -\rho\frac{\partial}{\partial t}\int_{-a}^{a}\varphi\, dz \qquad \text{(A-61)}$$

This can be expressed using equations (40) and (47) in the following form.

$$-\rho\frac{\partial}{\partial t}\int_{-a}^{a}\varphi\, dz = -\rho\frac{\partial}{\partial t}\left[-4a^2Ua_x+\frac{\pi}{2}a^2\nu+\frac{\pi^2}{8}\,\frac{\nu^2a^2}{Ua_x}\right] = -\frac{\pi}{2}\rho a^2\dot{\nu} \qquad \text{(A-62)}$$

The other terms in equation (37), being constant across the span, are easily integrated. Equation (37) can then be written finally as

$$\frac{dN}{dx} = -\frac{\pi}{2}\rho U\frac{\partial}{\partial x}(a^2\nu) - \frac{\pi^2}{8}\rho a\nu^2 + \rho a\nu^2\left[0.04+\log\left(-\frac{\pi}{4}\,\frac{\nu}{Ua_x}\right)\right]$$

$$-\frac{\pi}{2}\rho a^2\dot{\nu} - \rho a(Uy_0')^2 + \rho a(U\alpha - v_b)^2 \qquad \text{(A-63)}$$

Specific Cases.

For the case of a stationary ($v_b = 0$), flat ($y_0' = 0$) delta wing of apex angle $\beta(a_x = \beta/2)$ equation (63) is

$$\frac{2}{\rho U^2}\,\frac{dN}{dx} = \frac{\pi}{2}\alpha\beta^2 x - \frac{\pi^2}{8}\alpha^2\beta x + \alpha^2\beta x\left[0.04+\log\frac{\pi}{2}-\log\frac{\beta}{\alpha}\right]+\alpha^2\beta x \qquad \text{(A-64)}$$

The normal force is obtained by integrating equation (64) from the apex to the trailing edge. The normal force is reduced to a coefficient by divising by the dynamic pressure and the foil planform area. The normal force coefficient is then given to be

$$C_N = \frac{\pi}{2}\beta\alpha + \left[0.26 - \log\frac{\beta}{\alpha}\right]\alpha^2 \tag{A-65}$$

The lift and drag coefficients can be obtained by projecting the normal force vector since there are no tangential forces from this theory. The normal force vector since there are no tangential forces from this theory. The normal force coefficient curve slope is given by

$$\frac{\partial C_N}{\partial \alpha} = \frac{\pi}{2}\beta + \left[1.52 - 2\log\frac{\beta}{\alpha}\right]\alpha \tag{A-66}$$

If we oscillate the hydrofoil such that

$$v_b = \tilde{v}\sin \omega t \tag{A-67}$$

the sectional lift given by equation (63) becomes

$$\frac{2}{\rho U^2}\frac{dN}{dx} = \frac{\pi}{2}\beta^2 x\left(\alpha - \frac{\tilde{v}}{U}\sin \omega t\right) - \frac{\pi^2}{8}\beta x\left(\frac{\tilde{v}}{U}\sin \omega t - \alpha\right)^2$$

$$+ \beta x\left(\frac{\tilde{v}}{U}\sin \omega t - \alpha\right)^2\left[0.04 + \log\left(-\frac{\pi}{2}\,\frac{\frac{\tilde{v}}{U}\sin \omega t - \alpha}{\beta}\right)\right]$$

$$+ \beta x\left(\frac{\tilde{v}}{U}\sin \omega t - \alpha\right)^2 - \frac{\pi}{4}\beta^2 x^2 \omega\,\frac{\tilde{v}}{U^2}\cos \omega t \tag{A-68}$$

If in the last term we write the reduced fequency as k, the time dependent normal force coefficient is given by

$$C_N(t) = \frac{\pi}{2}\beta\left(\alpha - \frac{\tilde{v}}{U}\sin \omega t\right) - \frac{\pi^2}{8}\left(\alpha - \frac{\tilde{v}}{U}\sin \omega t\right)^2$$

$$+ \left(\alpha - \frac{\tilde{v}}{U}\sin \omega t\right)^2\left[0.04 + \log\frac{\pi}{2} - \log\frac{\beta}{\alpha} + \log\left(1 - \frac{\tilde{v}}{U\alpha}\sin \omega t\right)\right]$$

$$+ \left(\alpha - \frac{\tilde{v}}{U}\sin \omega t\right)^2 - \frac{\pi}{3}\beta k\,\frac{\tilde{v}}{U}\cos \omega t\,. \tag{A-69}$$

We might note that previously we have restricted the size of $U\alpha$ and v_b compared to Ua_x. More specifically, in terms of delta wing

parameters, we have said that $(\alpha/\beta)^2 << 1$ and $(v_b/U\beta)^2 << 1$. We have not said anything about the ratio $(v_b/U\alpha)$. , Because of the time dependent argument of the log term in equation (69) it will prove useful to take $(v_b/U\alpha) < 1$ so that we can expand the argument about one. The first term is clearly the dominant one of frequency ω. Let us consider only that part of $C_N(t)$ which is changing at the angular frequency ω and normalize the unsteady force coefficient components by dividing by the apparent change in angle of attack which is

$$\bar{\alpha} = -\frac{v_b}{U}. \tag{A-70}$$

The unsteady coefficients then become

$$C_{N_{\bar{\alpha}_r}} = \frac{\pi}{2}\beta + 2\alpha\left[0.76 - \log\frac{\beta}{\alpha}\right]$$

and

$$C_{N_{\bar{\alpha}_i}} = \frac{\pi}{3}\beta k \tag{A-71}$$

The subscripts r and i denote the component in-phase with the apparent angle of attack and the quadrature component respectively.

Figure A-3 presents the theoretical value of $C_{N\bar{\alpha}_r}/\beta$ as a function of α/β. It should be noted that $C_{N_{\bar{\alpha}_r}}$ and $\frac{\partial C_N}{\partial \alpha}$ stationary have the same value. This is not entirely unexpected for a quasi-steady theory.

The Effect of Gravity.

Although the preceding theory is strictly only for no gravity - experiments, perforce, must be made in the presence of a gravity field. This, of course, enormously complicates the entire problem as is well known. For very slender bodies, however, it seems reasonable that

the cross-flow streamlines and hence velocities will not be affected to first order because of the smallness of the parameter ϵ and the ratio of α to β. If this is the case, the pressures over the wetted face of the foil under the action of gravity will be increased by the local hydrostatic pressure (except very near to the spray sheet). This leads to the conclusion that the steady lift force is increased merely by the weight of the fluid above the hydrofoil. Thus if the angle of attack is α and if this weight is expressed in coefficient form we have

$$\Delta C_L = \frac{2}{3} \frac{\sin 2\alpha}{F^2} \qquad \text{(A-72)}$$

where F is the Froude number based on chord. Interestingly, Maruo (Ref. 34) has arrived at the same result as the limiting case of a much more complete lifting surface theory. The graphs of Figs. 37-39 incorporate this added term given by Eq. A-72.

Remarks.

It is useful to recapitulate the differences in the assumed flow model and that observed in practice. Referring again to Fig. 8 which is a sketch of the "actual" cross-flow, the free surface lies above the foil, not in the plane of the foil. The spray extends over the foil but does not form a closed cavity. It should also be mentioned that the flow is not conical near the trailing edge. This effect is similar to the ventilated cases shown by Kiceniuk in Ref. (29). A slight lift loss over the aft portion of the foil results and this produces a pitch up moment compared to the theory.

The unsteadiness of the flow is represented in two alterations of the boundary conditions, one explicit, the other implicit. The explicit

change is the addition of the heaving velocity at the foil. The implicit change is in the spray position which is allowed to change with time. Th. unsteady behavior shows up in the Bernoulli equation but since the fluid is incompressible, time enters Laplace's equation only as a parameter. In this sense the present theory is only a quasi-steady slender body approximation because no previous dynamic history of the flow is permitted to occur in the constant pressure boundary condition.

The theory is limited because of the slender body assumption to values of $\beta << 1$. It is further limited by other assumptions, particularly the spray position, to values of $(\alpha/\beta)^2 << 1$. The model may have a small amount of camber but the heaving velocity must be small, i.e., $v_b < U\alpha$. These conditions severly restrict the present theory to a rather narrow range of conditions.

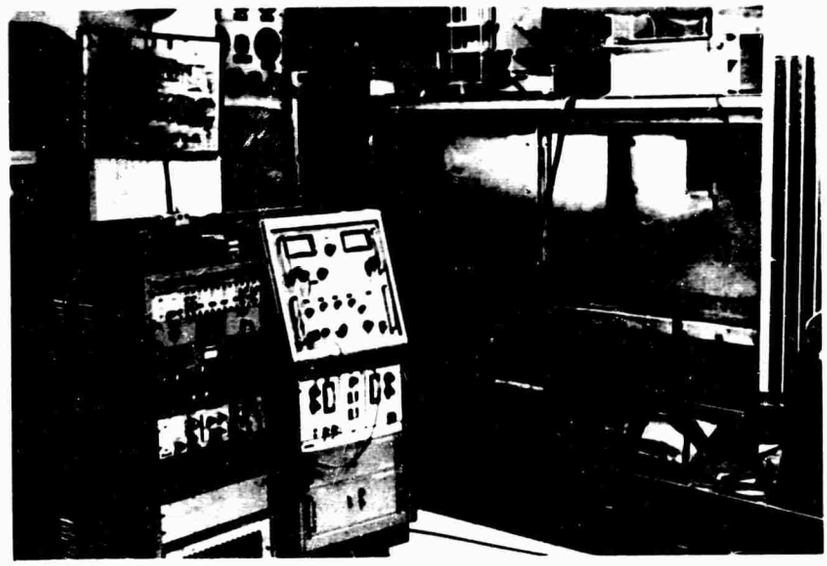

Fig. 1 View of tunnel working section, electronic apparatus and hydraulic oscillator mounted in the working section. There is no water in the working section.

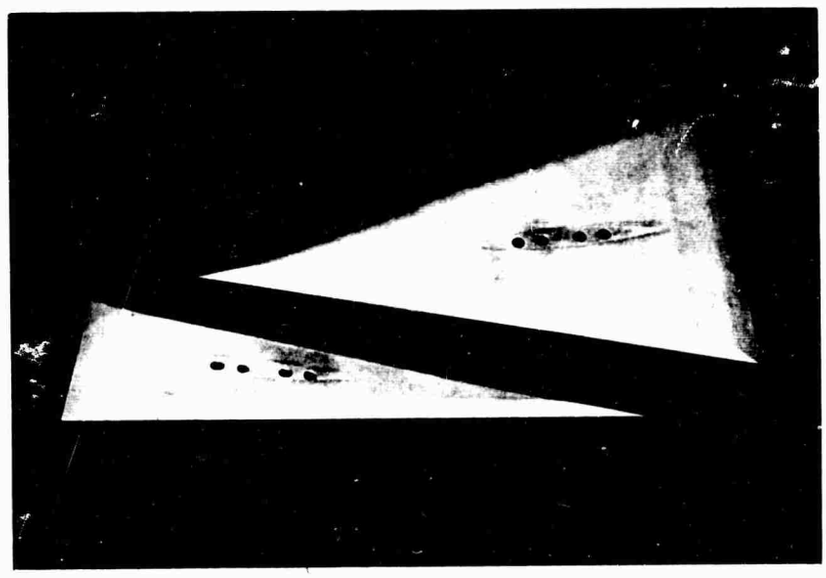

Fig. 3 Photograph of the 15 and 30 degree apex angle delta wing hydrofoil models.

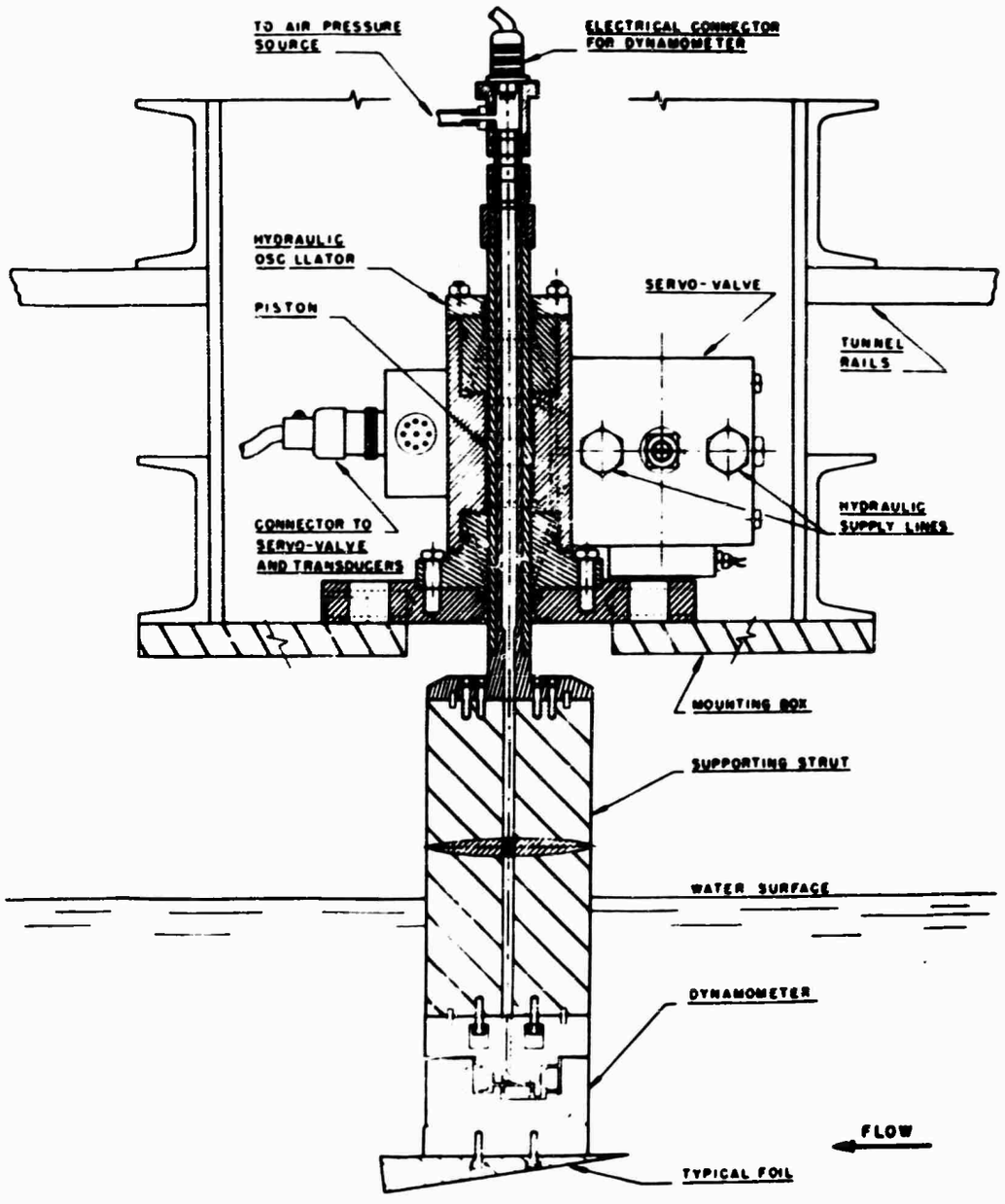

Fig. 2 Cross-section drawing of the hydraulic oscillator showing the tunnel mounting, balance (dynamometer) location and hydrofoil location.

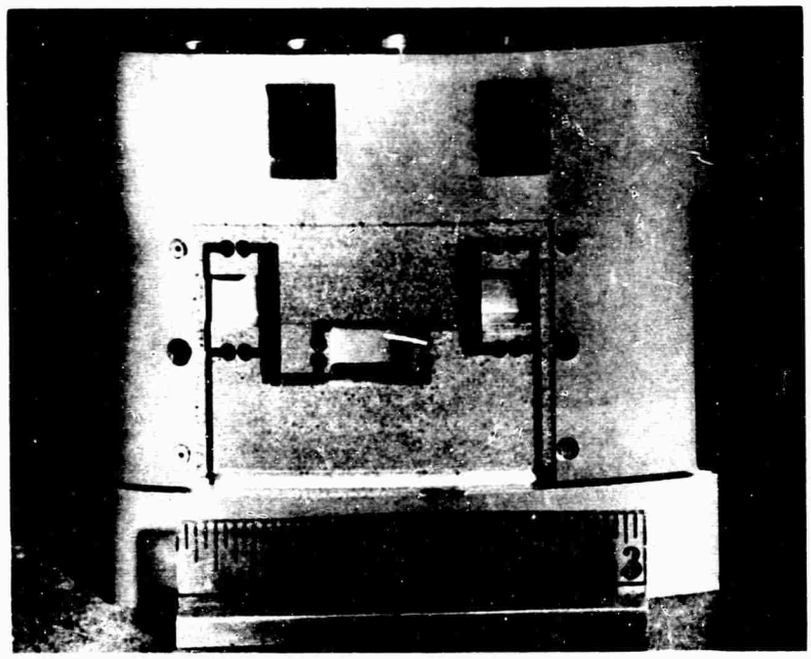

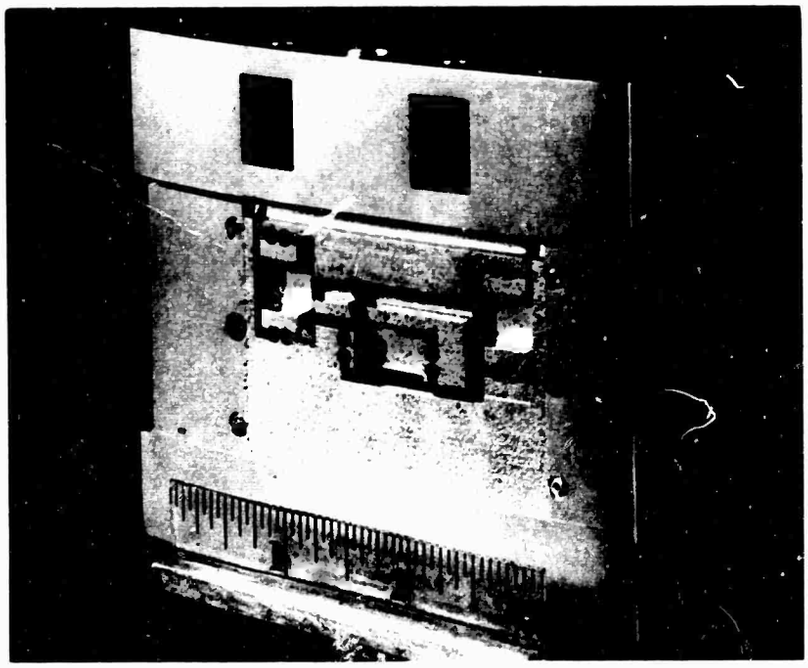

Fig. 4 The lift and pitching moment balance, seen from both sides, before affixing the strain gages.

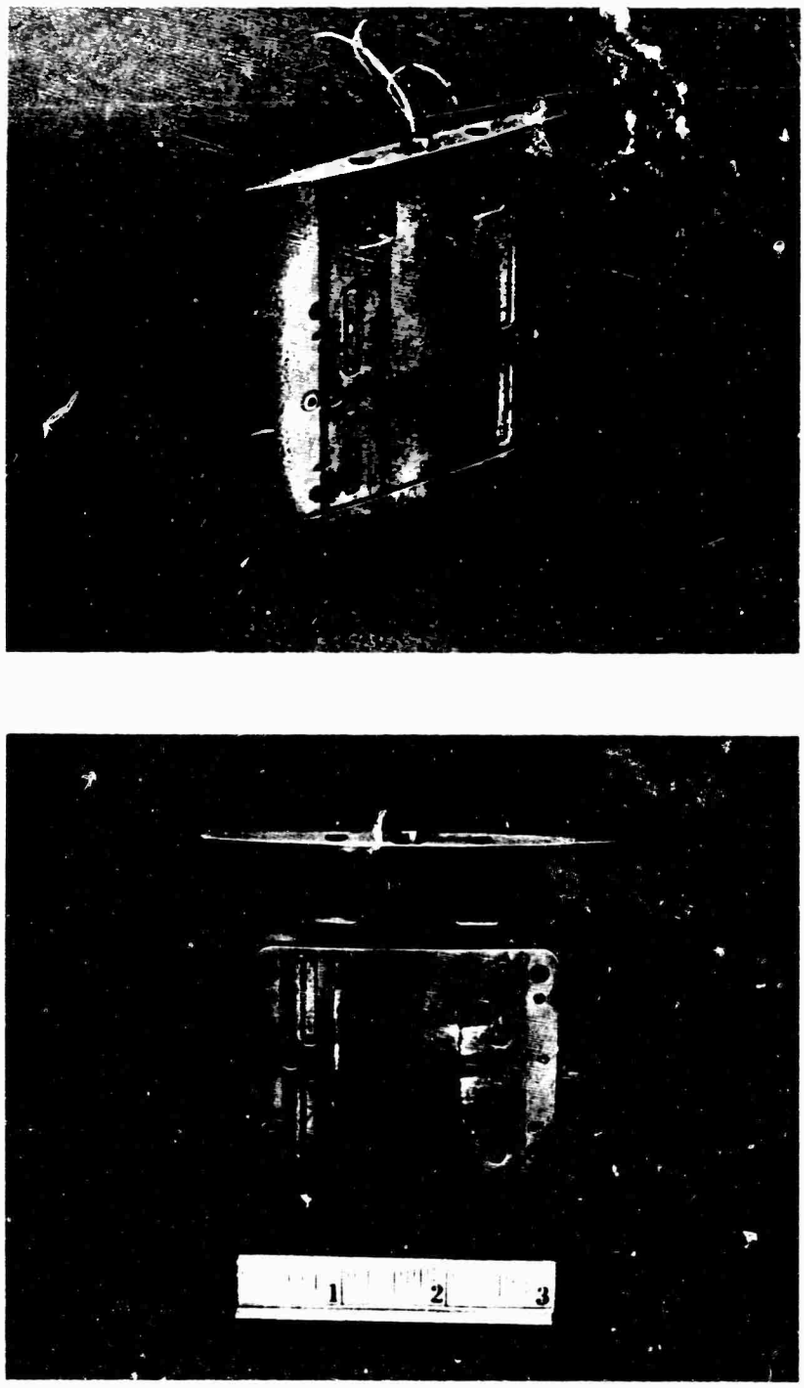

Fig. 5 The drag balance, seen from both sides, without waterproofing.

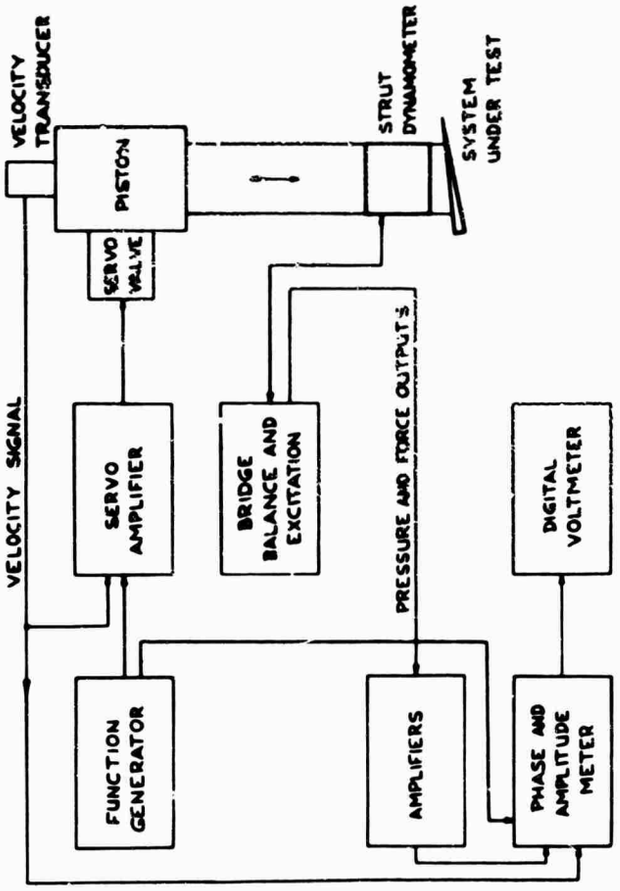

Fig. 6 Diagram of the electronic equipment for the hydraulic oscillator and data acquisition.

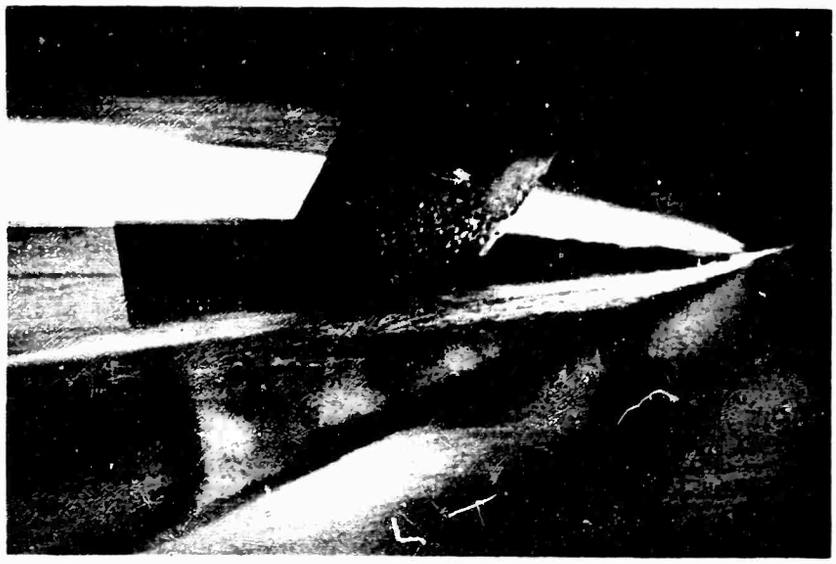

Fig. 7 Photograph of the 30° delta wing hydrofoil planing at a small angle of attack.

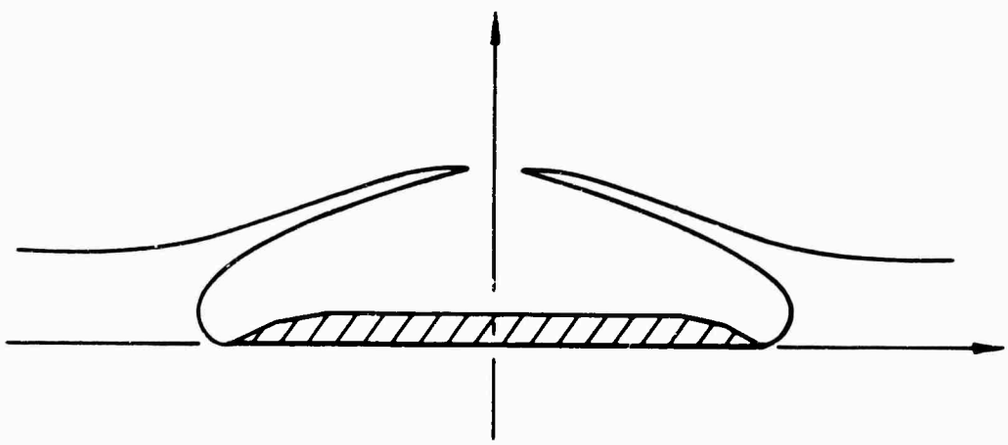

Fig. 8 Sketch of the actual cross flow of a planing delta wing at a small angle of attack.

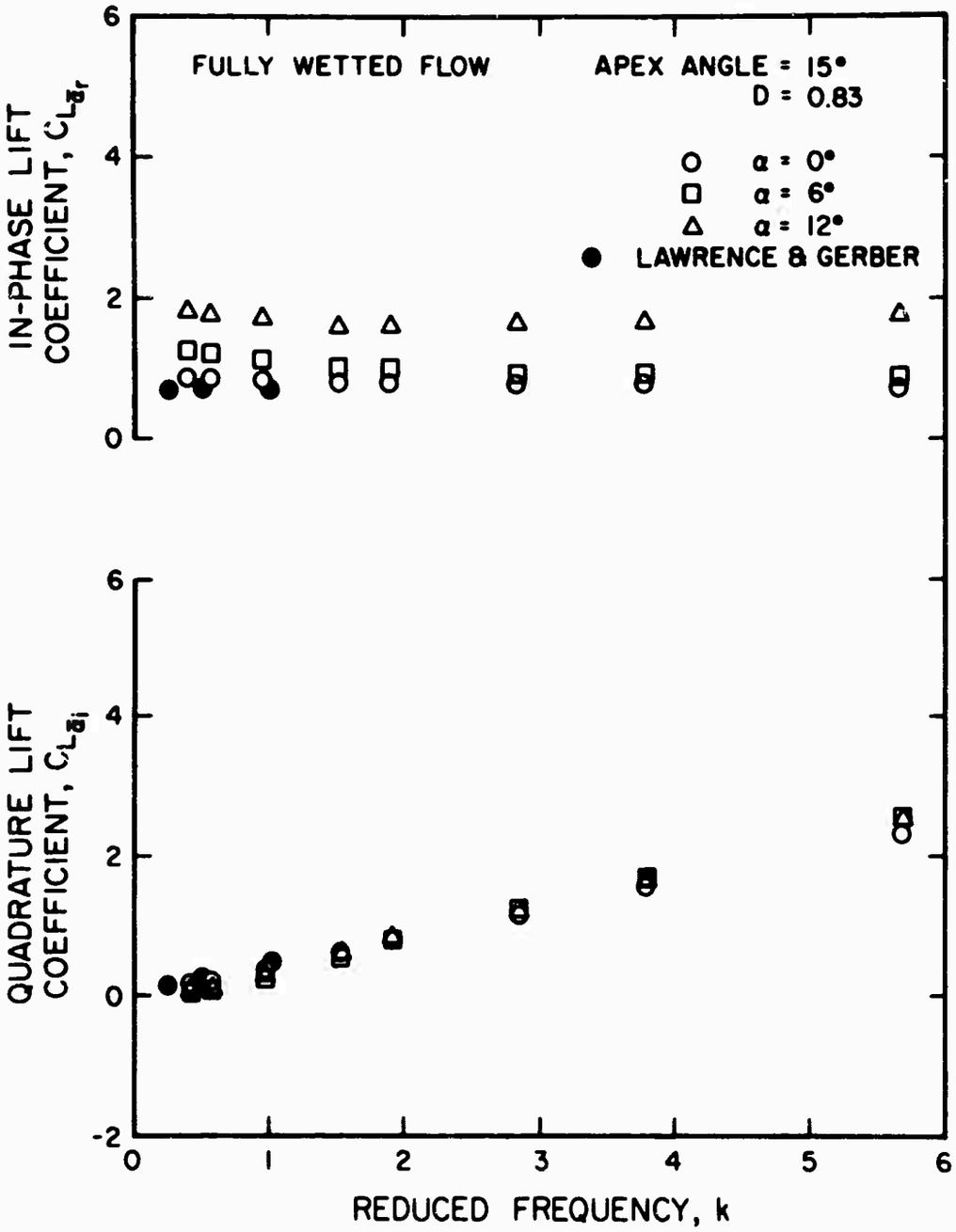

Fig. 9 Unsteady lift coefficients for a fully wetted delta wing with 0.83 chords submergence at various angles of attack.

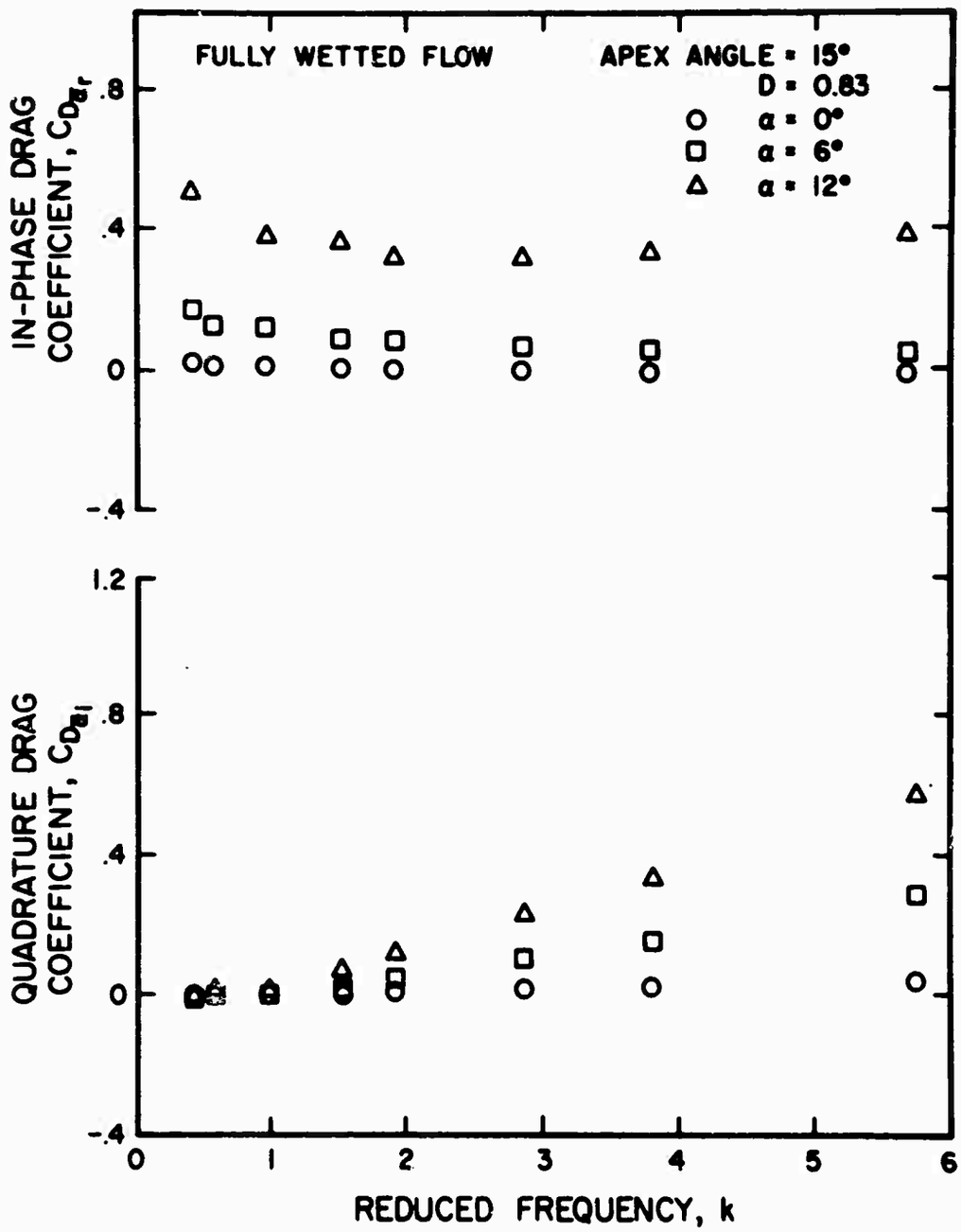

Fig. 10 Unsteady drag coefficients for a fully wetted delta wing with 0.83 chords submergence at various angles of attack.

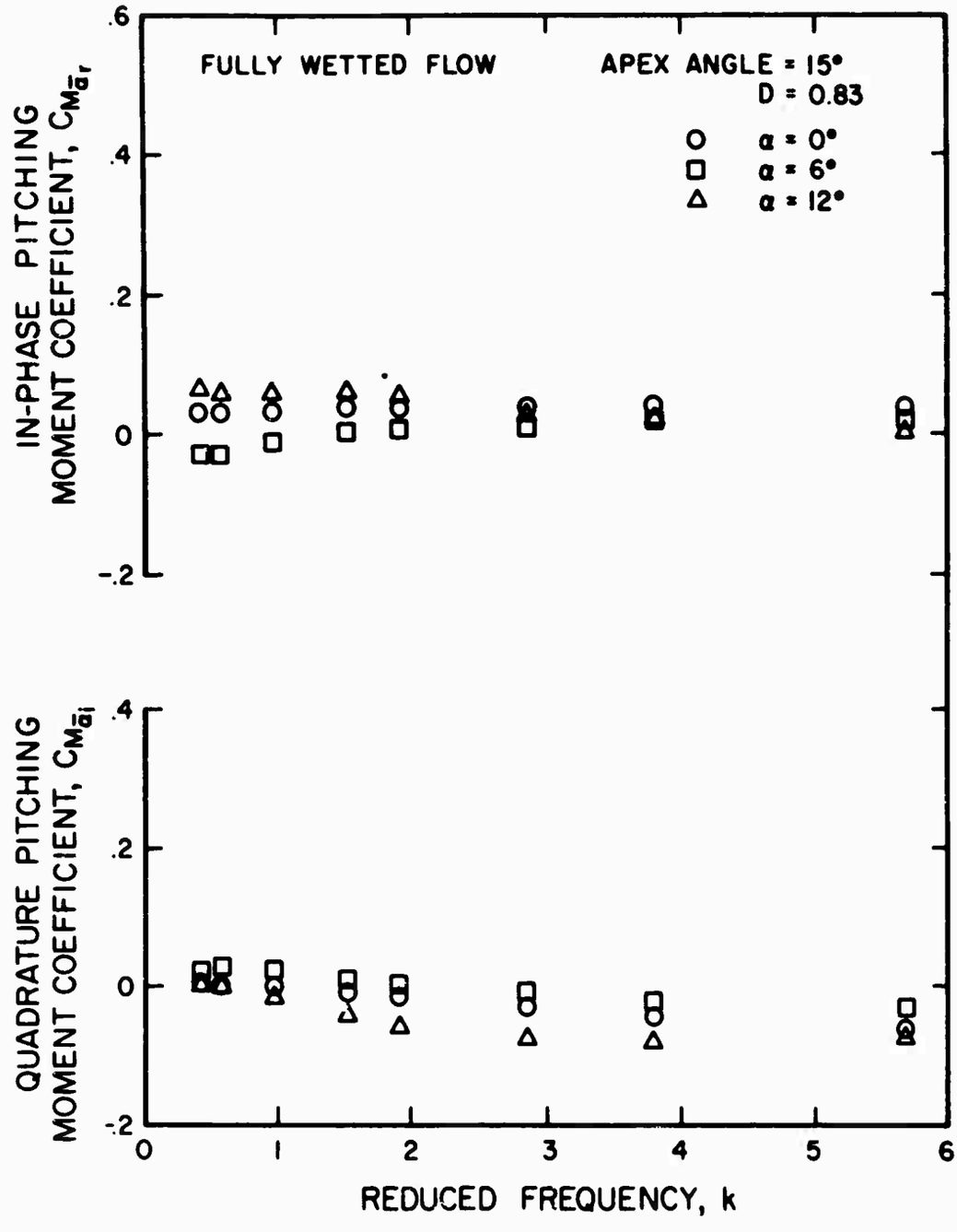

Fig. 11 Unsteady pitching moment coefficients for a fully wetted delta wing at 0.83 chords submergence at various angles of attack.

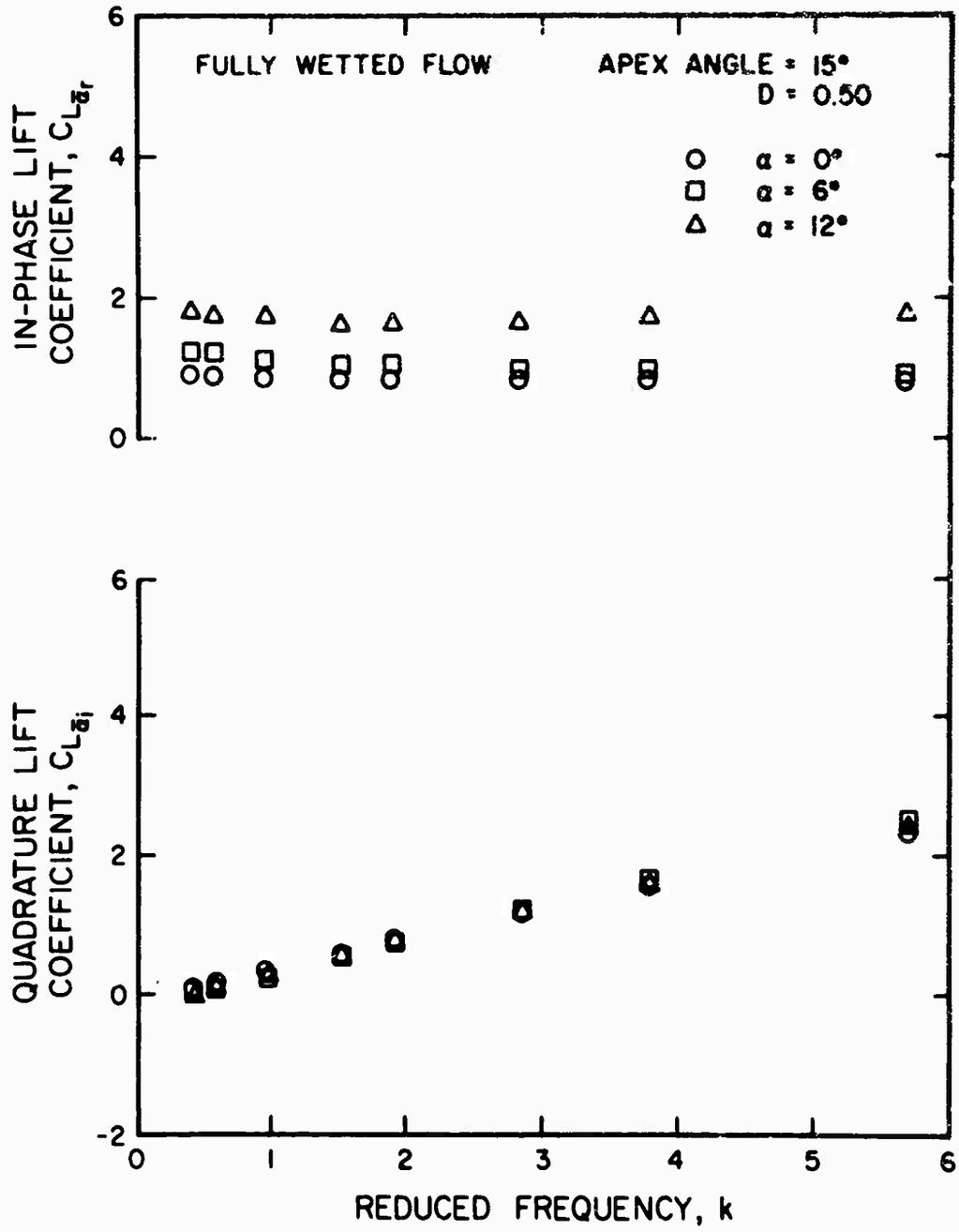

Fig. 12 Unsteady lift coefficients for a fully wetted delta wing with 0.50 chords submergence at various angles of attack.

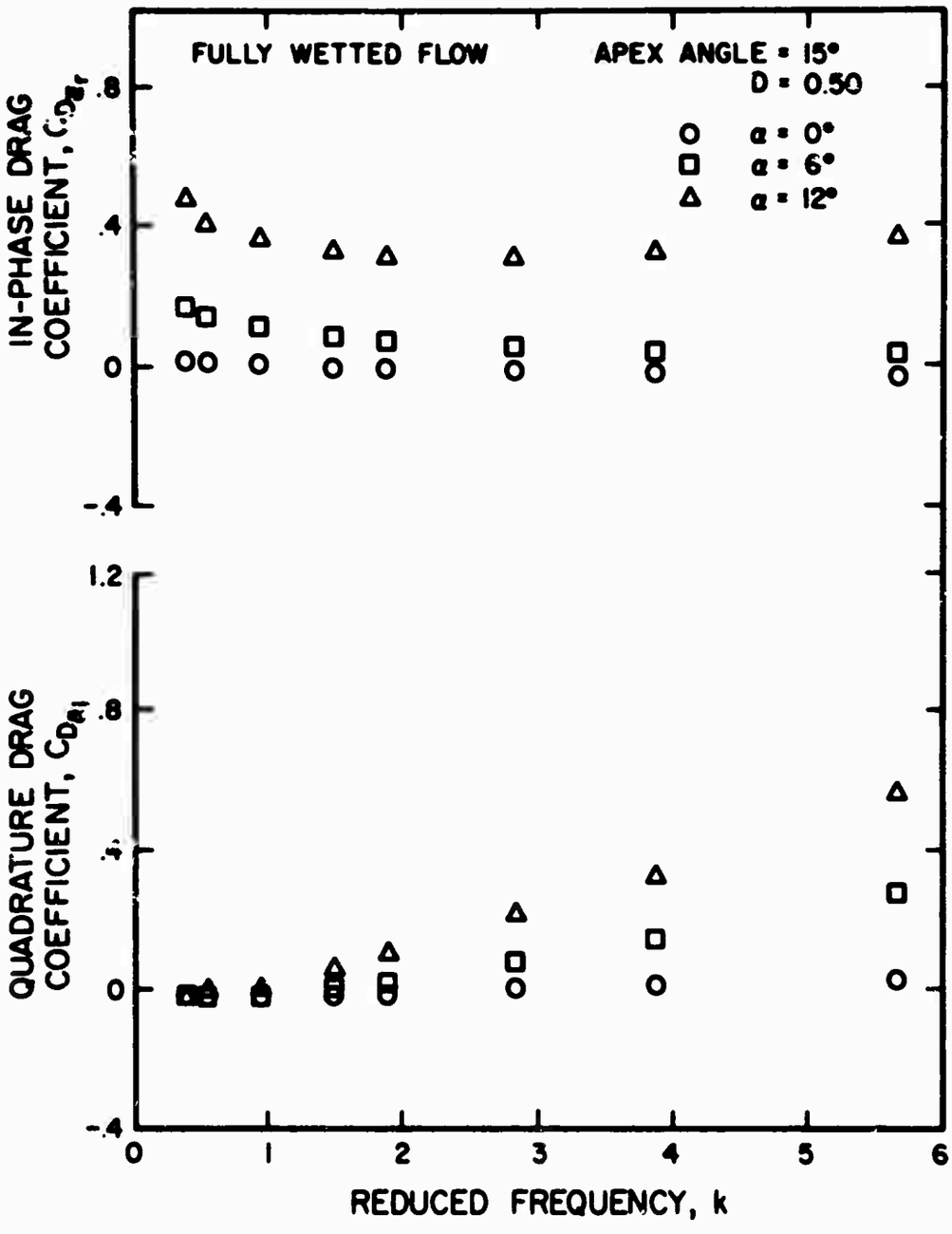

Fig. 13 Unsteady drag coefficients for a fully wetted delta wing with 0.50 chords submergence at various angles of attack.

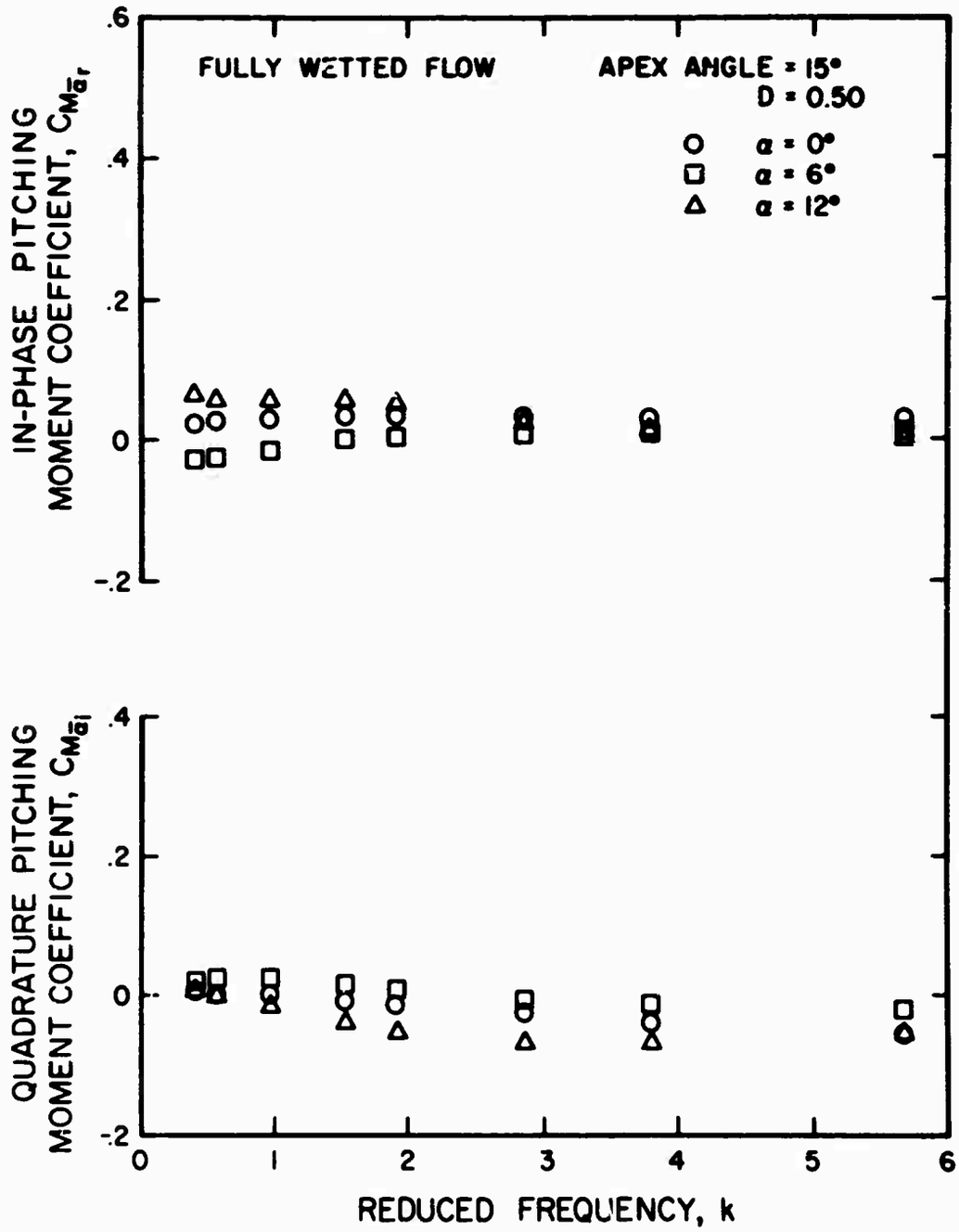

Fig. 14 Unsteady pitching moment coefficients for a fully wetted delta wing at 0.50 chords submergence at various angles of attack.

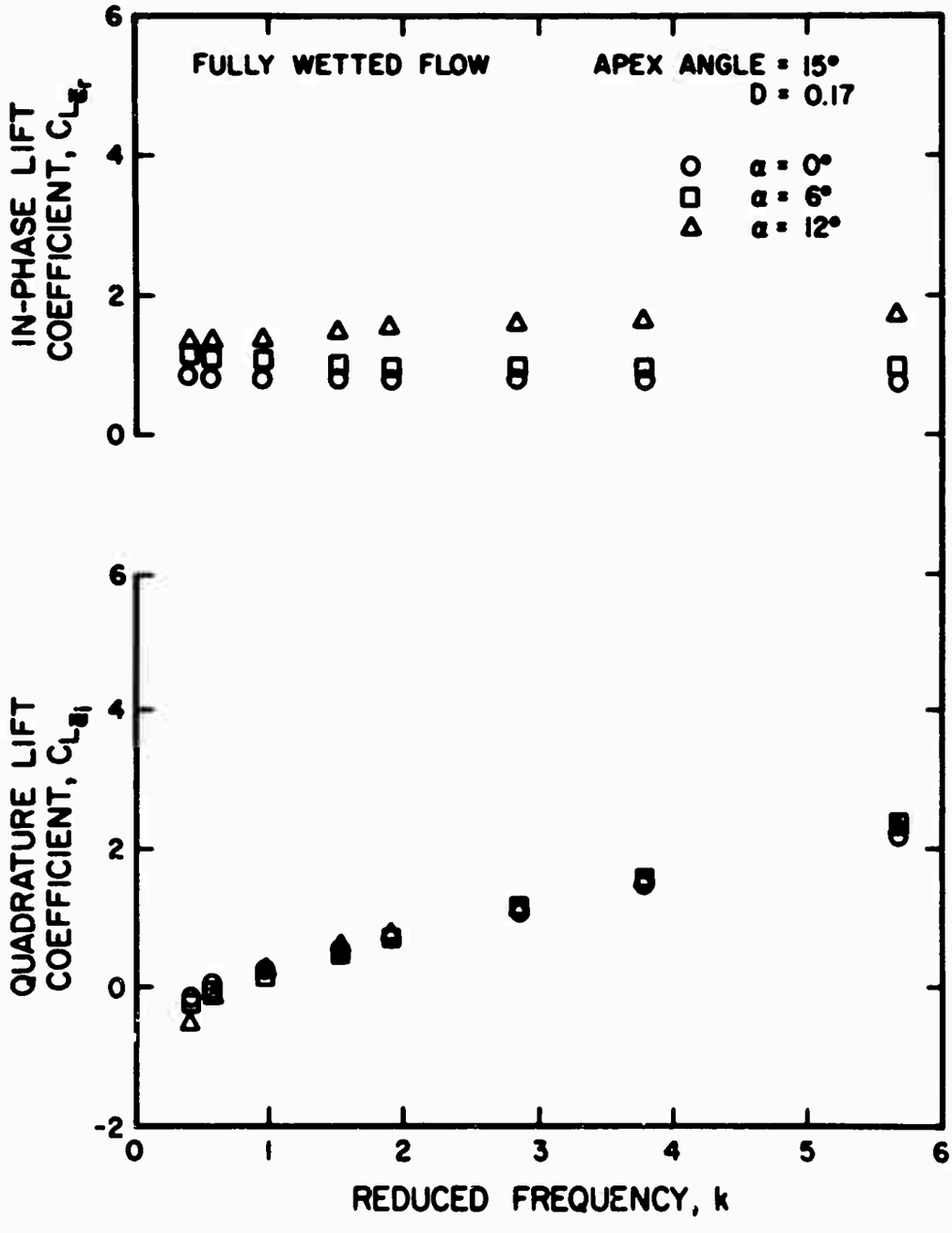

Fig. 15 Unsteady lift coefficients fo. a fully wetted delta wing with 0. 17 chords submergence at various angles of attack.

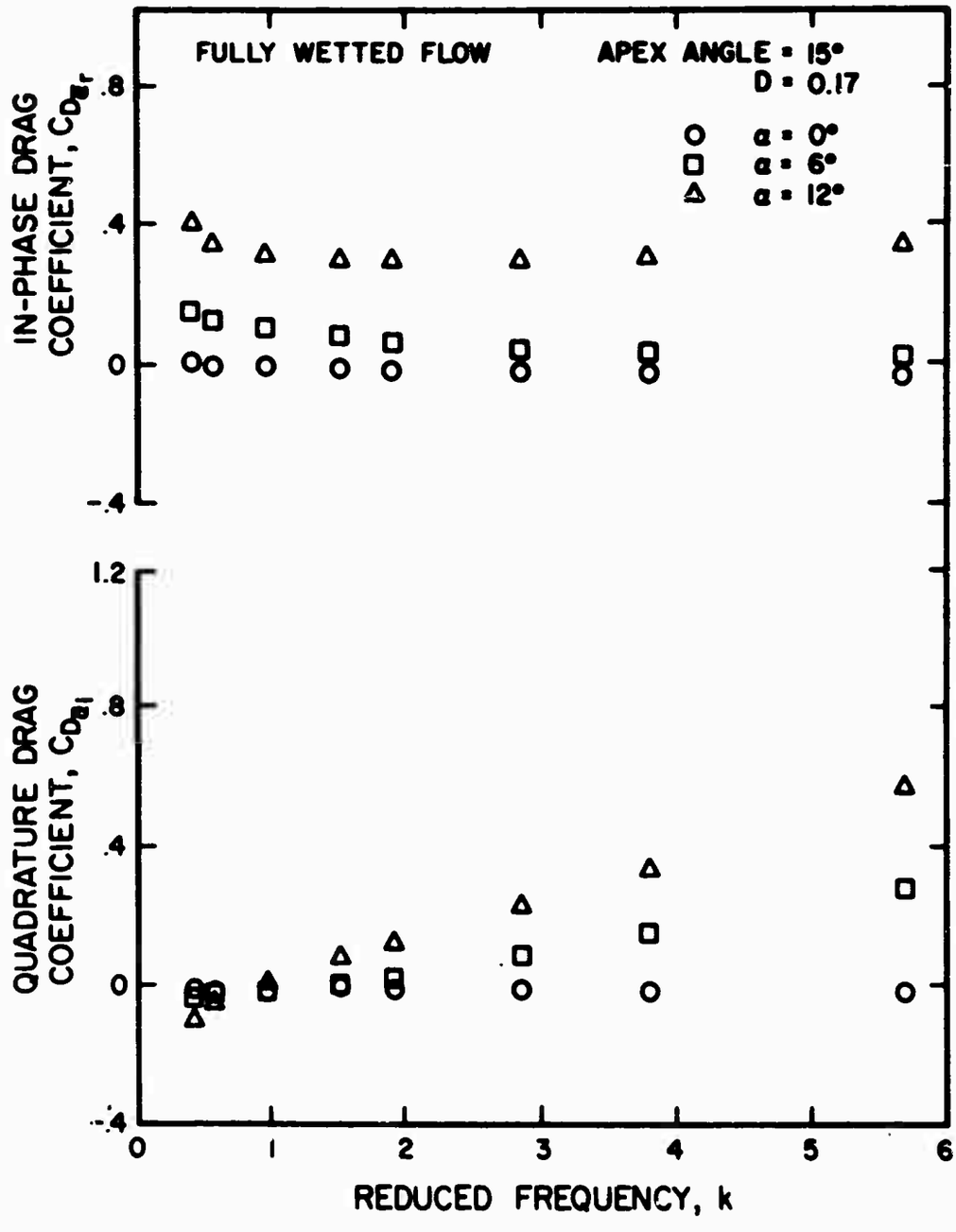

Fig. 16 Unsteady drag coefficients for a fully wetted delta wing with 0.17 chords submergence at various angles of attack.

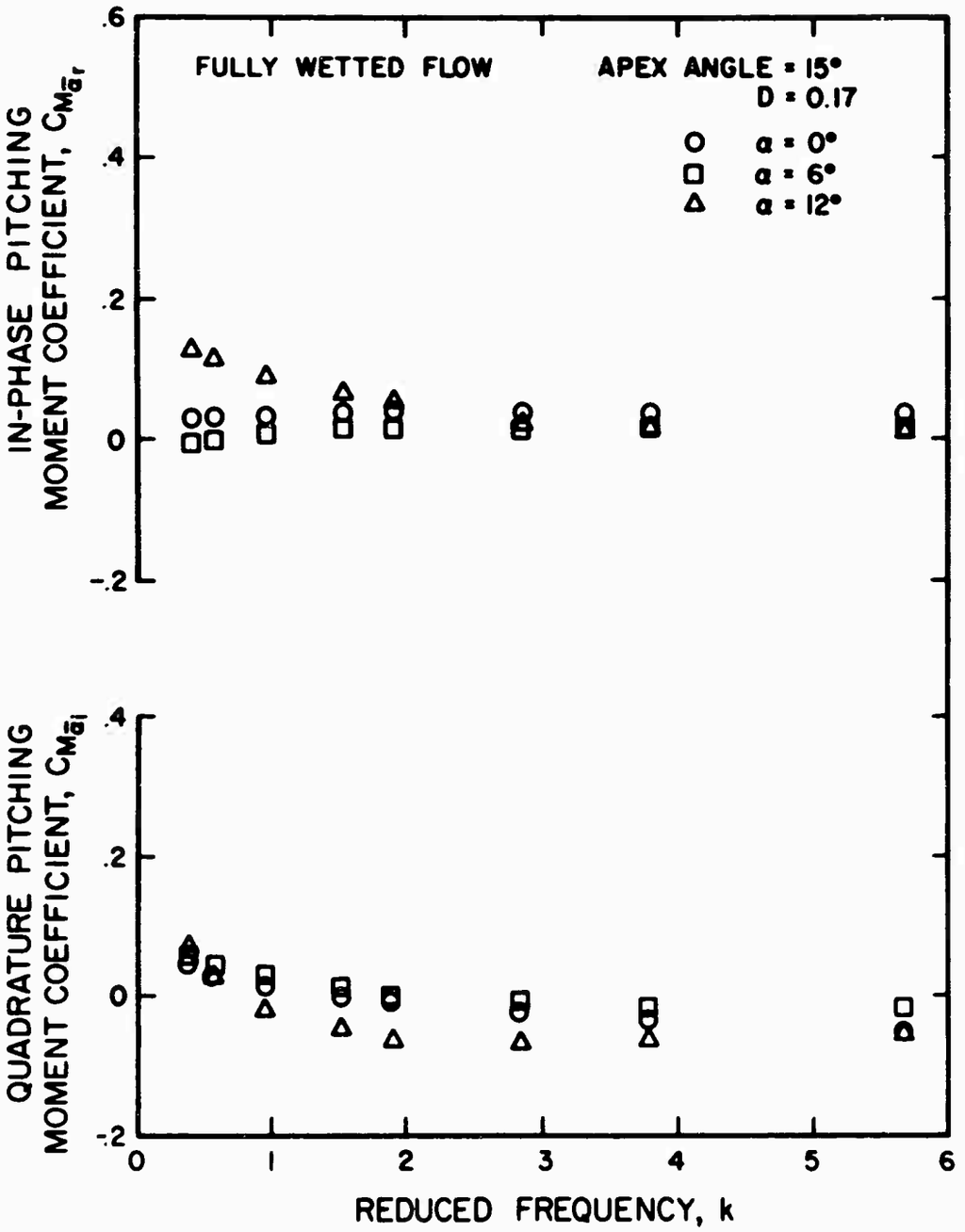

Fig. 17 Unsteady pitching moment coefficients for a fully wetted delta wing at 0.17 chords submergence at various angles of attack.

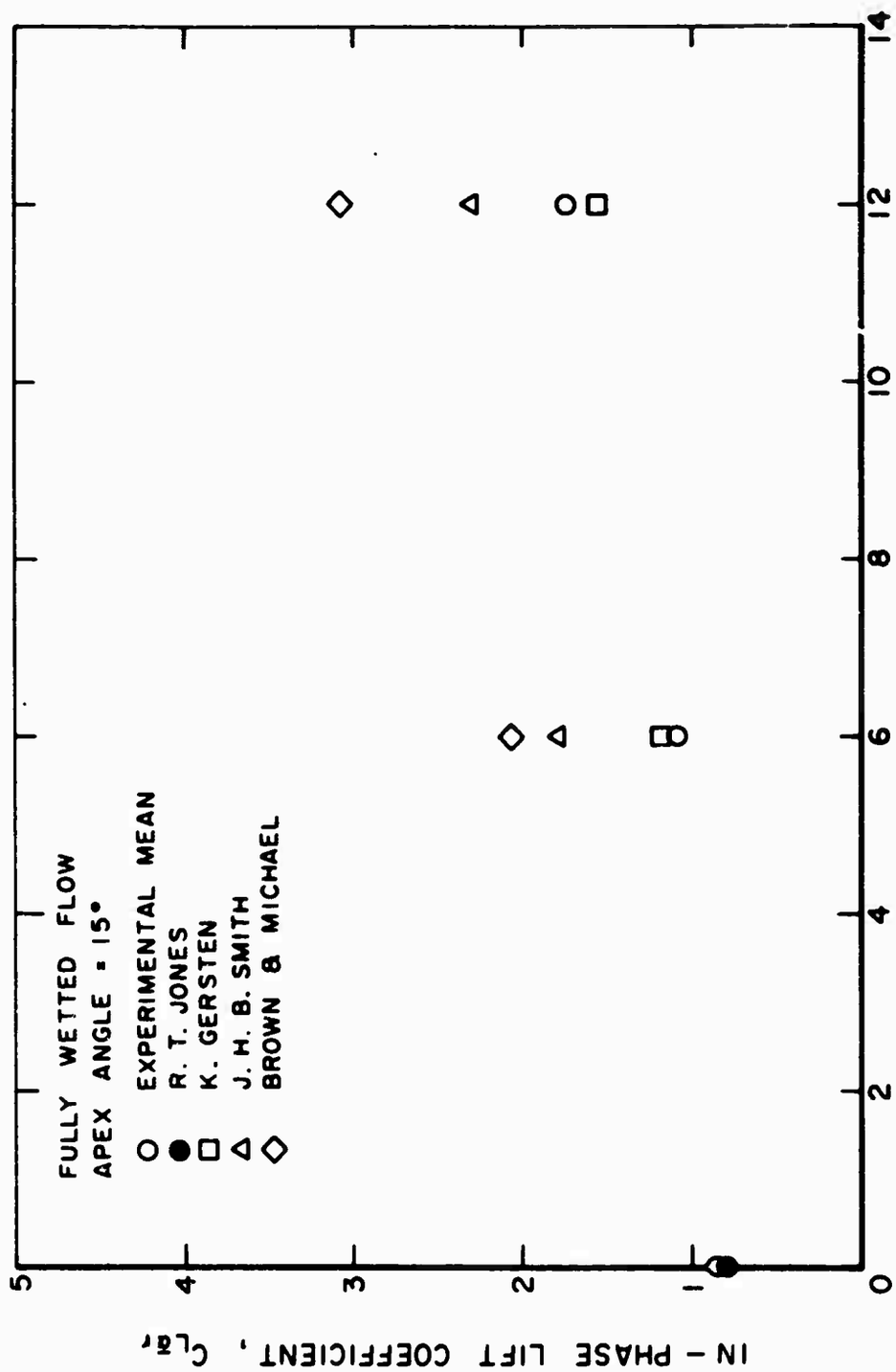

Fig. 18 Summary of various steady theories of lift slope for a fully wetted 15° apex angle delta wing vs angle of attack together with the present experimental in-phase dynamic lift slope coefficient averaged over the reduced frequencies tested.

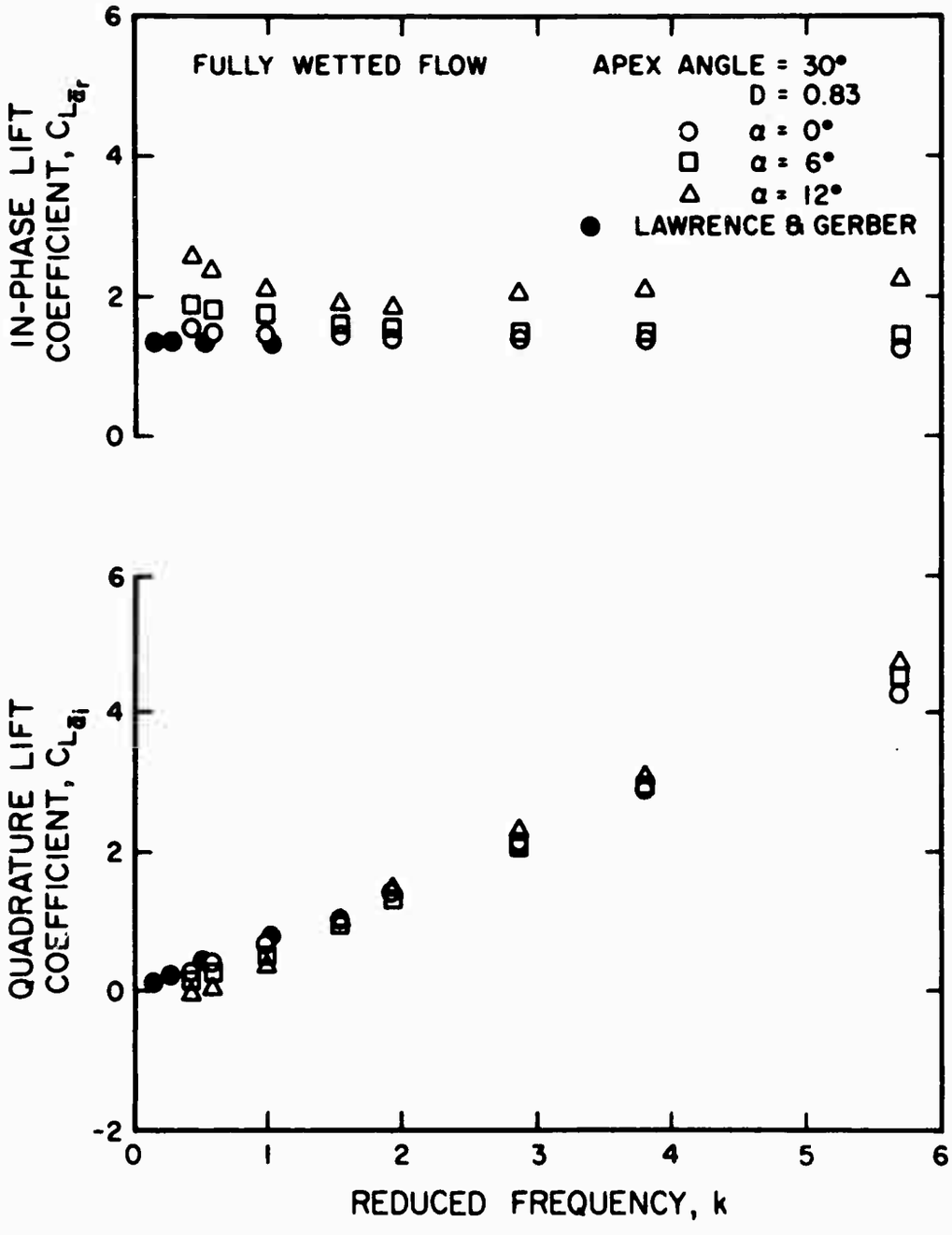

Fig. 19 Unsteady lift coefficients for a fully wetted delta wing of 30° apex angle with 0.83 chords submergence.

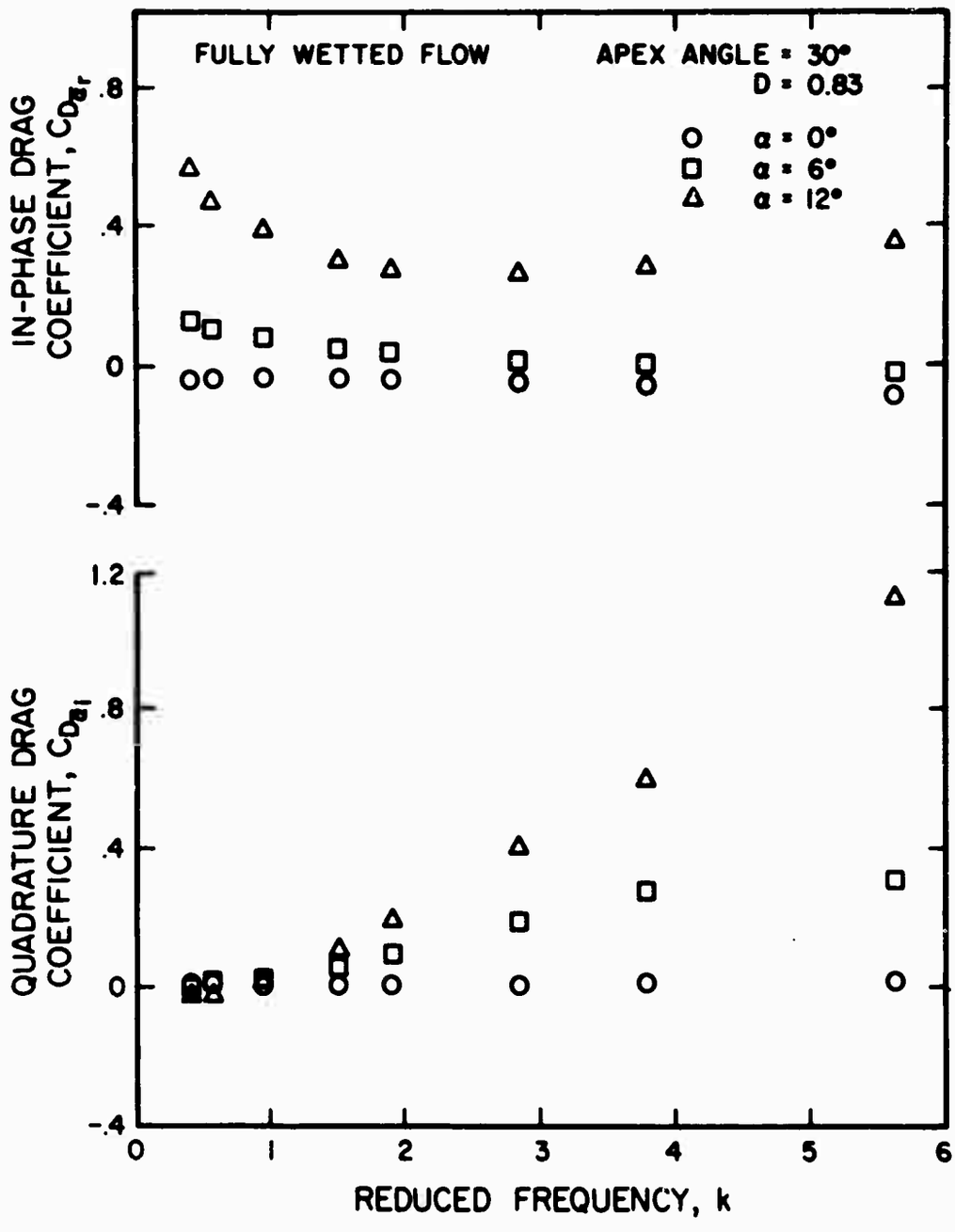

Fig. 20 Unsteady drag coefficients for a fully wetted delta wing of 30° apex angle with 0.83 chords submergence.

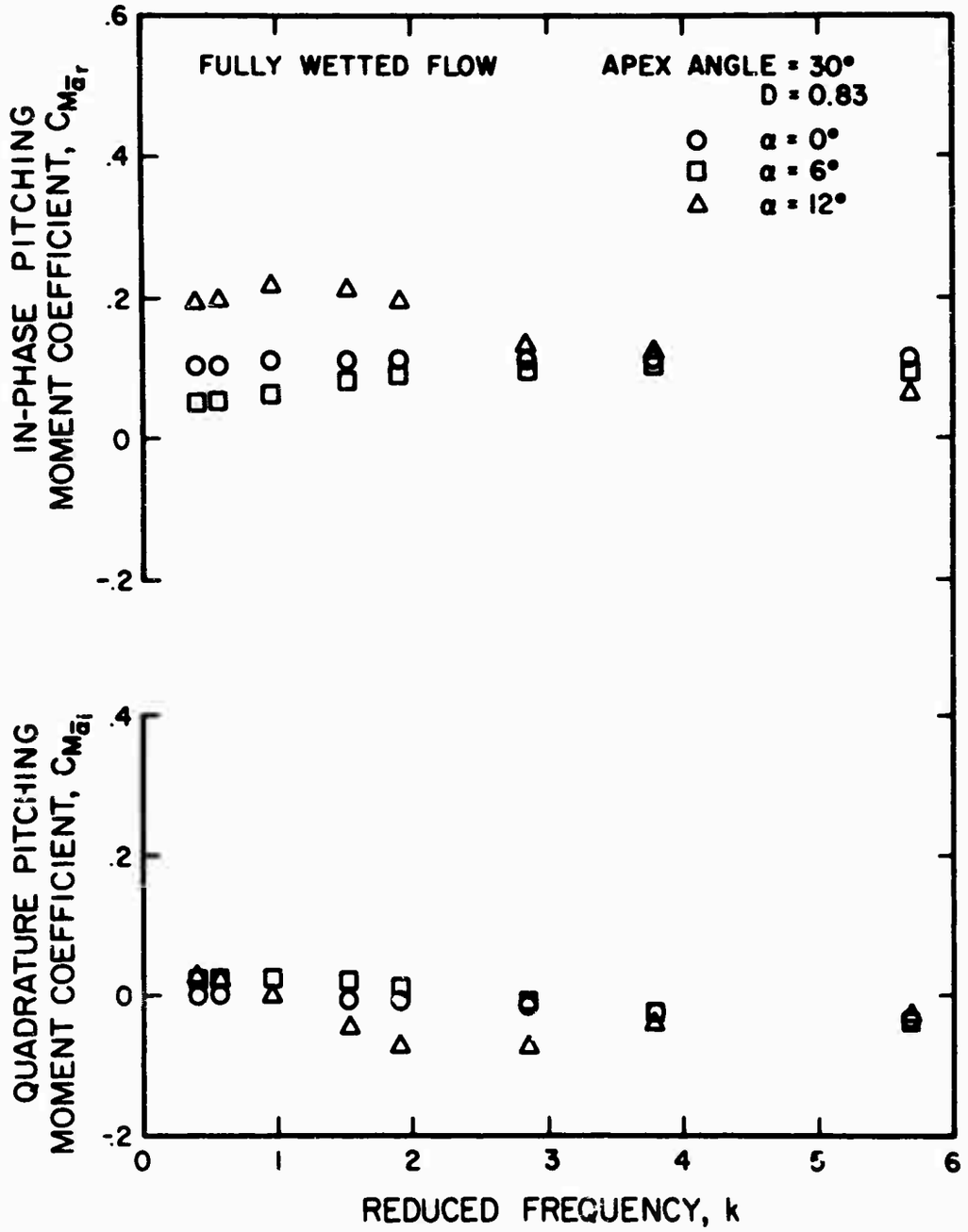

Fig. 21 Unsteady pitching moment coefficients for a fully wetted delta wing of 30° apex angle with 0.83 chords submergence.

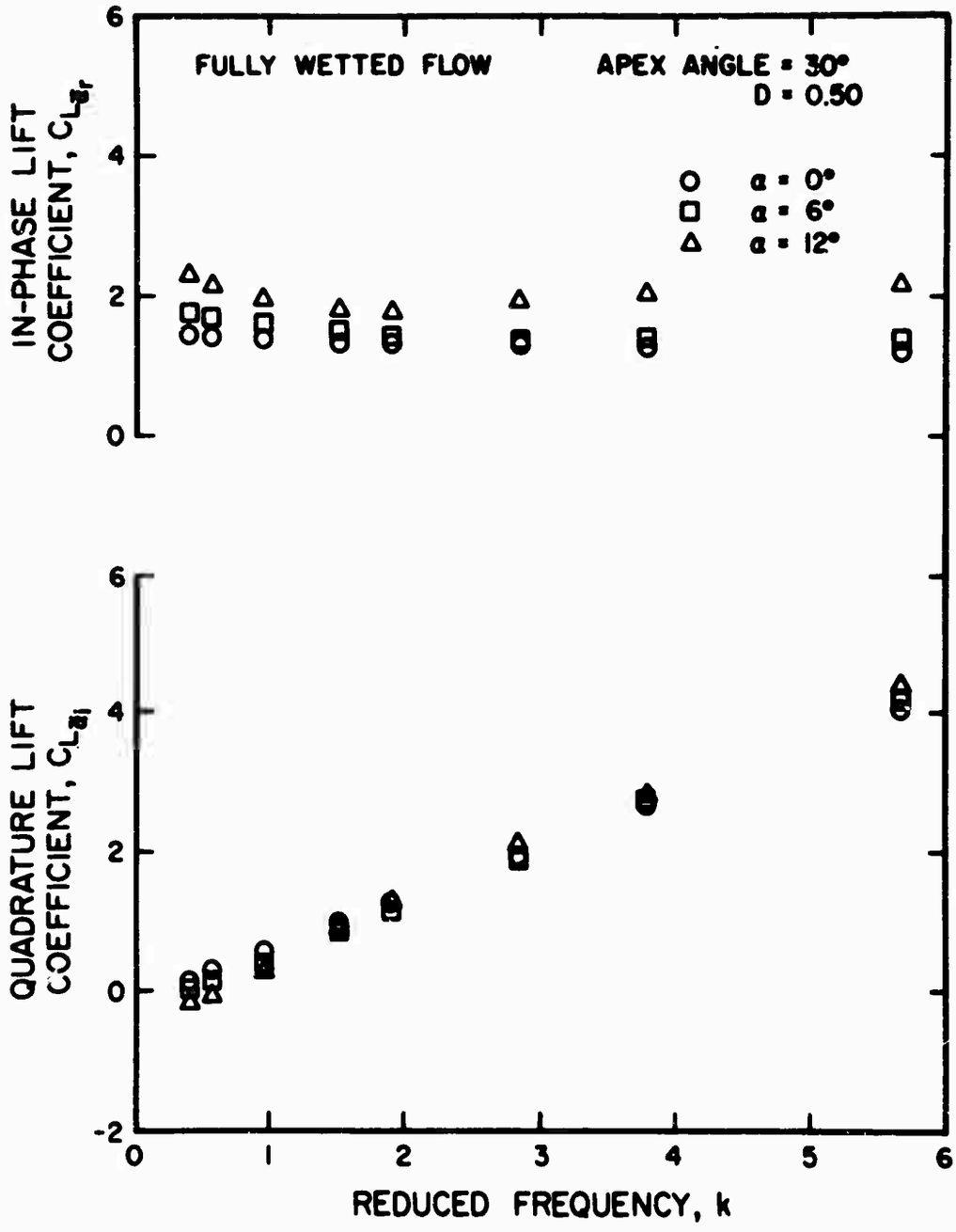

Fig. 22 Unsteady lift coefficients for a fully wetted delta wing of 30° apex angle with 0.5 chords submergence.

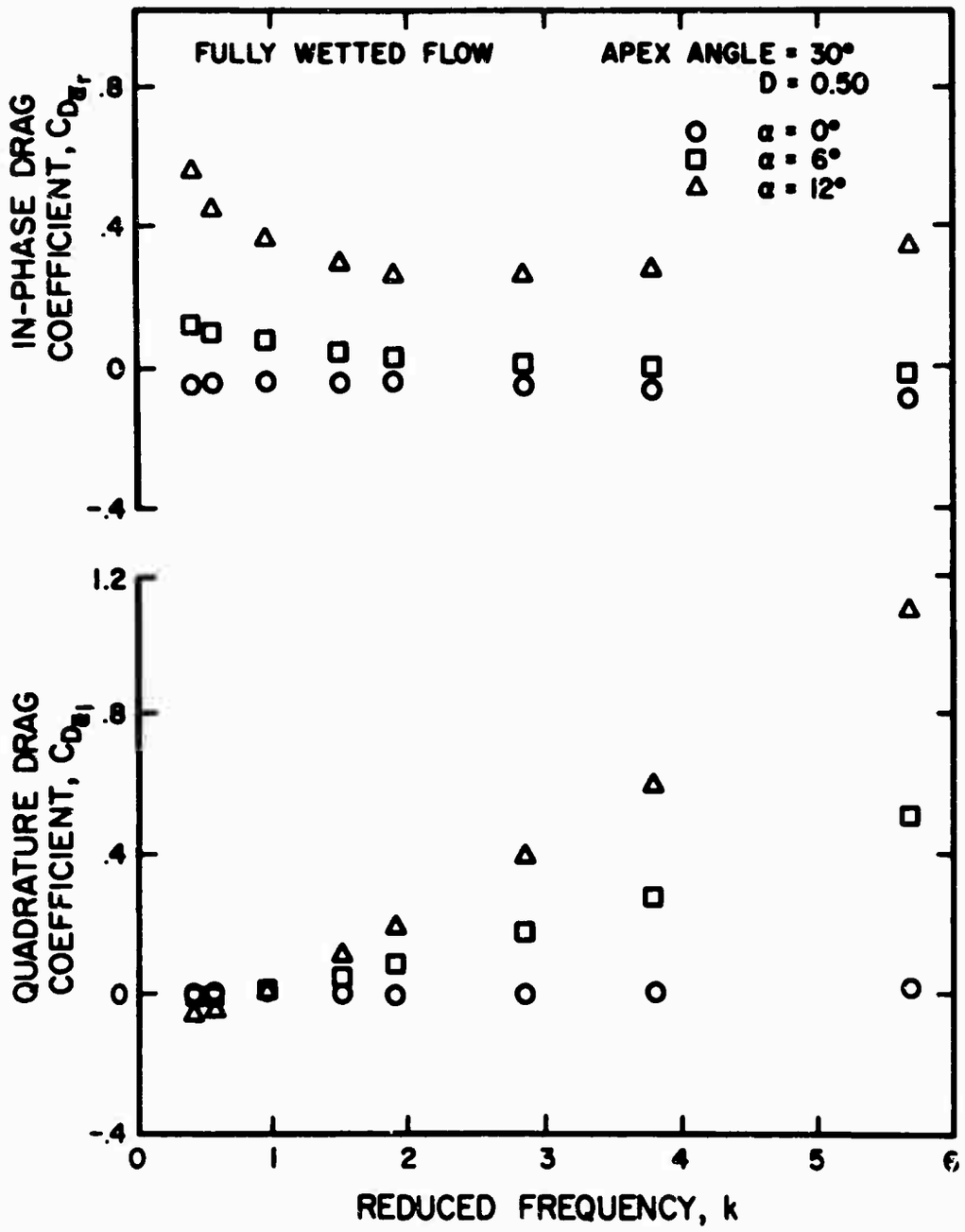

Fig. 23 Unsteady drag coefficients for a fully wetted delta wing of 30° apex angle with 0.5 chords submergence.

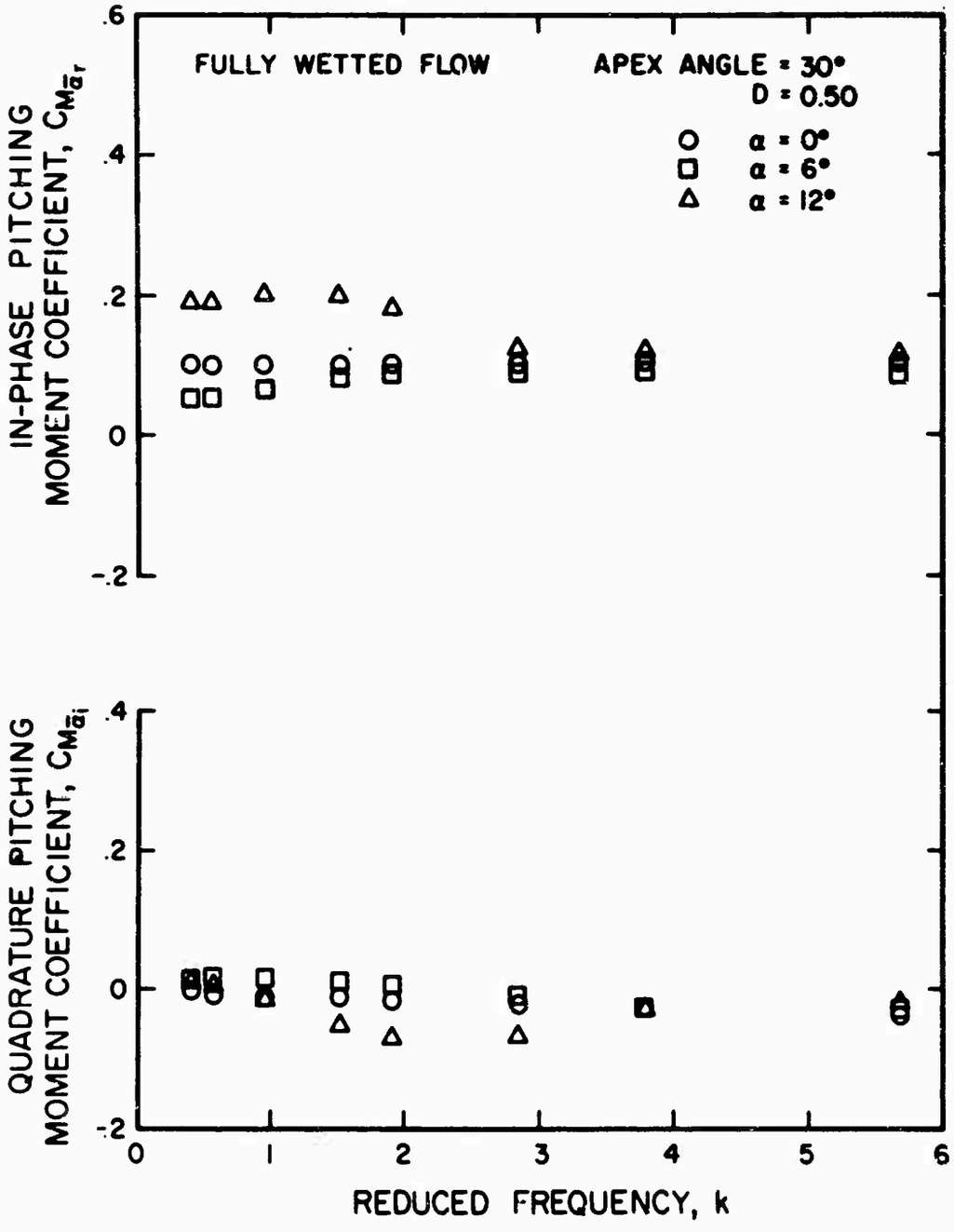

Fig. 24 Unsteady pitching moment coefficients for a fully wetted delta wing of 30° apex angle with 0.5 chords submergence.

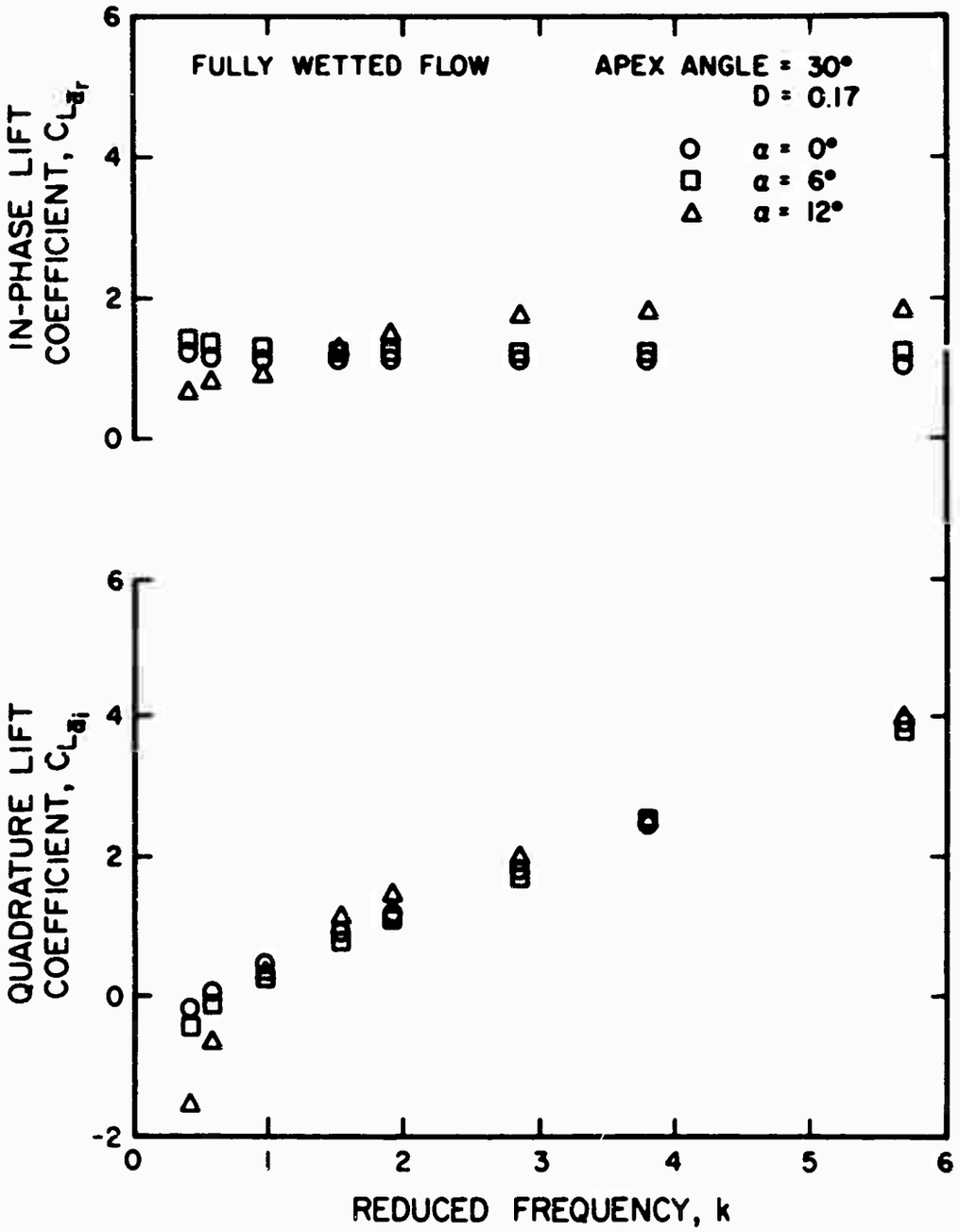

Fig. 25 Unsteady lift coefficients for a fully wetted delta wing of 30° apex angle with 0.17 chords submergence.

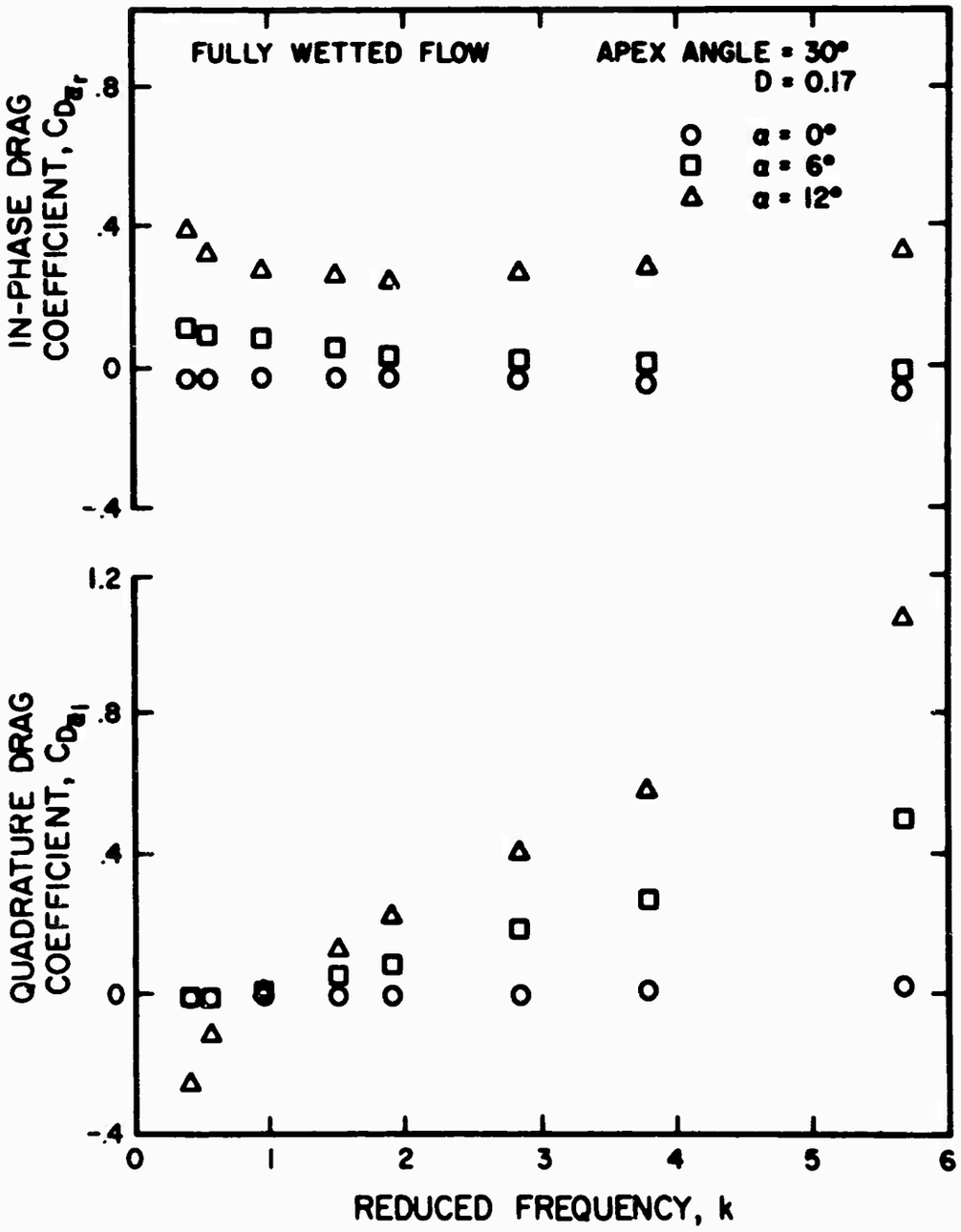

Fig. 26 Unsteady drag coefficients for a fully wetted delta wing of 30° apex angle with 0.17 chords submergence.

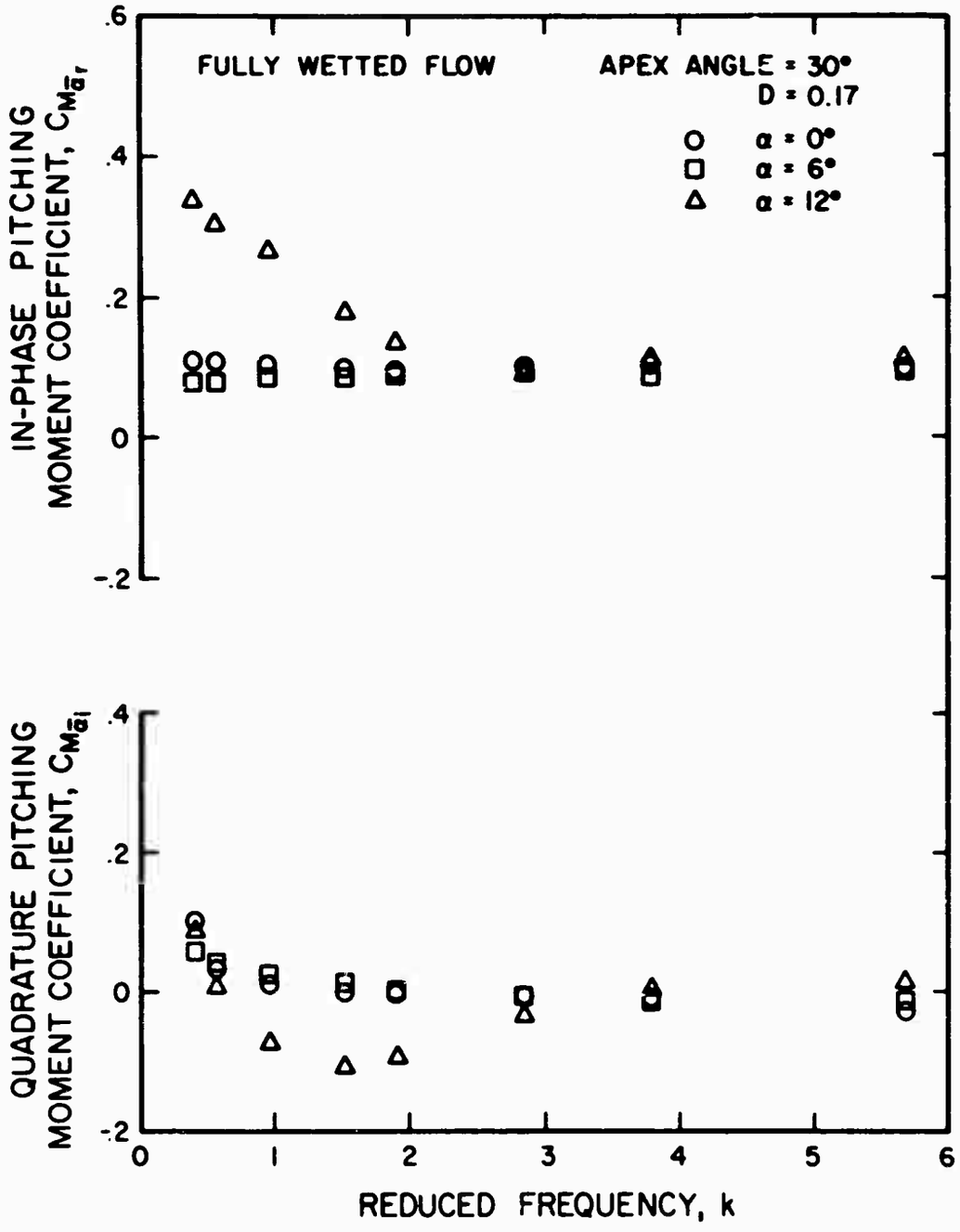

Fig. 27 Unsteady pitching moment coefficients for a fully wetted delta wing of 30° apex angle with 0.17 chords submergence.

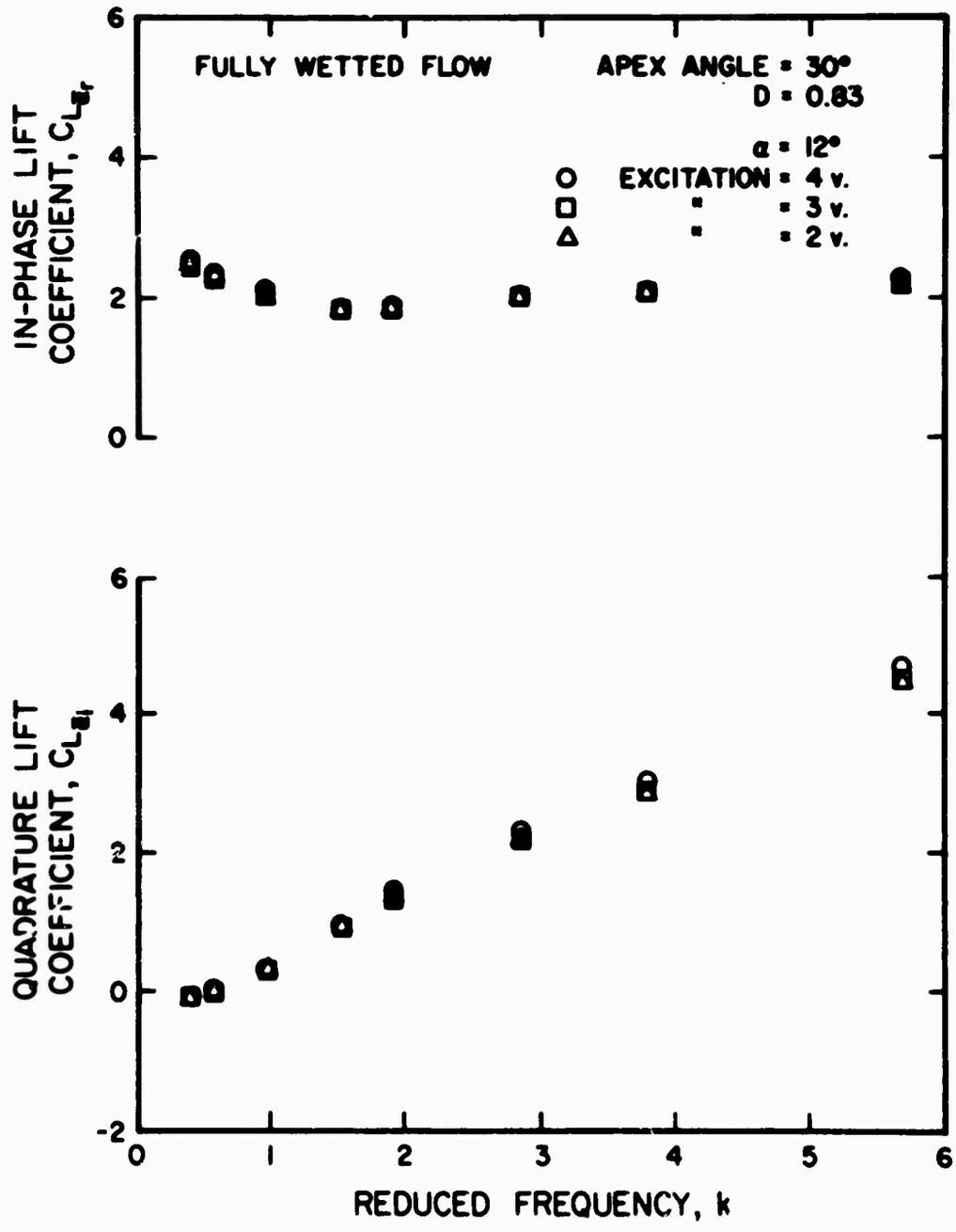

Fig. 28 Unsteady lift coefficients on a fully wetted delta wing of 30^{o} apex angle for various heaving amplitudes.

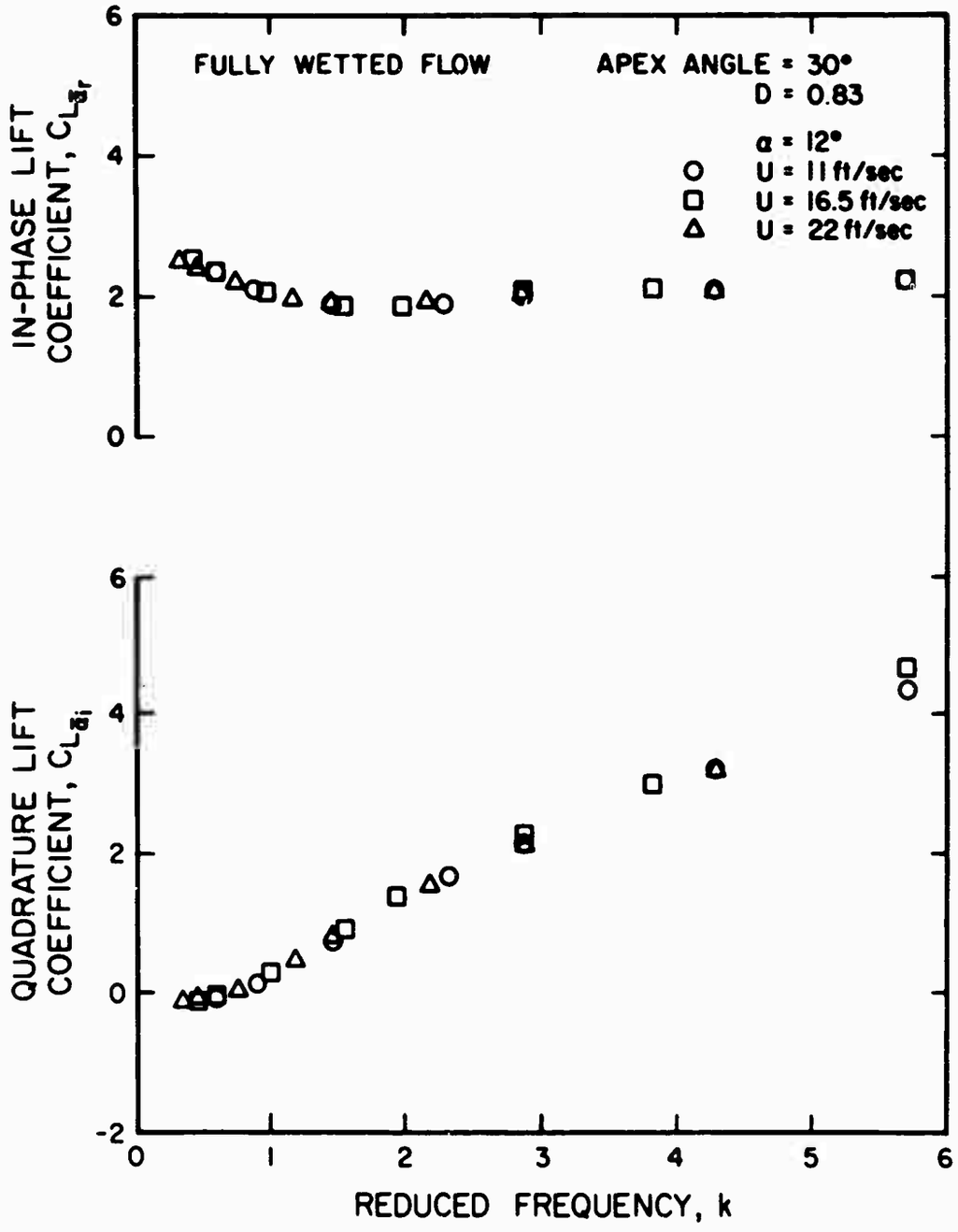

Fig. 29 Unsteady lift coefficients on a fully wetted delta wing of 30° apex angle showing the effect of various free-stream velocities.

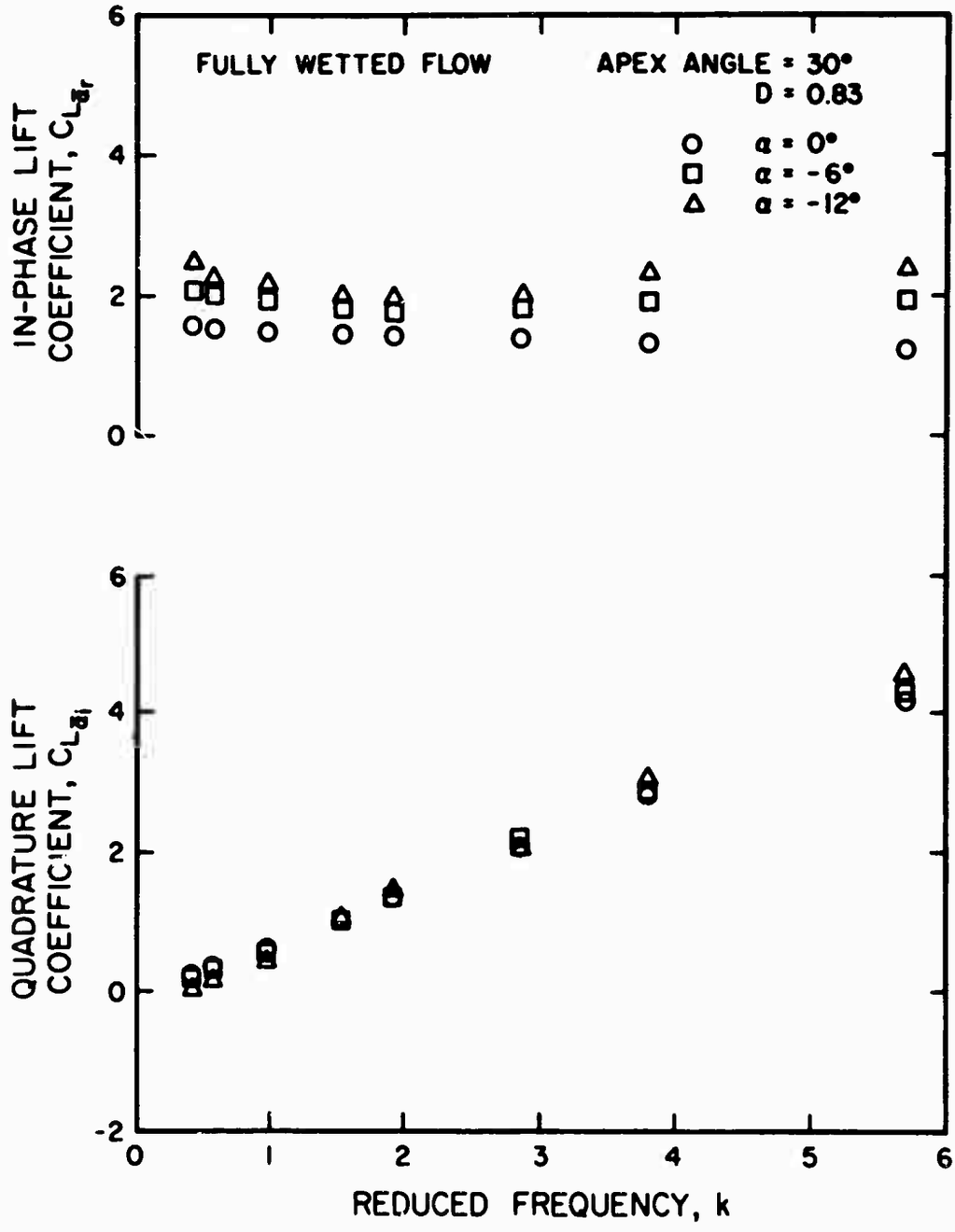

Fig. 30 Unsteady lift coefficients for negative angles of attack on a fully wetted 30° apex angle delta wing hydrofoil.

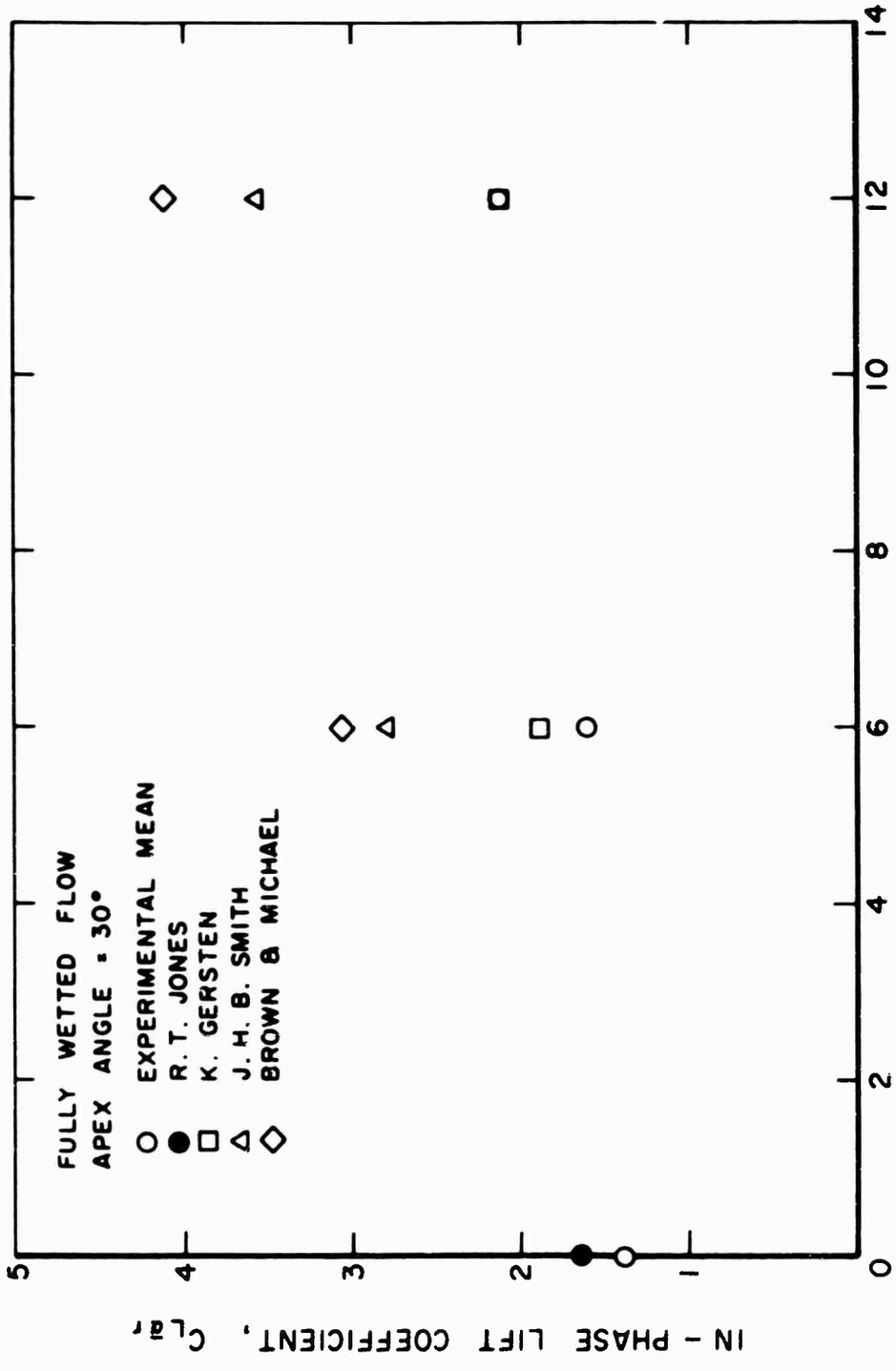

Fig. 31 Summary of various steady theories of lift slope for a fully wetted 30° apex angle delta wing vs angle of attack together with the present experimental in-phase dynamic lift slope coefficient averaged over the reduced frequencies tested.

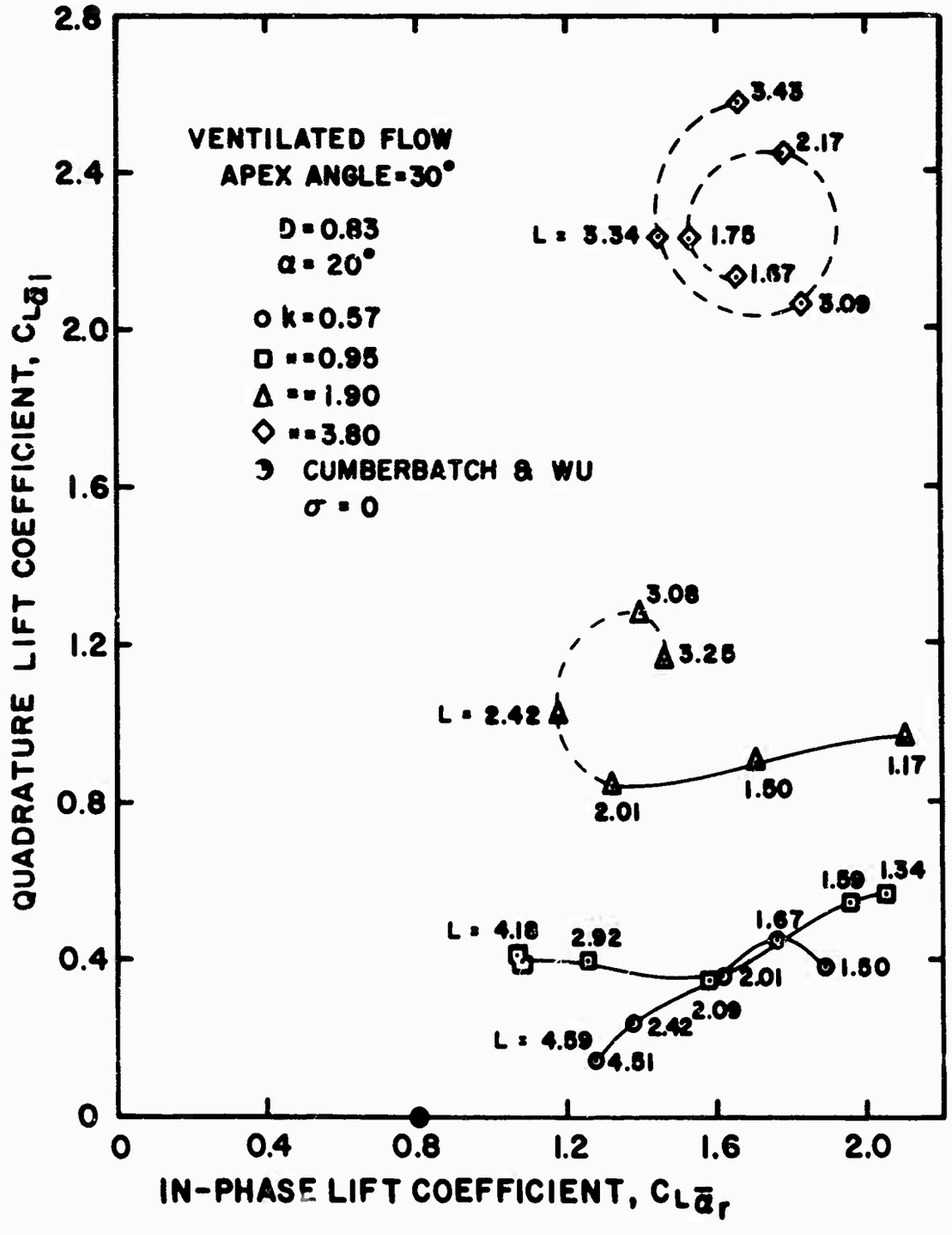

Fig. 32 Unsteady lift coefficients in forced ventilation flow past a 30° delta wing hydrofoil oscillating in heave for various frequencies. The number on each of the curves is the mean length of the ventilation cavity expressed in chords.

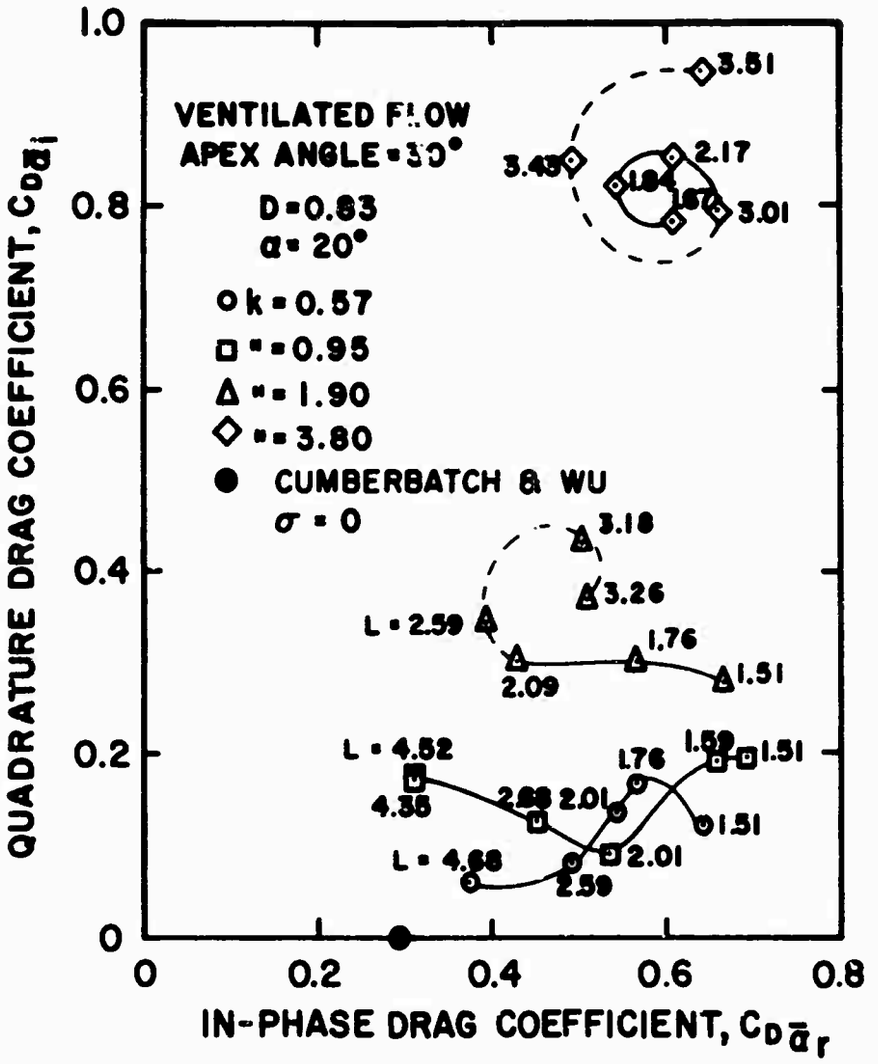

Fig. 33 Unsteady drag coefficients for the configuration of Fig. 32.

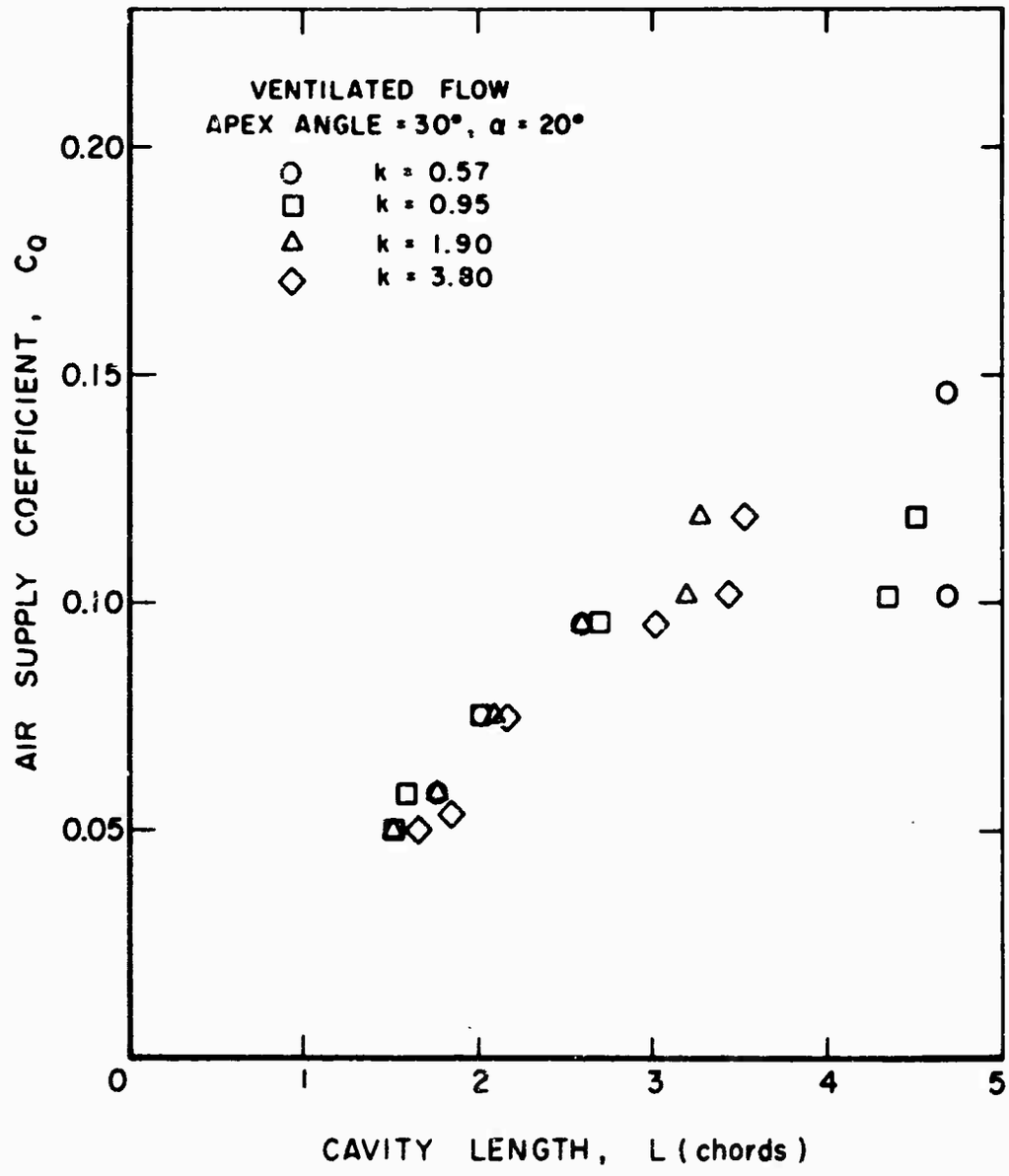

Fig. 34 Air supply coefficient as a function of cavity length showing the effect of reduced frequency.

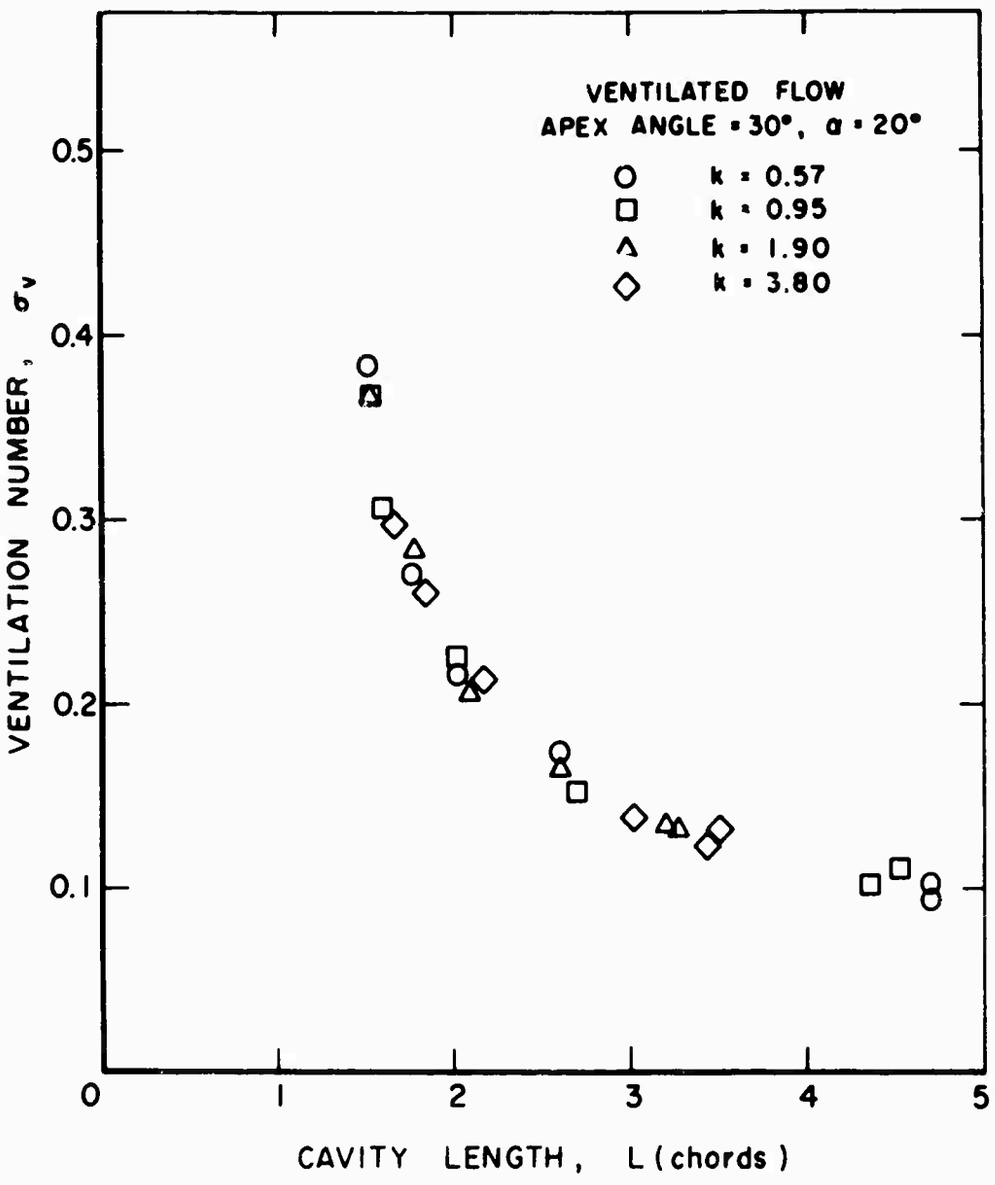

Fig. 35 Ventilation number as a function of cavity length showing the effect of reduced frequency.

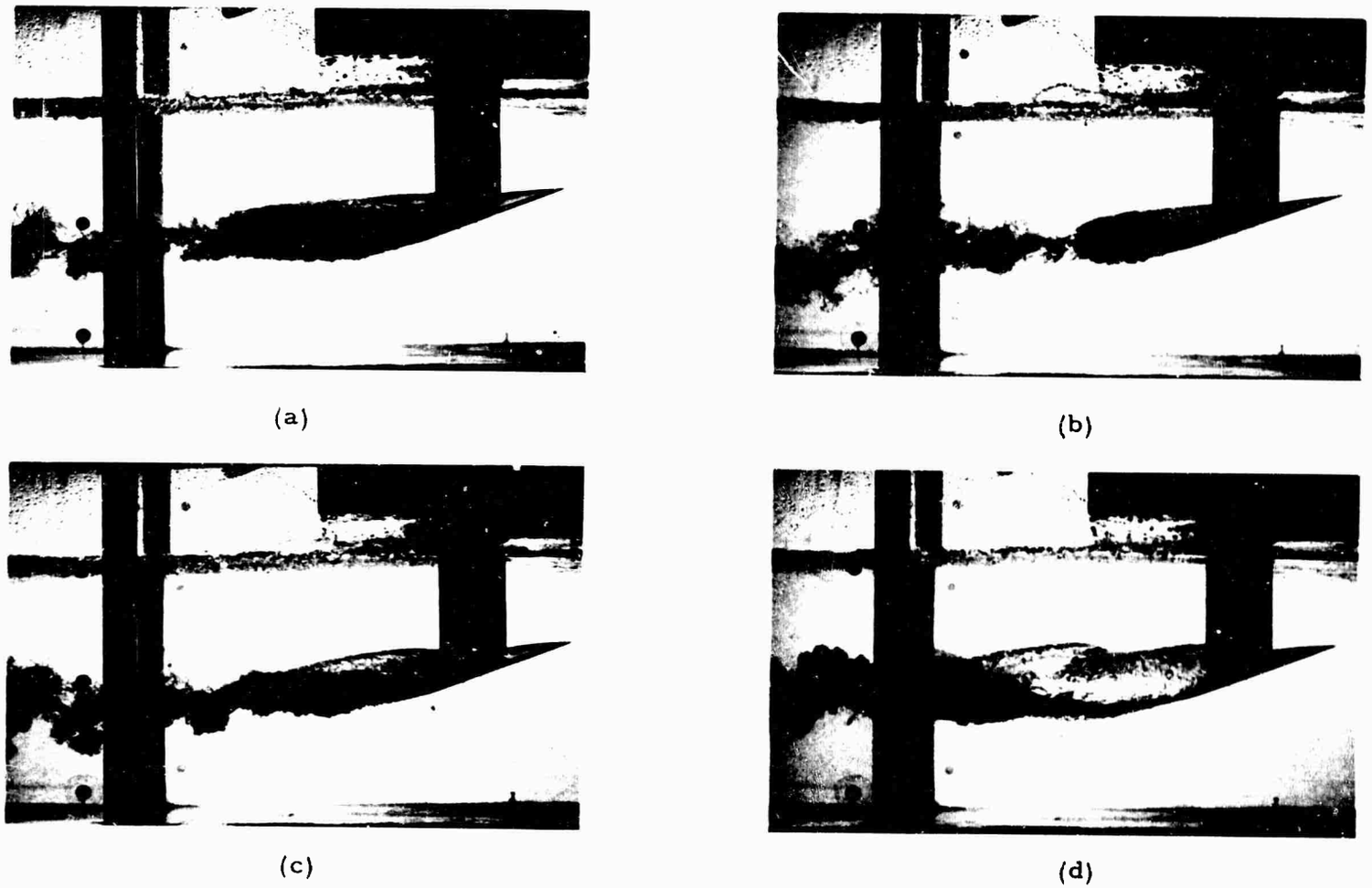

(a) (b) (c) (d)

Fig. 36 Flash photographs of the ventilated cavity on the 30° delta wing at various reduced frequencies k and ventilation coefficients c_Q.

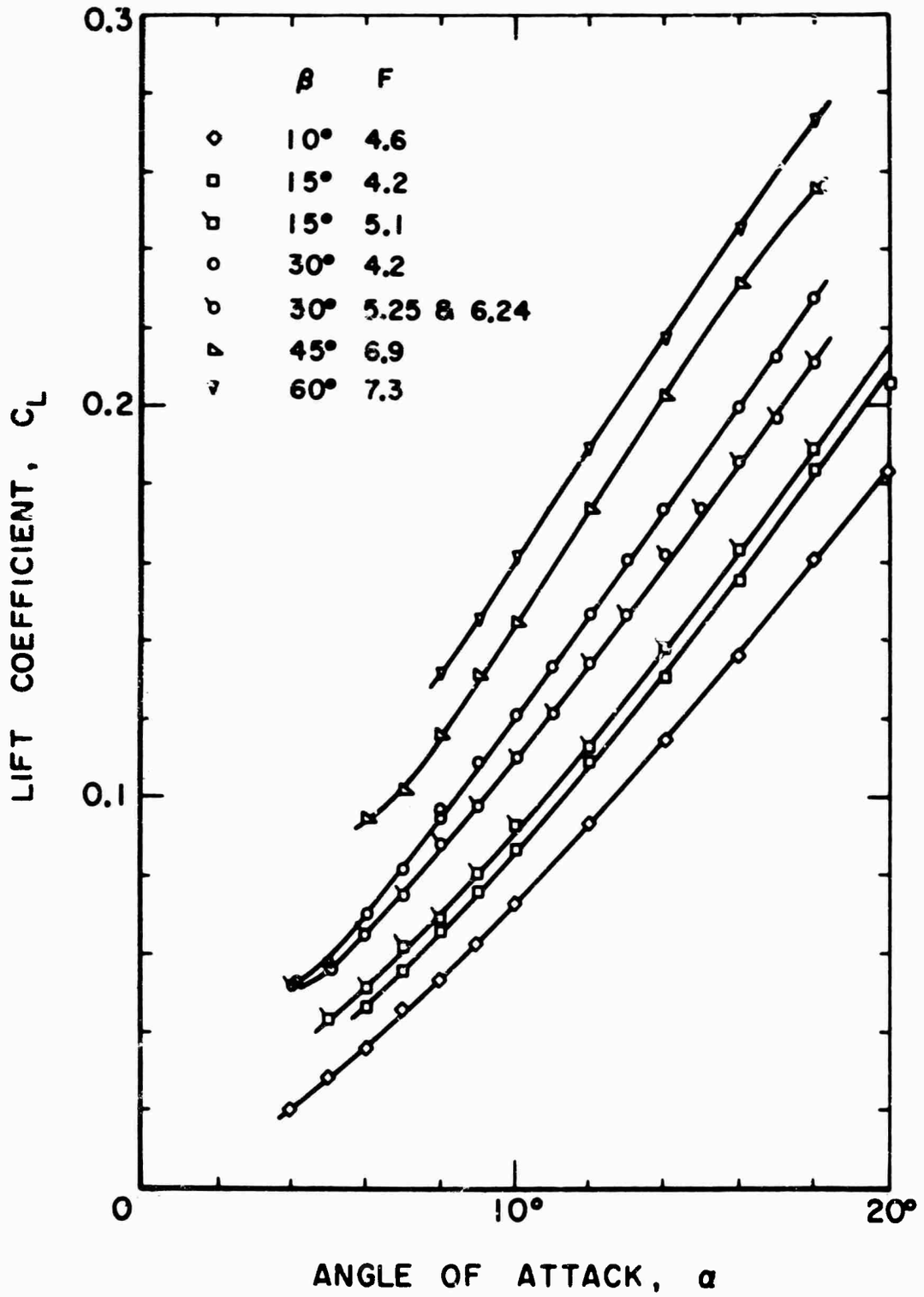

Fig. 37 Summary of experimental data for the steady planing lift coefficient of a family of delta wing hydrofoils vs angle of attack.

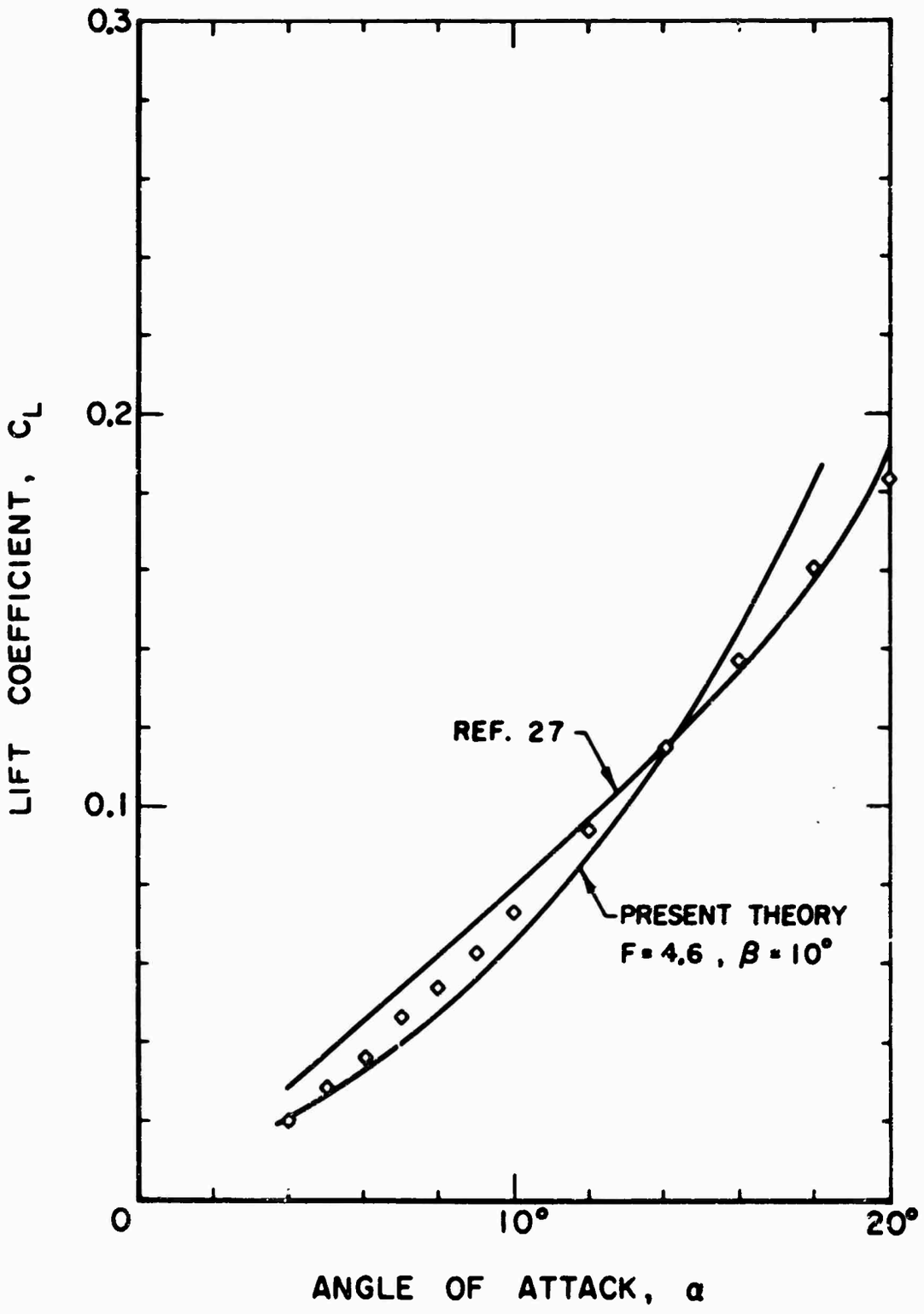

Fig. 38 Lift coefficient vs angle of attack for steady planing of a 10° delta wing.

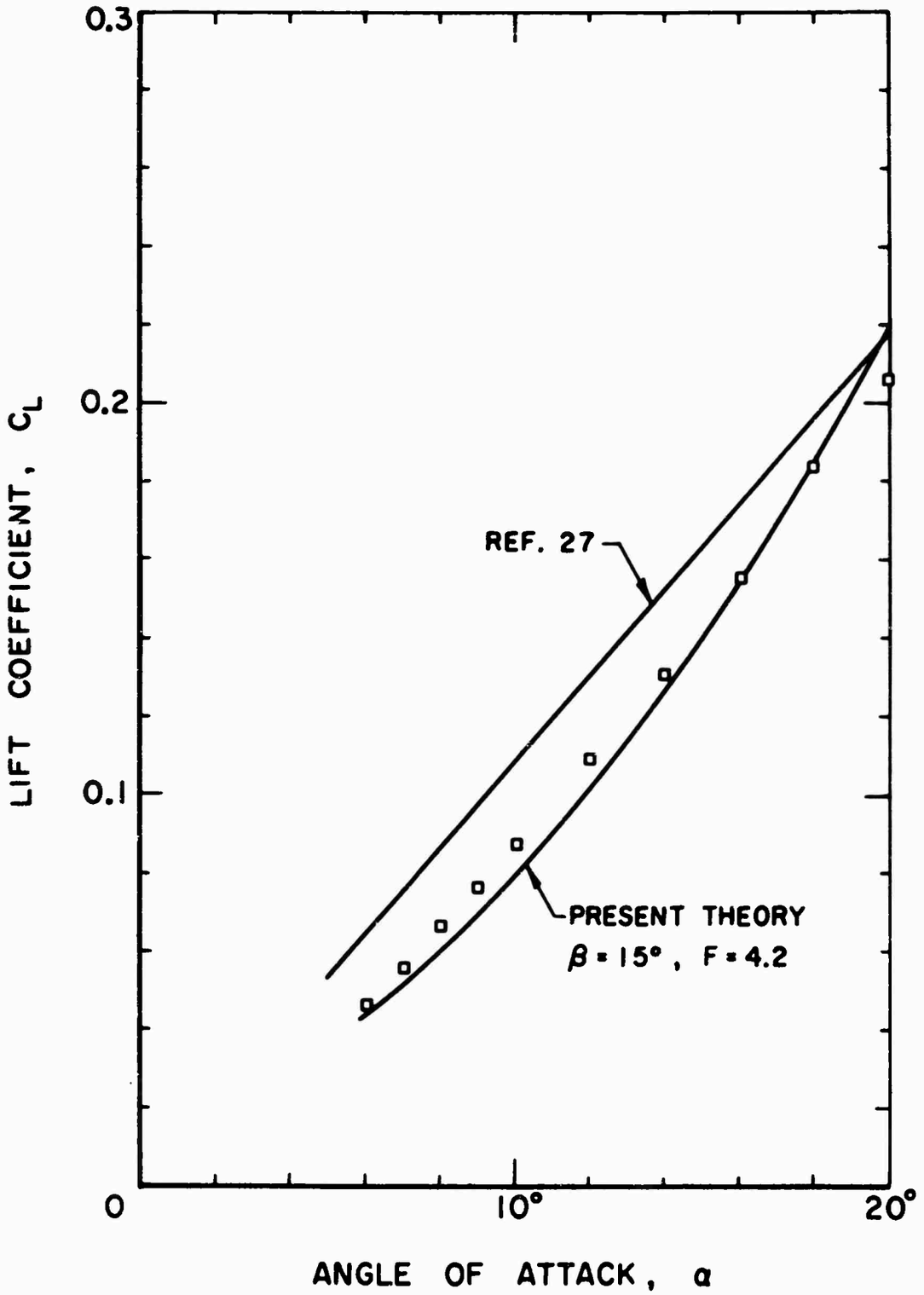

Fig. 39 Lift coefficient vs angle of attack for steady planing of a 15° delta wing.

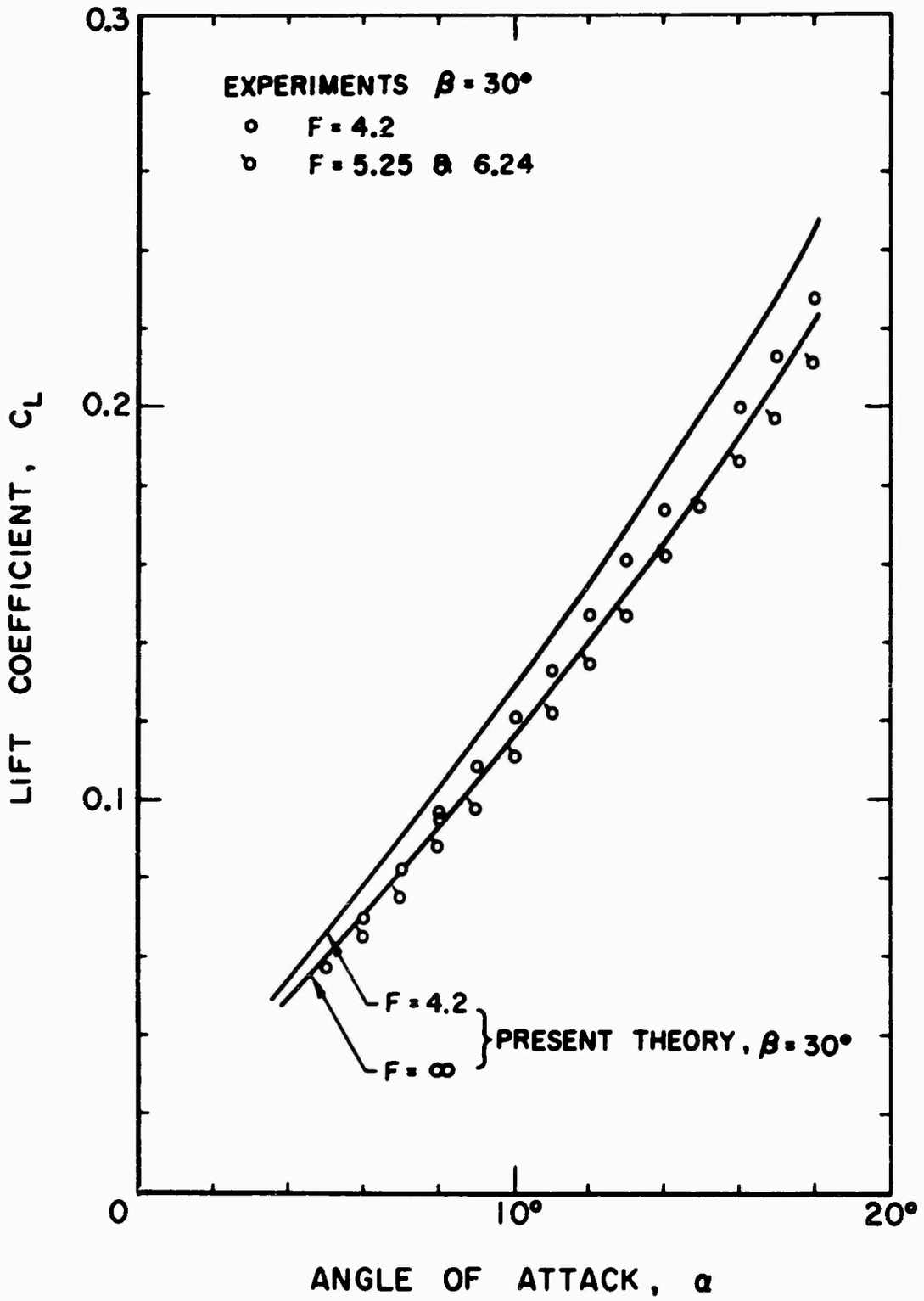

Fig. 40 Lift coefficient vs angle of attack for steady planing of a 30° delta wing.

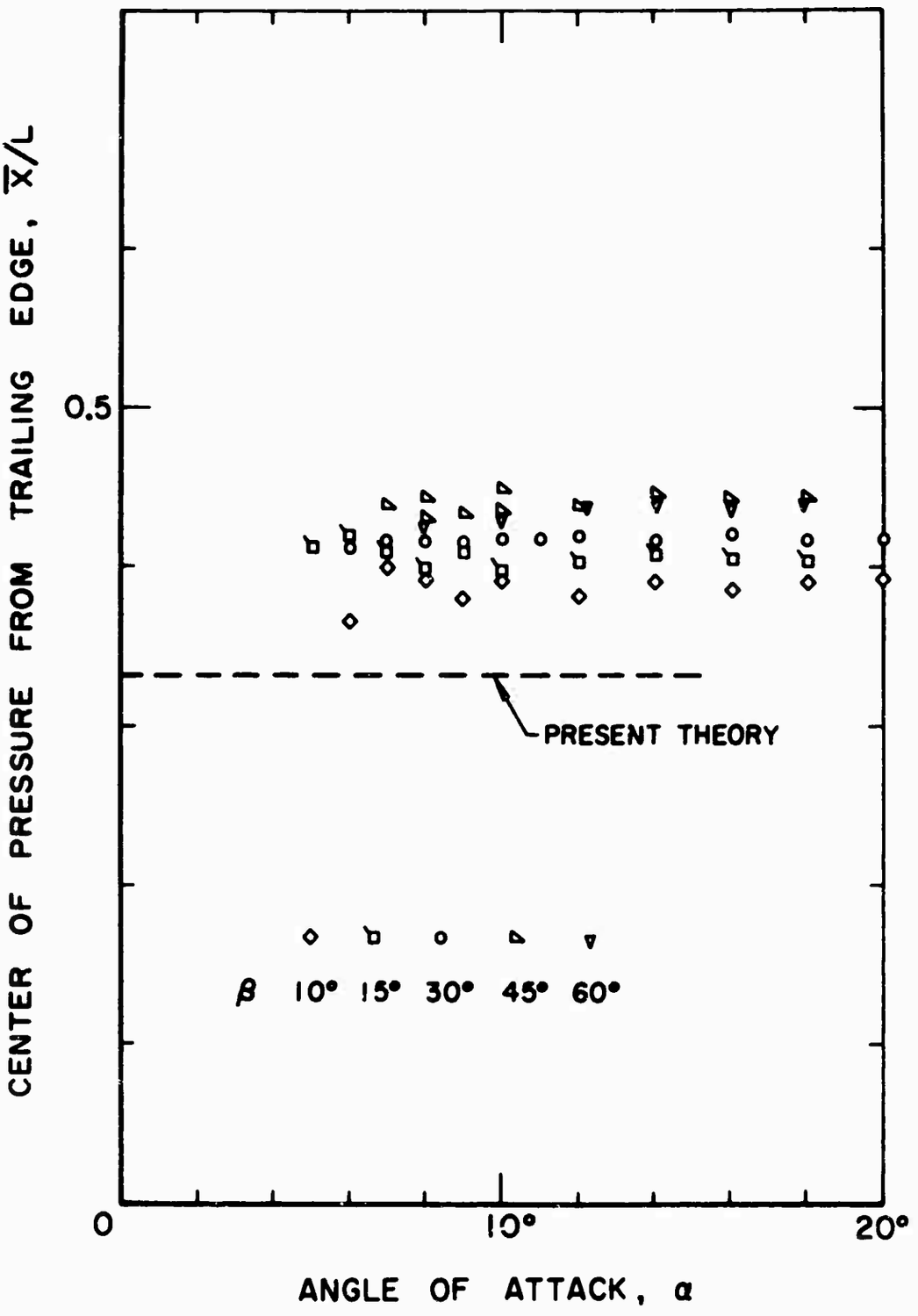

Fig. 41 Location of experimentally measured centers of pressure (from the trailing edge) in steady planing vs angle of attack for the series of delta wings.

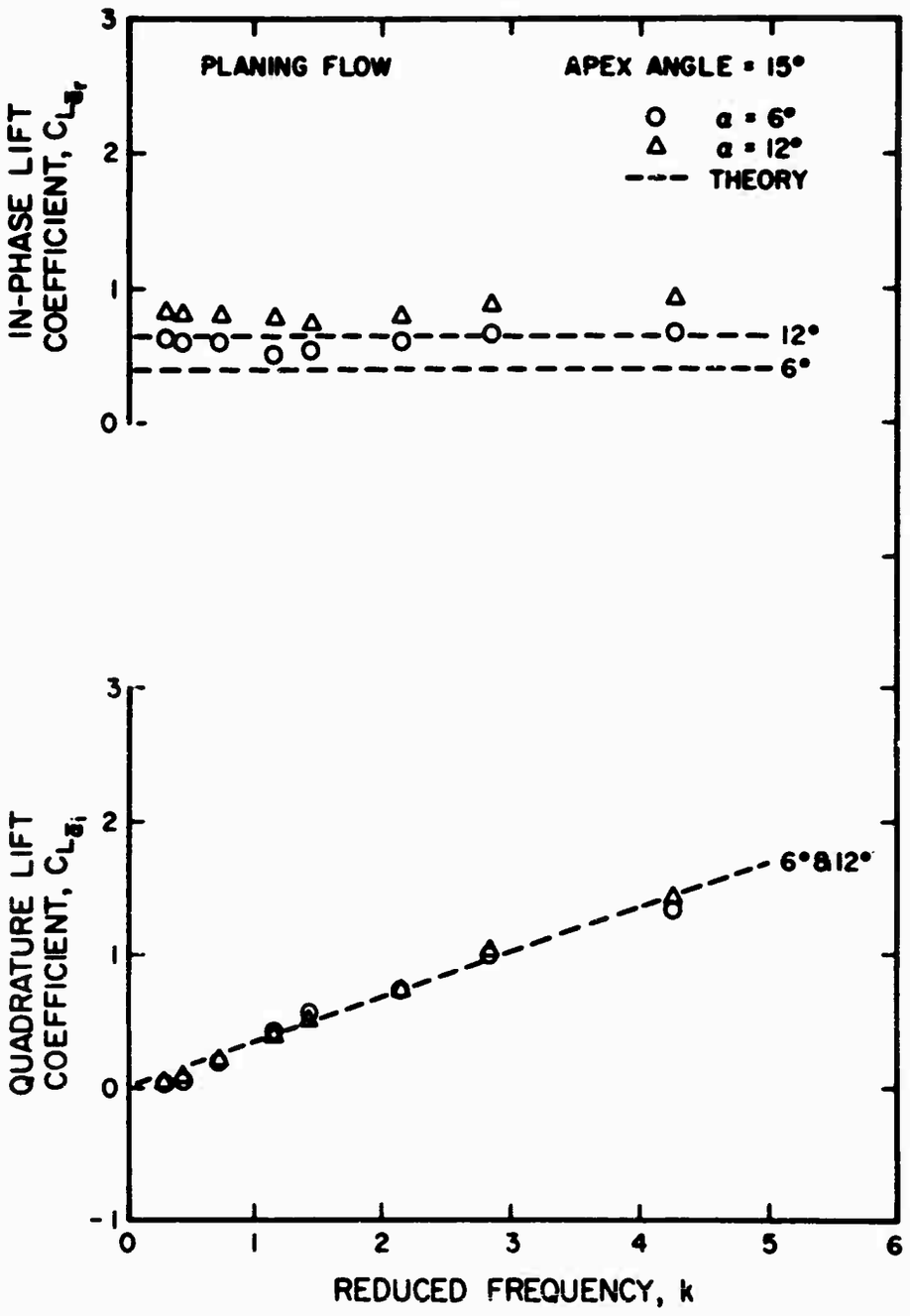

Fig. 42 Unsteady lift coefficients for the planing 15° delta wing.

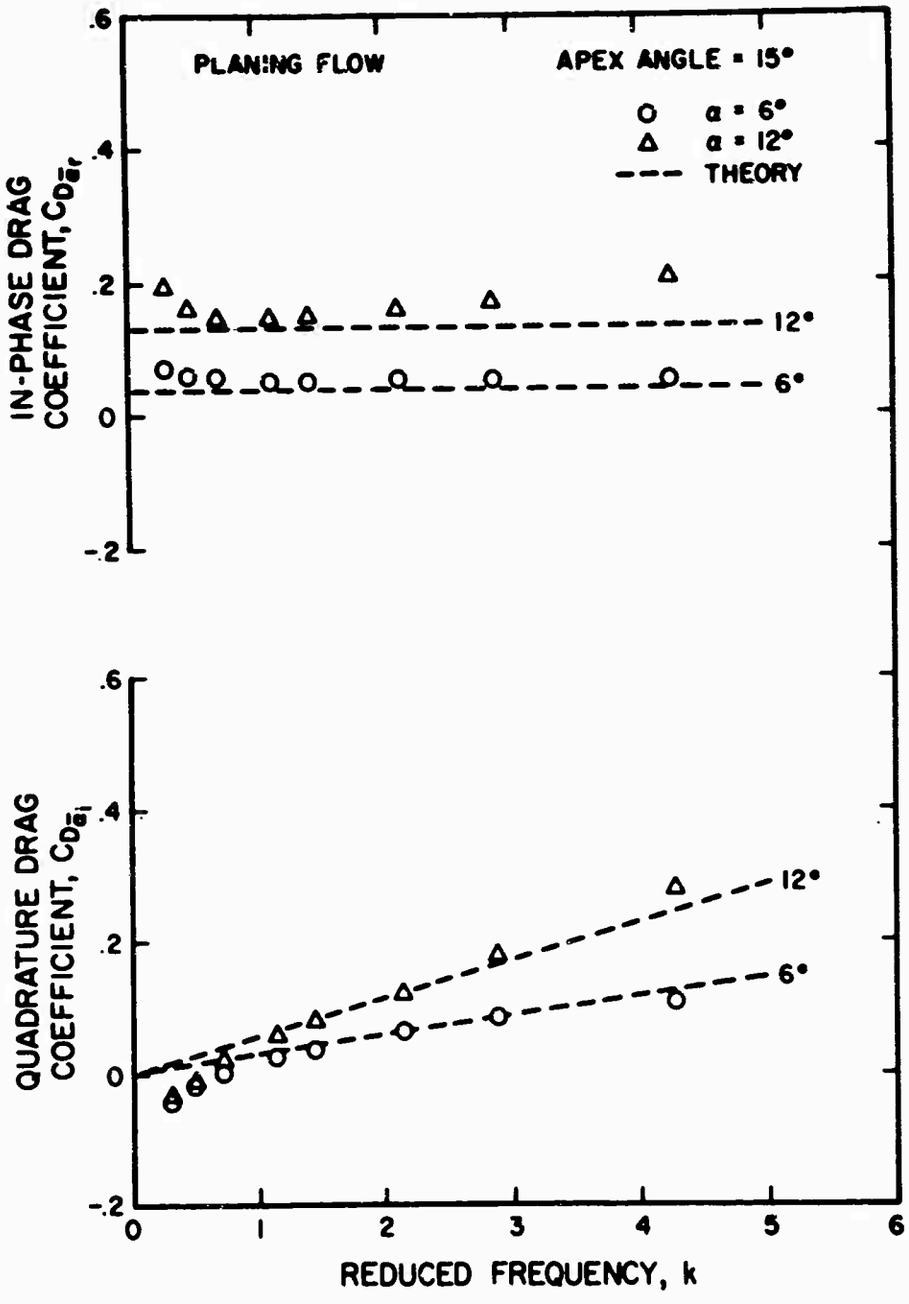

Fig. 43 Unsteady drag coefficients for the planing 15° delta wing.

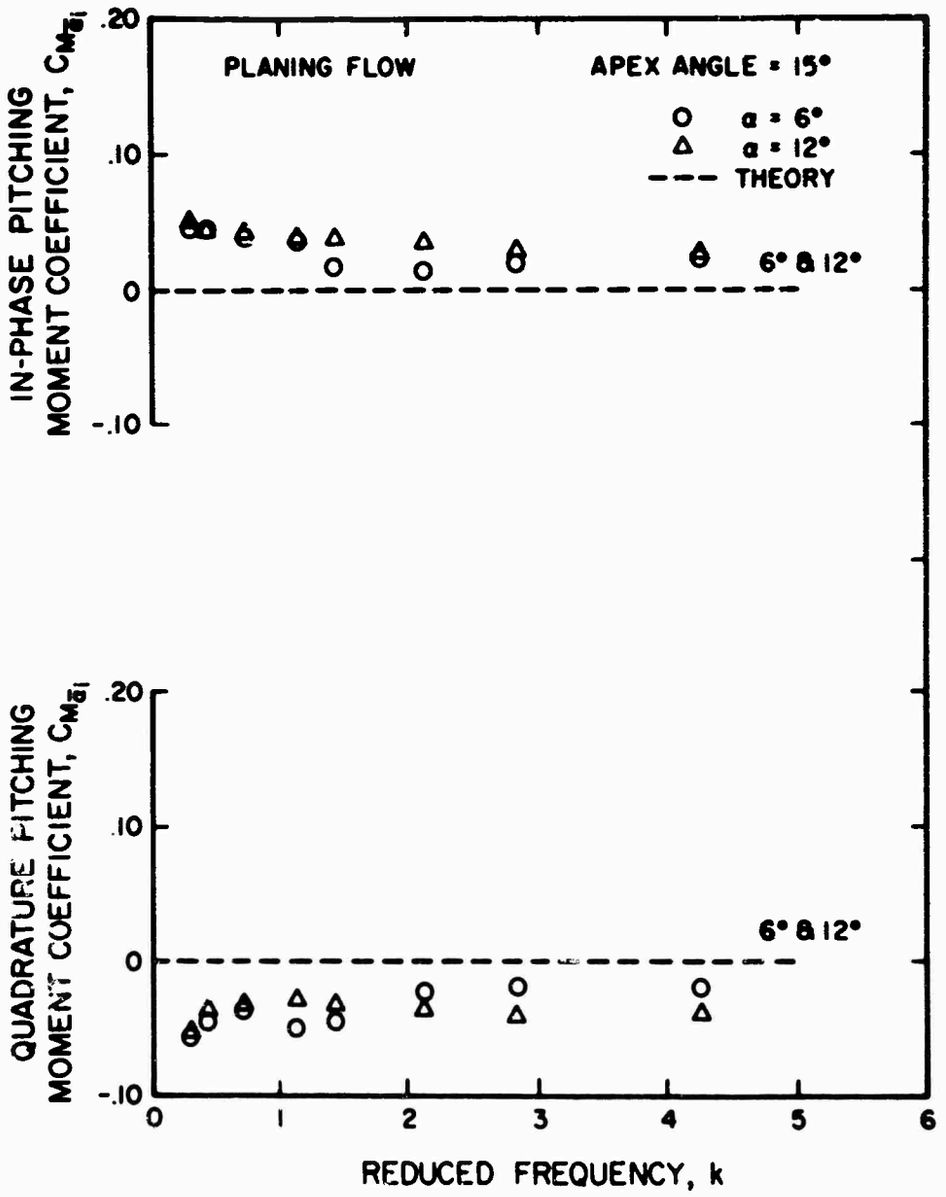

Fig. 44 Unsteady pitching moment coefficients for the planing 15° delta wing.

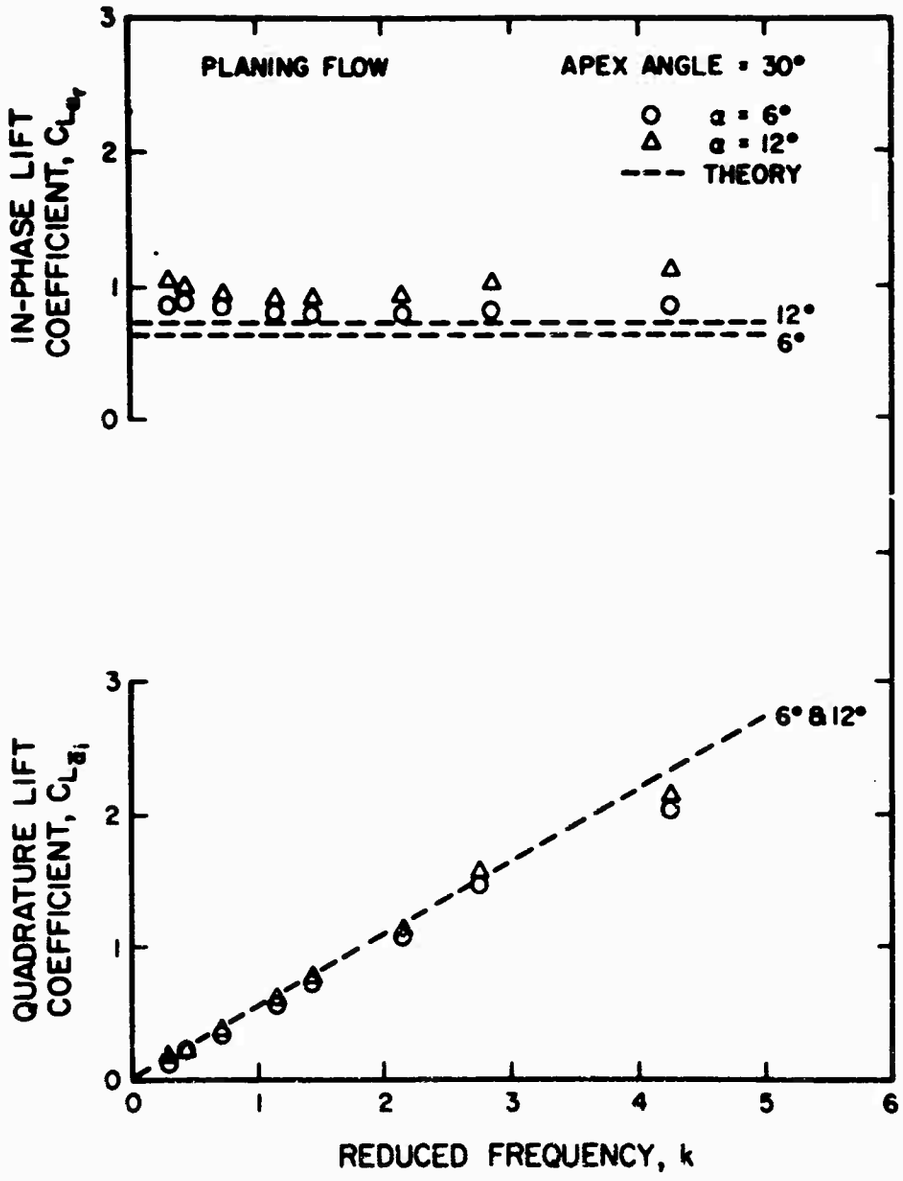

Fig. 45 Unsteady lift coefficients for the planing 30° delta wing.

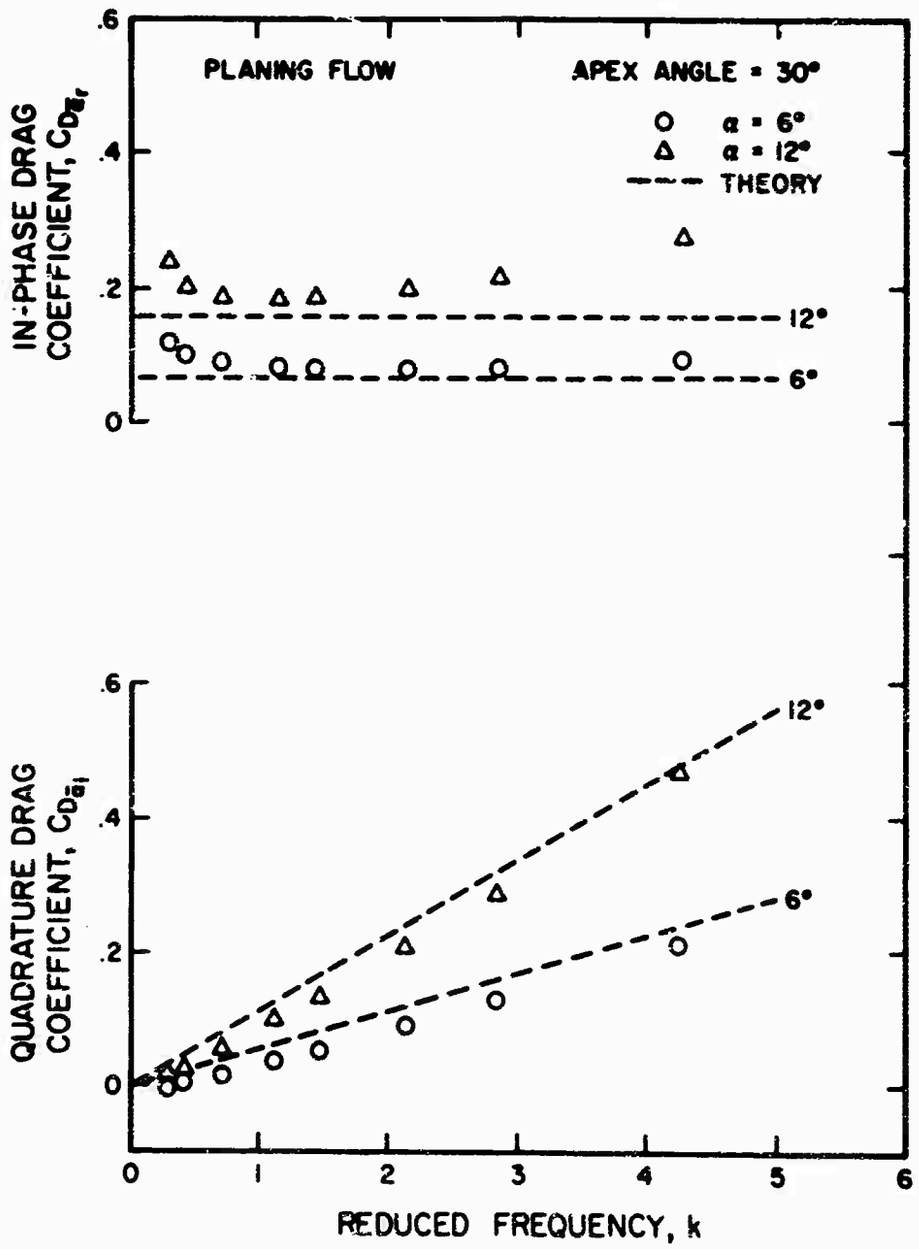

Fig. 46 Unsteady drag coefficients for the planing 30° delta wing.

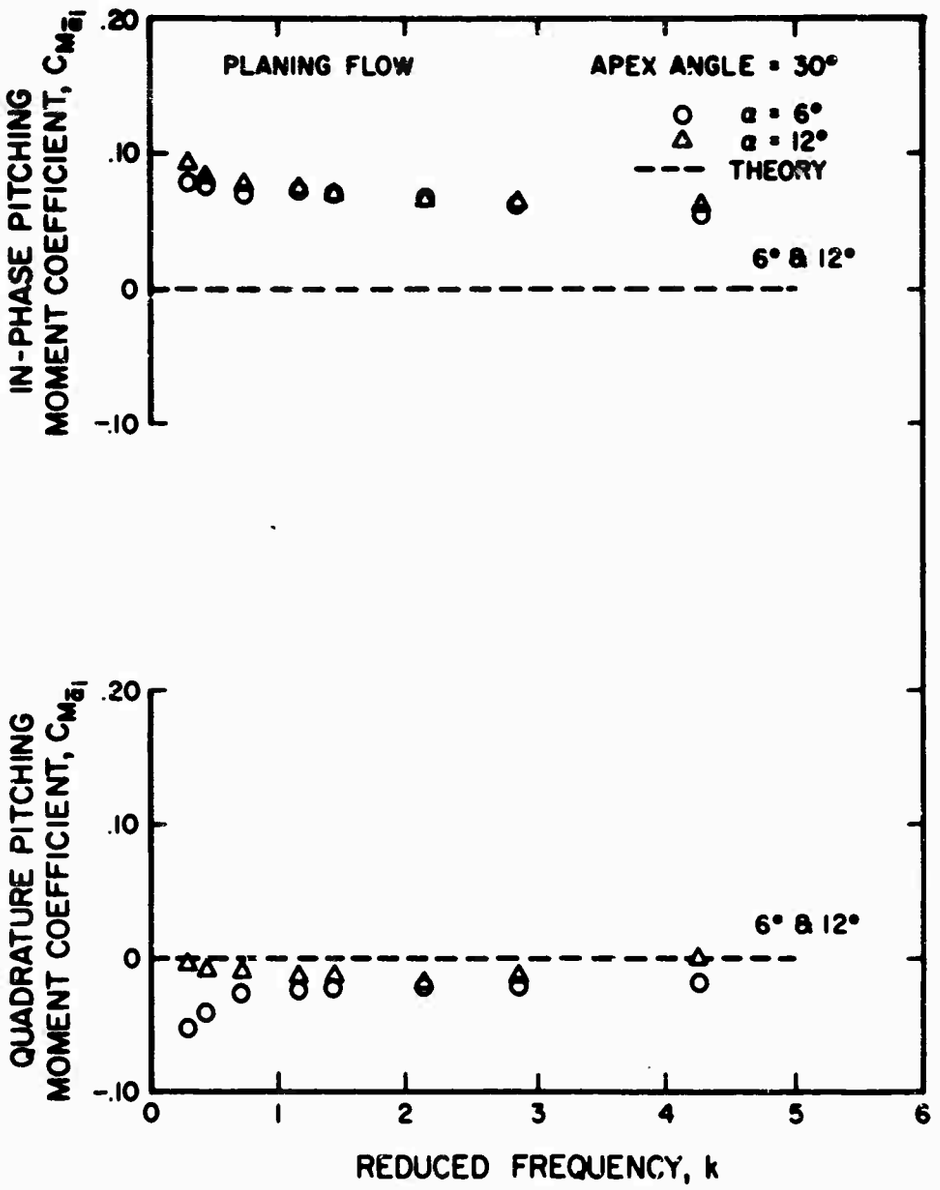

Fig. 47 Unsteady pitching moment coefficients for the planing 30° delta wing.

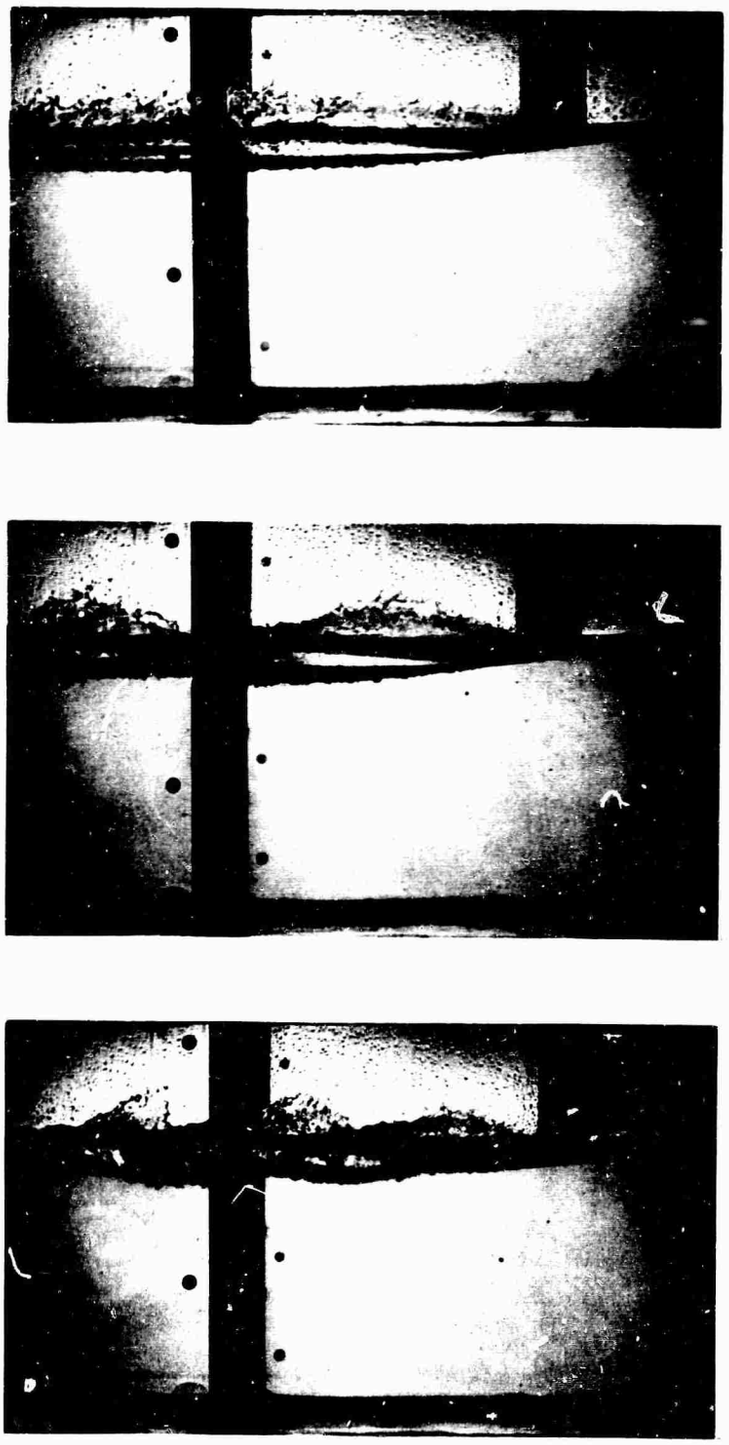

Fig. 48 High speed flash photographs of the 30° delta wing planing at three different reduced frequencies.

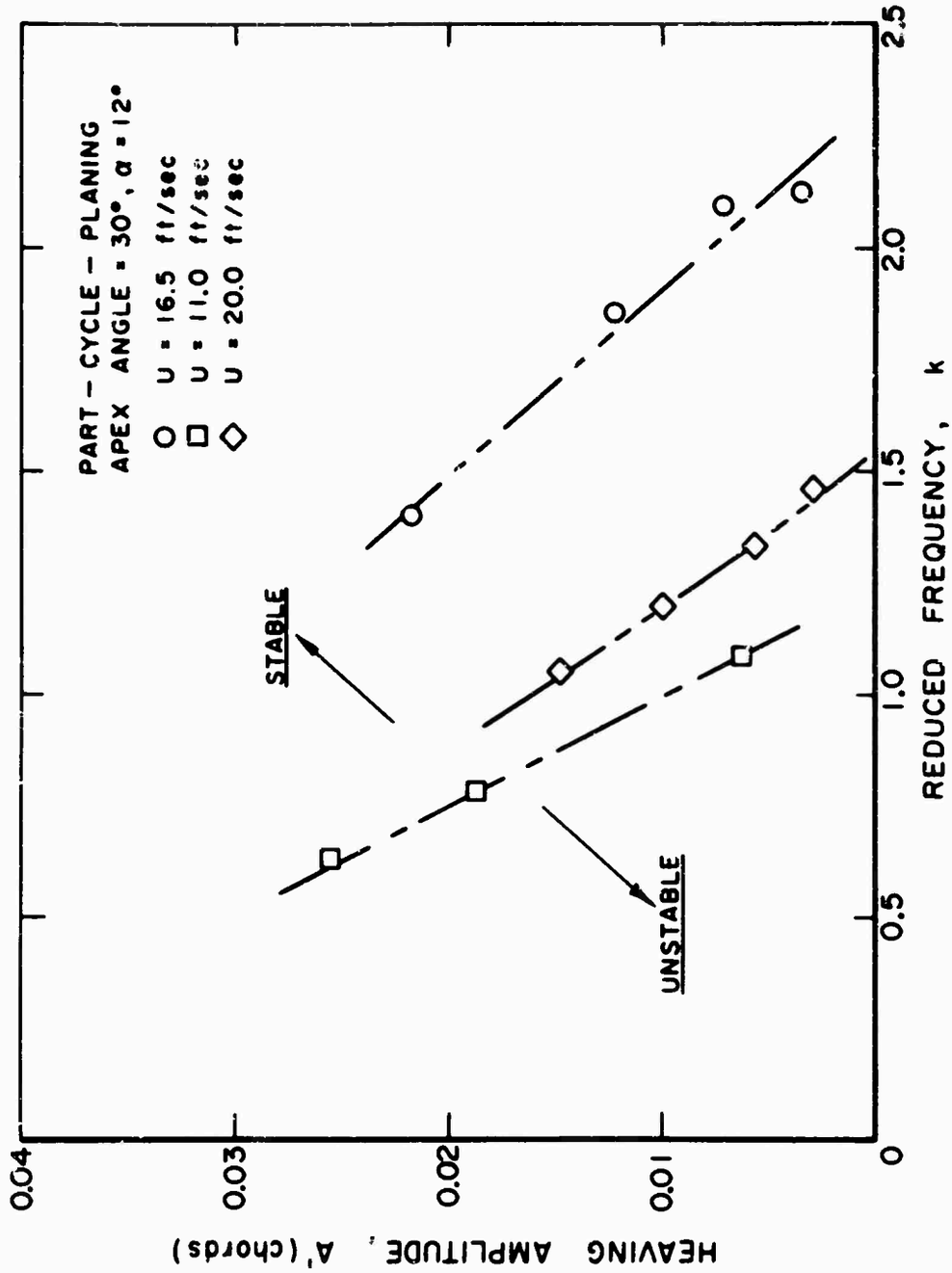

Fig. 49 Frequency-amplitude boundaries for neutral stability of the 30° planing delta wing during 'part cycle' planing.

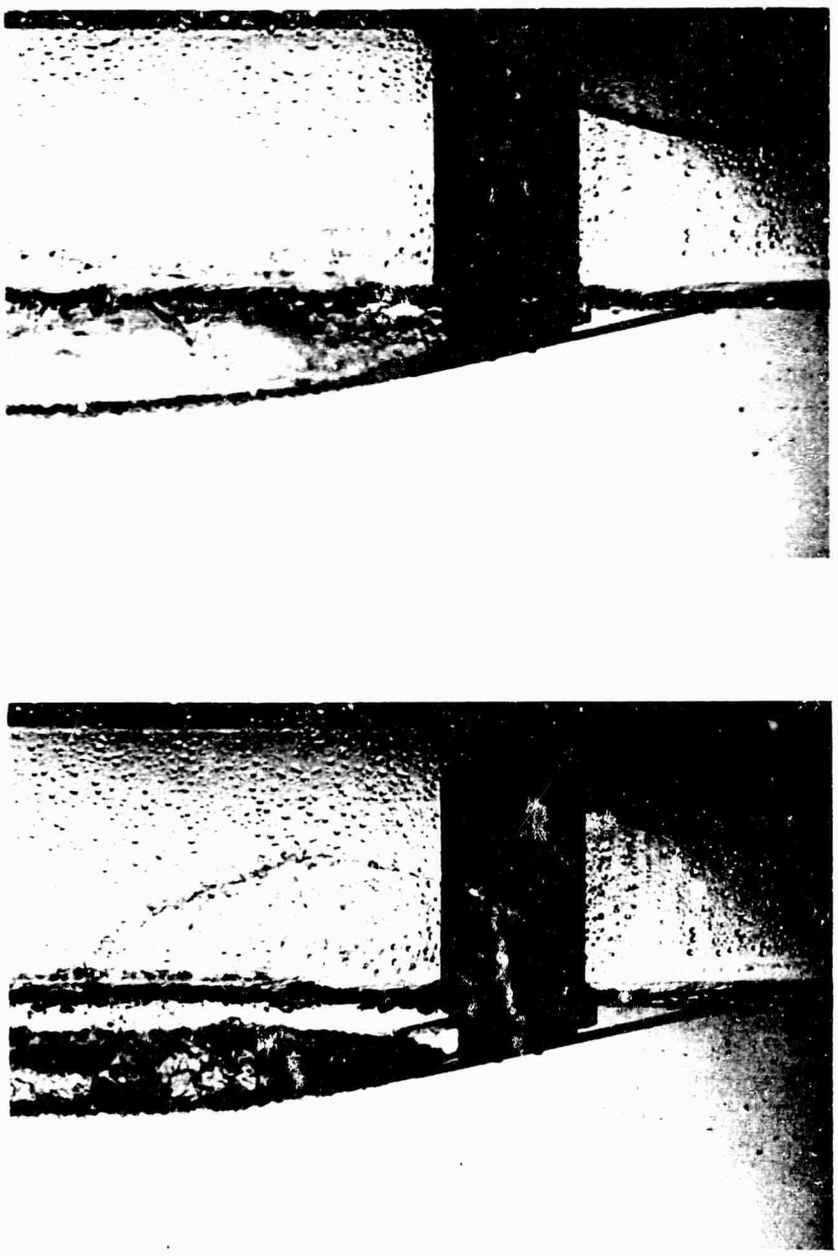

Fig. 50 Flash photographs of 'part cycle' planing; the upper picture shows that part where normal planing occurs. The lower photograph shows that during a position of the cycle, the planing spray sheet collapses on the top of the foil so that it becomes partially wetted and only ventilated tip cavities remain.

Fig. 51 Photograph of the cavitating hydrofoil and support apparatus. The black covering over the supporting strut adjacent to the foil is the waterproofing for the balance shown in Fig. 4. The mean angle of attack shown is 16^{o}.

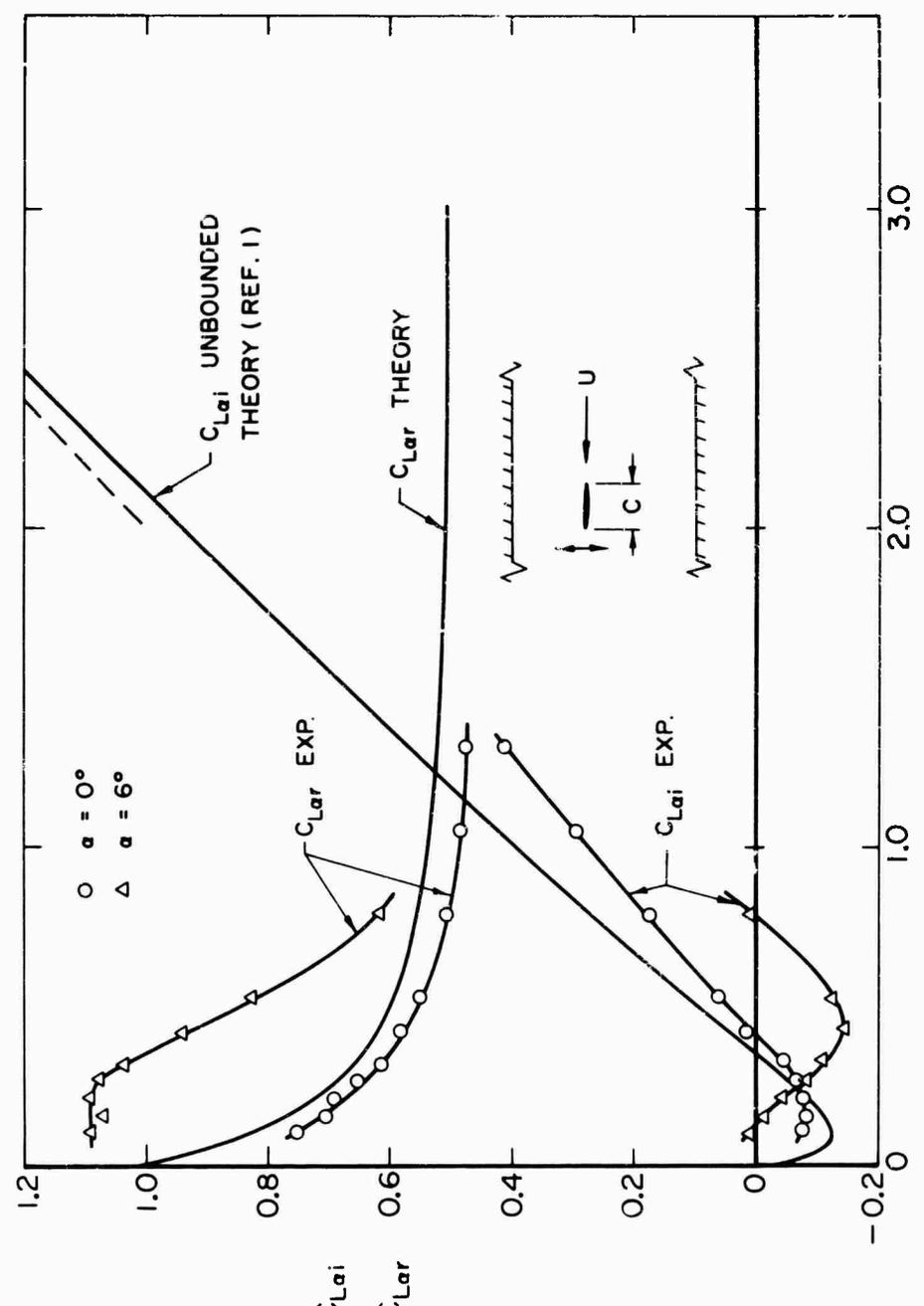

Fig. 52 Unsteady lift coefficients in fully wetted heaving motion of a two-dimensional flat plate hydrofoil for various reduced frequencies and mean angles of attack. Reynolds number based on chord=1.2×10^6. The diagram of the graph shows the relation of the hydrofoil to the tunnel working section.

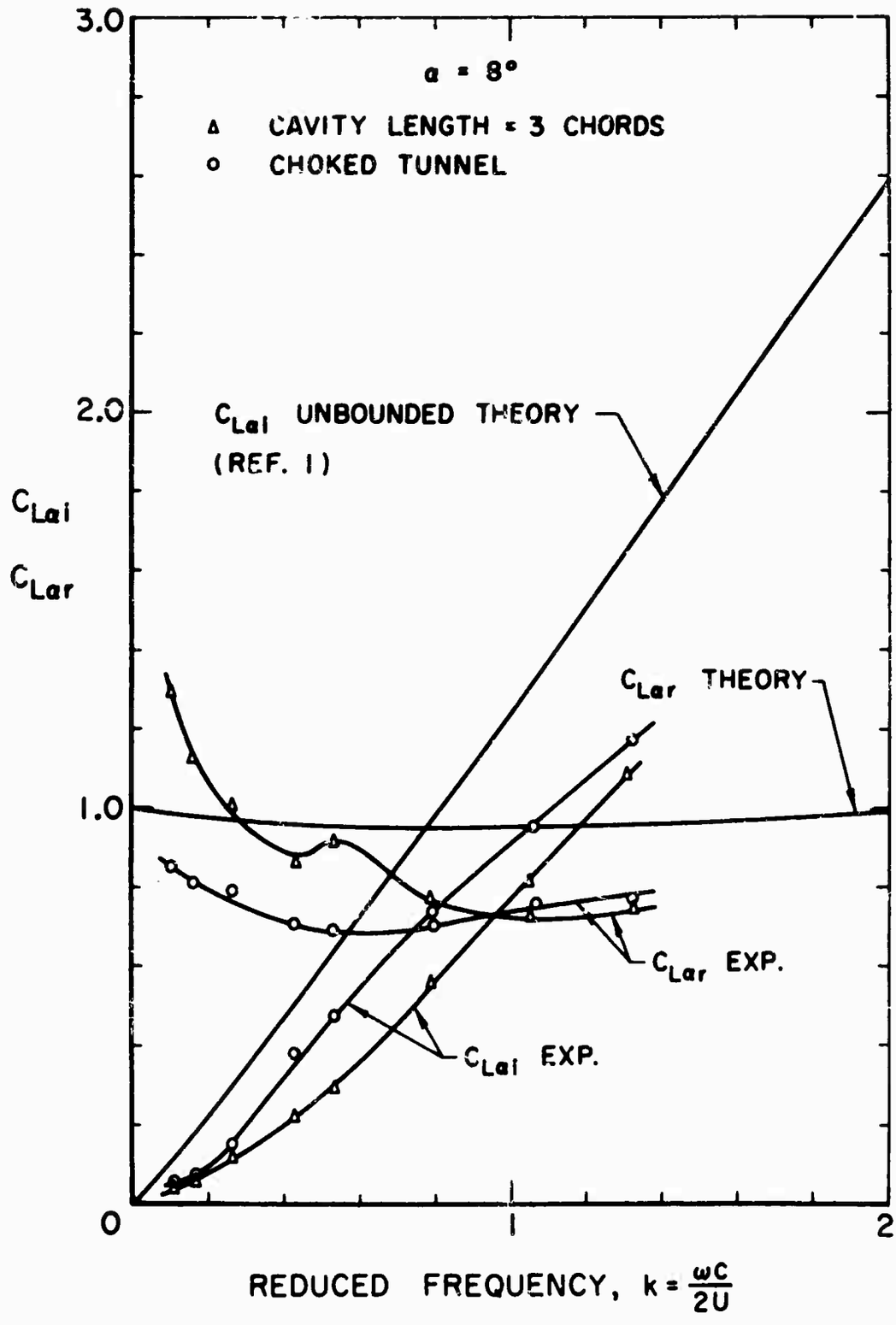

Fig. 53 Unsteady lift coefficients in heaving motion of a naturally cavitating two-dimensional hydrofoil having a mean angle of attack of 8 degrees. These coefficients have been divided by $\pi/2$.

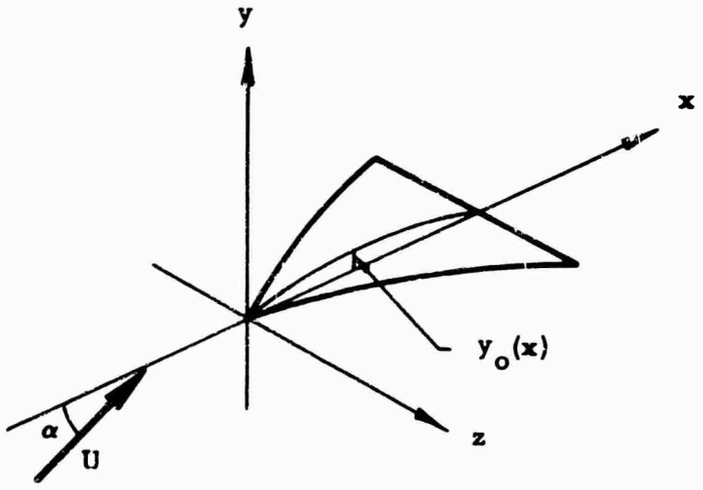

Fig. A-1 The coordinate system used to calculate planing loads.

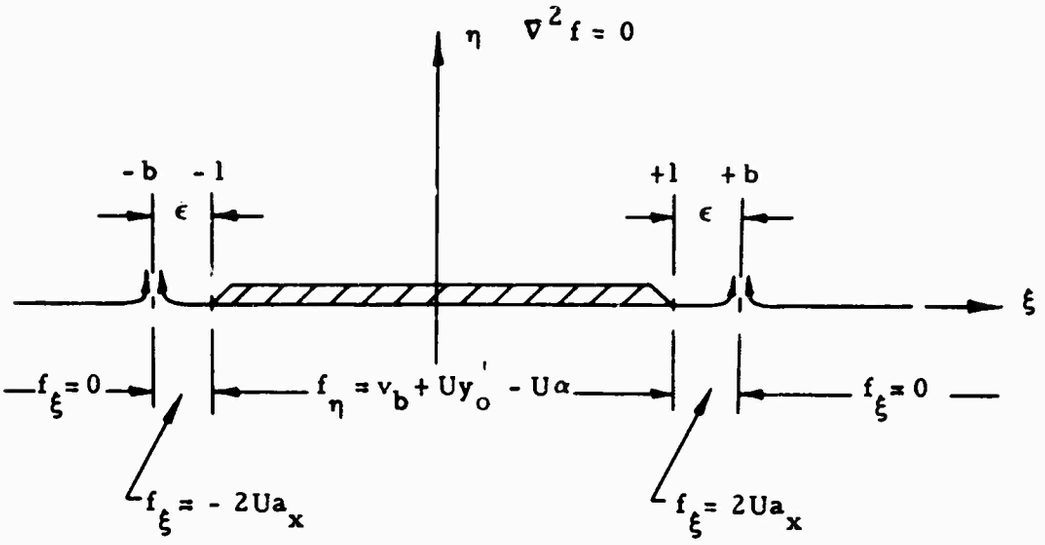

Fig. A-2 The boundary value problem in the reduced cross flow plane.

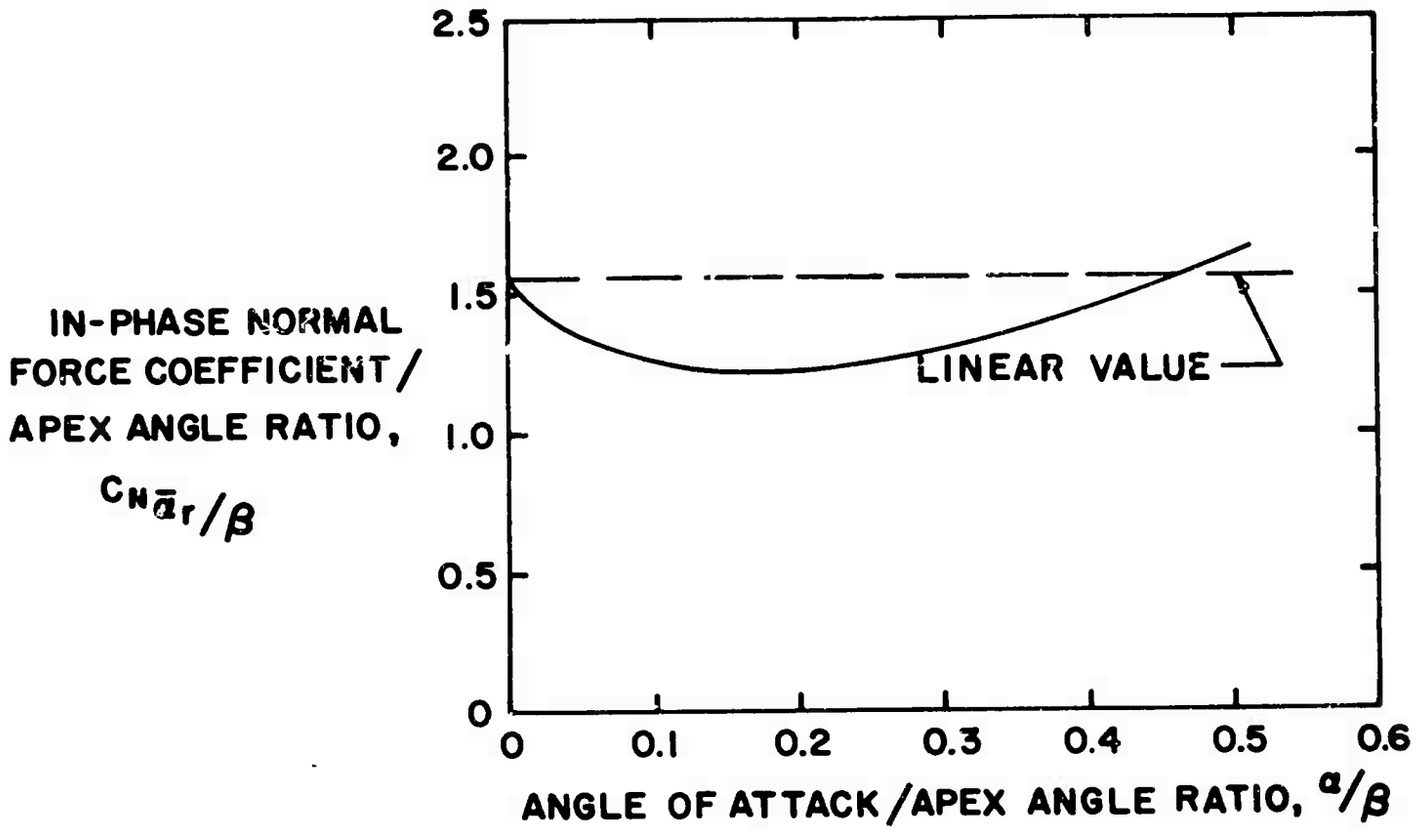

Fig. A-3 Theoretical quasi-steady normal force slope.

UNCLASSIFIED
Security Classification

DOCUMENT CONTROL DATA - R & D

(Security classification of title, body of abstract and indexing annotation must be entered when the overall report is classified)

1 ORIGINATING ACTIVITY (Corporate author)

California Institute of Technology
Pasadena, California

2a. REPORT SECURITY CLASSIFICATION
UNCLASSIFIED

2b. GROUP

3 REPORT TITLE

Experimental Investigation of Non-Steady Forces on Hydrofoils Oscillating in Heave

4 DESCRIPTIVE NOTES (Type of report and inclusive dates)

Final Report

5 AUTHOR(S) (First name, middle initial, last name)

Raymond K. DeLong and Allan J. Acosta

6 REPORT DATE	7a. TOTAL NO. OF PAGES	7b. NO. OF REFS
March 1969	131	34

8a. CONTRACT OR GRANT NO	9a. ORIGINATOR'S REPORT NUMBER(S)
N00014-67-A-0094-0003	
b. PROJECT NO	
c.	9b. OTHER REPORT NO(S) (Any other numbers that may be assigned this report)
d.	

10 DISTRIBUTION STATEMENT

This document has been approved for public release and sale; its distribution is unlimited.

11 SUPPLEMENTARY NOTES	12 SPONSORING MILITARY ACTIVITY
	Naval Ship Research and Development Center, Washington, D. C.

13 ABSTRACT

Measurements of the unsteady forces on heaving delta wing hydrofoils having apex angles of 15° and 30° were carried out in fully wetted flow, planing at a free surface, and with forced ventilation. The fully wetted dynamic measurements were in good agreement with the results of lifting surface theory at small angles of attack. A slender body theory of planing due originally to Tulin is extended to account for non-steady motions. This theory generally underestimates the in-phase lift force; the quadrature unsteady lift is well predicted by the theory. Additional measurements of steady planing delta wings were carried out; for small apex angles and small angles of attack the theory is found to be adequate though it does appear to underestimate the lift somewhat. Some additional experiments on non-steady forces on two-dimensional fully wetted and fully cavitating hydrofoils were also carried out.

DD FORM 1 NOV 65 1473 (PAGE 1)

S/N 0101-807-6801

UNCLASSIFIED
Security Classification

14 KEY WORDS	LINK A		LINK B		LINK C	
	ROLE	WT	ROLE	WT	ROLE	WT
Hydrofoils Nonsteady planing Delta Wings Ventilated Flow						